Intrinsic Flat Bands and Magnetic Proximity in Two-Dimensional Materials

Submitted in partial fulfillment of the requirements for
the degree of

Doctor of Philosophy
in
Materials Science and Engineering

Edward J Seifert

B.S., Physics, University of Texas at Austin
M.S., Materials Science and Engineering, Carnegie Mellon University

Carnegie Mellon University
Pittsburgh, PA

August, 2021

Acknowledgements

When I finished my thesis overview, I knew the journey toward defending my dissertation was going to be tough. That was January of 2020, and I don't think anything could have prepared me for what the next year and half would bring. Nonetheless, here we are, at the end of what may be one of the first PhDs completed *mostly* during a pandemic. Nobody finishes a PhD on their own. This PhD is built upon the shoulders of many others, and every person here deserves a part of the credit.

First, I need to thank my parents. Mom and Dad, you two have been an inspiration for me. The way you lead your lives has been an incredible example for me as I grew up, and as I begin the next chapter of my life. From a young age, you encouraged my interests in math and science. I remember being an excited first grader, who had just learned about subtraction at school and wanted to tell you all about it. You asked me for an example of a subtraction problem, and I naively said "16 minus 17 is... um...", at which point you introduced me to the concept of negative numbers, and I was fascinated. You two have inspired so much of what I do, thank you for being the most encouraging and accepting parents I could have asked for.

I'd like to thank the two professors who have had the biggest impact on my work here, my advisor Ben Hunt and Randall Feenstra. Ben, you taught me to think like a scientist. Every observation has an explanation, and every hypothesis has an experiment to test it. Your incredible knowledge of quantum materials and electron transport was the engine driving much of the early work in this thesis, while I was still learning the basics. Thank you for all the help you've given me. Randy, I have leaned on your vast knowledge of scanning tunneling microscopy these past two years. Almost every experiment idea from the STM sections of this work was discussed with you beforehand. You taught me not only the art of surface science, but also the intricate details of vacuum science, which naturally goes hand-in-hand with STM measurement. Thank you so much for your patience with me as I learned. And thank you for answering the phone when I frantically called at 9:30pm on a week night when I was sure I'd destroyed my best sample.

I'd like to thank my undergraduate advisor, Elaine Li from the University of Texas at Austin. I worked in your lab for two years, and it was my first exposure to experimental physics research. You got me started with 2D materials, and it stuck with me throughout my entire PhD. Thank you for taking a chance on a timid undergrad sending you an email about taking part in physics research.

All of the lab mates who have mentored me in the past, this paragraph is for

you. Deva Gopalan, you were my partner in crime. We made every transport device together, celebrated our successes and persevered through our failures together. You taught me every fabrication technique I know. Electron beam lithography, reactive ion etching, our dry-transfer techniques, everything. Our friendship has been a defining part of my time as a graduate student, and I cannot wait to join you in Portland when I'm done. Thank you, Deva. Sergio de la Barrera, seeing how you approach problems in the lab was inspiring, and even today I'm often asking myself "How would Sergio solve this problem?" This lab would not nearly be the lab it is without your work, and we still use so many tools you created. Your knowledge of Python inspired me to learn, and I can confidently say most of the modeling and computational aspects of this work would not have happened without that inspiration. Thank you, Sergio. Dacen Waters, you taught me the nitty-gritty of STM. You set up the entire STM laboratory that I inherited. Every single STM measurement presented in this thesis relies largely on your work. I cannot thank you enough for helping me transition to thinking like a surface scientist. Thank you, Dacen.

Thank you to all of my lab mates that have been on this journey with me: Michael Sinko, Ryan Muzzio, Qingrui Cao, Erin Grimes and John Lyons. Thank you for lending an ear when I had a tough problem to solve, and I've enjoyed discussing problems in your own projects as well. Thank you for help with experimental problems as well, seeing how you solve problems has helped me come up with my own solutions along the way. A special thank you to Erin Grimes: you're the first and only student I got to teach about STM. I've seen you work through many of the same problems as I did when I was learning, and I'm certain I'm leaving the STM lab in good hands. Thanks for working with me, and thank you for helping out with several of the measurements here. I wish you the best of luck with the rest of your PhD.

And lastly but most importantly, I want to thank my boyfriend, Todd Long. Man, five years of a long distance relationship is impressive, and we've managed to do it together. You've been my motivation this entire time. Coming home every day and getting to chat with you, to feel your positive energy, that's what I looked forward to the most every single day. Thank you for sticking by my side this entire time, bunny boy.

Thank you to my committee members:

- Benjamin M. Hunt (advisor)
- Randall Feenstra
- Lisa Porter

- Marek Skowronski

Thank you to my funding sources: the Department of Energy, the National Science Foundation, and the Department of Defense's National Defense Science and Engineering Graduate Fellowship.

Abstract

van der Waals materials offer a new paradigm in controlling the properties of materials. The ability to combine materials into heterostructures and precisely control the arrangement of atoms along the stacking axis allows researchers to engineer topological properties via proximity effects, or create energetically flat bands that encourage many-body effects.

This work represents progress towards both engineering topological properties in materials and observing exotic correlated states in flat bands. In chapter 4, I discuss experiments towards realizing a magnetic proximity effect in a van der Waals heterostructure, a critical ingredient to break time-reversal symmetry and realize topological phenomena such as the quantum anomalous Hall effect. To achieve this, I create heterostructures of graphene and several different 2D magnetic materials, including CrI_3, $CrBr_3$ and α-$RuCl_3$. I demonstrate that the chemical instability of both CrI_3 and $CrBr_3$ are detrimental to graphene electronic quality and induce a massive effective doping, which prohibits their use as proximity ferromagnetic materials despite their extensive optical studies. In α-$RuCl_3$/graphene heterostructures, I demonstrate the absence of a proposed ferromagnetic state, instead observing an anti-ferromagnetic transition at an elevated temperature that is tunable in gate voltage.

In addition, I study intrinsic flat surface bands in rhombohedral graphite using scanning tunneling microscopy and spectroscopy, which may hold interested correlated physics including superconductivity. A thickness-dependent measurement of flat surface states is performed, demonstrating the increasing density of states of the sharp central van Hove singularity as thickness is increased for the first time experimentally. In the thickest sample, an exploration of the rhombohedral/hexagonal phase boundary illuminates how changes in stacking order as the boundary is approached have a measureable effect on the surface density of states. A search for correlated states is performed in the thickest sample, however doping due to surface contamination and a strong electric field screening prevent observation of these states. Altogether, this work is a small step forward toward engineering topological properties and exotic many body effects in 2D heterostructures.

Contents

List of Tables

List of Figures

1 Introduction

In the most commonly used models of solids, electrons are viewed as non-interacting particles, occupying energetic landscapes that can be calculated in the absence of electron-electron interaction effects. The large kinetic energy of free electrons in a solid causes them to move so fast past each other that they do not interact at all, and the first descriptions of electronic behavior of materials completely ignores electron-electron repulsion. Metals are materials with a partially filled highest energy band, insulators have a completely filled highest energy band, and in between these two are semiconductors with a small enough energy gap between the highest filled and lowest unfilled bands that charge carriers can be thermally excited.

In the middle of the 20th century, materials were discovered that seemed to disobey these principles. Materials with partially-filled bands did not have metallic character and instead behaved as insulators, specifically the transition metal oxide NiO [1]. It would later be discovered that this phenomenon resulted from electron-electron correlations in the material, where the electrostatic interaction between electrons prevents their free motion, confining them around the ions from which they were donated. This "correlated insulator" was one of the first examples of macroscopic effects resulting from these previously-ignored particle interactions in a material. Since its discovery, many other many-body effects in solids have been discovered. Superconductivity, where electrons of opposite spins pair up to form bosonic quasiparticles called Cooper pairs, or ferromagnetism, where electrons align their spins due to a fermionic exchange effect, are the two perhaps most famous examples. Beyond these are many more examples, including charge density waves, fractional quantum Hall effects, and others. The continued search for these exotic states of matter have caused researchers to seek out materials with strong electron-electron interactions, and it is thus an important goal of experimental physics research to find these states in nature and discover how they occur.

This search has led researchers to flat bands: regions of the electronic band structure where a weak energy-momentum dispersion leads to a sharp peak in the density of states. In a flat band, there exists a large number of electrons with similar energies and crystal momenta, allowing them to interact with one another and potentially form one of these exotic states. Electron kinetic energy, proportional to the band width W, is at a minimum, and the coulomb interaction energy $E_c = \frac{1}{4\pi\epsilon_0}\frac{e^2}{r_{12}}$ dominates electron behavior. Flat bands can occur naturally, such as in flat d-bands of transition metals that form permanent magnets [2], or they can be induced by variation of external parameters like magnetic field, such as in the case of Landau level physics

in a 2D electron gas in a semiconductor quantum well [3, 4]. More recently, researchers have engineered flat bands by carefully stacking single atomic layers of materials, and have observed a wide range of interesting correlated electron states [5–12].

Recently in condensed matter research, a heavy emphasis has been put on two-dimensional van der Waals materials. These are materials that, in their bulk form, consist of covalently-bonded two dimensional planes of atoms that stack together to form a three dimensional bulk. These planes are held together by relatively weak van der Waals bonds, which allows researchers to peel apart the layers and isolate a single sheet of atoms. Most famously this was done for graphene, a single sheet of carbon atoms, but since then a variety of 2D materials have been created, including insulators, semiconductors, ferromagnets, superconductors, and more.

With few exceptions, bulk properties of 3D materials dominate overall material properties. Unit cells deep in the interior of a 3D crystal see only identical neighbors, and properties in these materials can only be adjusted either by adjusting external parameters (i.e. temperature, applied magnetic field) or by growing new materials with different structures or different compositions. However, atoms near the surface can have properties different than those in the bulk, either from the lack of symmetry near the surface or from close proximity to neighboring materials with different properties. This ability to inherit the properties of other nearby materials is called a "proximity effect".

With 2D materials, everywhere is a surface. There is no "bulk" that cannot be in close proximity to another material. The entirety of the material can be proximitized, and fundamental properties of two materials can be combined in a single structure. With a host of physical properties present in 2D materials, including extremely high mobility in graphene [13], superconductivity in $NbSe_2$ [14] and TaS_2 [15], and ferromagnetism in CrI_3 [16] and $CrSiTe_3$ [17], physicists and materials scientists have a playground of physical properties that may be combined simply by stacking these materials on top of one another. This provides an avenue towards realizing a host of interesting physical phenomena which require a combination of exotic physical properties.

In this thesis, I will describe my research over the past five years on flat bands in two dimensional materials and proximity effects between different 2D materials. Chapter 2 will give an overview of 2D materials and describe all materials used in this work, and give a necessary description of magnetism in 2D materials that will be useful in later discussions. Chapter 3 will describe the techniques used in my projects, give a full description of sample fabrication from start to finish, and give an overview of scanning tunneling microscopy, one

of the primary techniques used in this thesis. Chapter 4 will describe my work on inducing a magnetic proximity effect in graphene using 2D ferromagnets, and measuring this proximity magnetism using electron transport techniques. Chapter 5 will describe my recent measurement of intrinsic surface flat bands in rhombohedral graphite using scanning tunneling microscopy, before concluding the thesis in chapter 6.

2 Background: 2D Materials and Magnetic Proximity

2.1 2D Materials

In 2004, graphene, a single atomic layer of carbon arranged in a hexagonal lattice, was isolated experimentally for the first time by Andre Geim and Konstantin Novoselov, an achievement which won them the Nobel Prize in 2010 [13]. Graphene attracted immediate interest, as it had been predicted to possess extraordinarily large electron mobility as well as a unique linear dispersion, and researchers quickly discovered many exotic physical phenomena in the material, including the integer and fractional quantum Hall effects with a unique 4-fold symmetry [18–21], and more recently, superconductivity [5, 6] and anomalous ferromagnetism [7, 8]. Since graphene's discovery, a wide variety of 2D materials have been discovered, including insulating hexagonal boron nitride [22, 23], semiconducting transition metal dichalcogenides MoS_2, $MoSe_2$, WS_2, and WSe_2 [22, 24], ferromagnetic insulators CrI_3 [16], $CrBr_3$ [25], $CrSiTe_3$ [17] and $Cr_2Ge_2Te_6$ [26], anti-ferromagnetic Mott insulator α-$RuCl_3$ [27,28], topological insulator 1T'-WTe_2 [29], among many others.

There are many advantages that 2D materials offer over traditional 3D materials. First, fabrication of 2D materials with pristine quality is easy. Single atomic layers can be isolated from a bulk crystal using mechanical exfoliation (colloquially, the "Scotch tape" technique), and the resulting materials are high-quality, pristine atomic layers on par with those grown by expensive, time-consuming techniques like molecular beam epitaxy (MBE). Second, 2D materials offer remarkable tunability compared to 3D materials. The electric field effect, whereby a DC voltage is applied across a dielectric to create a capacitive effect between the 2D material and back gate, allows researchers to finely tune the charge density within the entire 2D material, in a similar manner to creating an inversion layer in a MOSFET. To achieve this same effect in a 3D material, electron donors/acceptors are typically implanted into the material, which requires creation of an entirely new material. This charge density tuning in 2D materials is as simple as turning a knob. Third, 2D materials can be stacked together, allowing researchers to easily combine materials with a wide variety of properties to create a "super-material" that potentially has the properties of all of the constituents. Even further, 2D materials can be rotated on top of one another, giving rise to a novel "twist" degree of freedom that has no analog in conventional 3D materials [6]. Altogether, 2D materials offer many avenues to explore interesting physical properties that are either

extremely difficult or even impossible to explore in 3D materials, with a lower fabrication time and cost than that of most 3D materials.

In this section, I'll discuss many of the 2D materials I use in my own research. I'll start with a description of graphene and its interesting electronic properties, which has been used in every project in this thesis. Then I'll discuss hexagonal boron nitride and transition metal dichalcogenides, which are often used as substrates in this work. Finally, I'll discuss the recently-discovered 2D magnetic materials, which are used in proximity devices with graphene.

2.1.1 Graphene

Monolayer graphene is made up of a single atomic layer of carbon atoms in a honeycomb lattice. The unit cell of graphene contains two carbon atoms, dubbed the A and B atoms, forming two interpenetrating trigonal sublattices of A and B carbons. Of the four valence electrons in carbon, three are occupied in the in-plane, sp^2 hybridized orbitals, while one remains in the out-of-plane, un-hybridized p_z orbital. These sp^2 orbitals covalently bond A atoms to the three nearest-neighbor B atoms and vice versa, forming strong σ bonds that contribute to graphene's high in-plane stability. The p_z electrons form a delocalized π band that, in bulk graphite, weakly holds together layers with van der Waals forces.

This π band is also responsible for the electronic structure of graphene near the Fermi level, and we can use a simple tight-binding model to describe it. The Hamiltonian for such system is described by:

$$H = \gamma_0 \sum_{\langle ij \rangle} (a_i^\dagger b_j + h.c.)$$

where $a_i^\dagger$ and b_j denote creation of an electron on the A sublattice and destruction of an electron on the B sublattice, respectively, $\gamma_0 \approx 3.1$ eV [30] is the hopping integral describing electron motion between the sublattices, and the summation is over nearest neighbors. The Hamiltonian can be written in the sublattice basis (ψ_A, ψ_B), and utilizing the nearest neighbor lattice vectors:

$$\delta_1 = \frac{a}{2}\left(\frac{1}{\sqrt{3}}, 1\right) \qquad \delta_2 = \frac{a}{2}\left(\frac{1}{\sqrt{3}}, -1\right) \qquad \delta_3 = \frac{a}{2}\left(\frac{-2}{\sqrt{3}}, 0\right)$$

where a = 2.46 Åis the lattice constant for graphene. The resulting Hamiltonian for this system is:

$$H = \begin{pmatrix} 0 & \sum_j e^{ik\cdot\delta_j} \\ \sum_j e^{-ik\cdot\delta_j} & 0 \end{pmatrix}$$

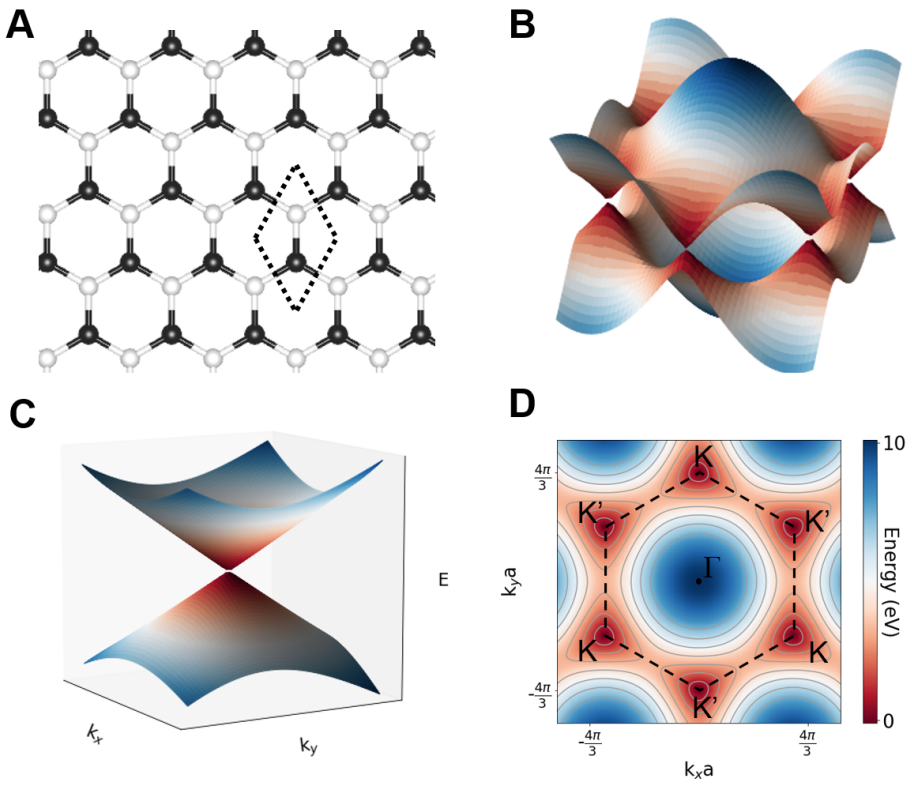

Figure 2.1: **a)** Crystal structure of a single sheet of graphene. Black and white balls denote the A and B sublattice. The dashed parallelogram is the unit cell of graphene. **b)** Full view of the band structure of graphene over the first Brillouin zone. **c)** A close up of the linear bands at the K and K' point, called the Dirac point or charge neutrality point. **d)** A topographical map of the full graphene π-band. The colorbar is shared among b-d).

Taking the eigenvalues of this Hamiltonian yields the two low energy bands of graphene:

$$E(\vec{k}) = \pm\gamma_0 \sqrt{3 + 4\cos\left(\frac{\sqrt{3}ak_x}{2}\right)\cos\left(\frac{ak_y}{2}\right) + 2\cos\left(ak_y\right)}$$

This band structure is depicted in figure 2.1. The conduction band and valence bands touch at high-symmetry K and K' points, having no band gap but zero density of states at the point they touch, which is often called the Dirac point or charge neutrality point (CNP). This causes graphene to behave

semimetallically.

A few symmetries become apparent when studying the band structure in 2.1. First, spin was not considered in the creation of this band structure. In the absence of any magnetic field, graphene exhibits a spin degeneracy, so each band shown contains two subbands, one for each spin projection. Comparing the K and K' points, a valley degeneracy is observed, where the operation K $\rightarrow$ -K appears to take the band structure into itself. In fact, the degeneracy between the K and K' points a consequence of inversion symmetry of the lattice and thus should always be present at zero magnetic field. At each of the K/K' points, graphene appears to have symmetric valence and conduction bands. However, the apparent particle-hole symmetry is a consequence of the nearest-neighbor approximation: including the next-nearest neighbors into the tight-binding calculation breaks this symmetry at higher energies.

Expanding around the K and K' points (i.e. for $\vec{p} \equiv \hbar(\vec{K} - \vec{k})$) gives the linear dispersion graphene is known for:

$$E = \pm\hbar v_F|\vec{k}| = \pm v_F|\vec{p}|$$

This mimics the dispersion relation in the relativistic Dirac equation with zero mass ($E = c|\vec{p}|$), which is why charge carriers in graphene are often called "Massless Dirac Fermions" [30].

Interestingly, graphene displays an extraordinarily high intrinsic mobility as compared to traditional semiconductors. Graphene has extremely low electron-phonon scattering rates, which set the fundamental limit on carrier mobilities in semiconductors [31]. This causes an intrinsic mobility in excess of 100,000 cm^2/Vs. However, graphene mobility is often limited by effects from the substrate, where substrate roughness can introduce short-range scattering sites and charge-trapping can cause local electrostatic doping leading to "charge puddles" in graphene [23, 32]. Thus substrate choice is of extreme importance in graphene magnetotransport measurements.

Graphene devices (and many other 2D materials) also allow for fine control over charge carrier density via the electric field effect. Graphene is often exfoliated on a heavily p-doped silicon substrate that is capped with a thin 300nm oxide layer. By applying a bias voltage to the silicon, a capacitive effect is induced between the silicon and 2D material, which generates mobile charge carriers in graphene. This effectively varies the chemical potential in the 2D material, as if it were possible to change the doping of the material with the turn of a knob. This is the same effect at play as in field-effect transistors, and was the subject of the Nobel prize-winning paper by Andre Geim and Konstantin Novoselov [13].

2.1.2 Bilayer Graphene

Bilayer graphene, depicted schematically in figure 2.2a, is made of two sheets of monolayer graphene stacked such that the B sublattice in the top layer lies directly above the A sublattice in the bottom layer (B_1 and A_2, respectively). The remaining sublattices, A_1 and B_2, do not have a neighbor directly below/above them. The electronic structure for bilayer graphene may be calculated in a similar manner as the monolayer, using a tight-binding model to quantify electron motion between nearest neighbors. In this case, an additional hopping $\gamma_1 \approx 0.38$ eV [30] must be included to account for interlayer hopping between the A_2 and B_1 sublattices. Additional terms, such as γ_3 describing hopping between the A_1 and B_2 sublattices, have only minor effects on the band structure and are excluded for now [30].

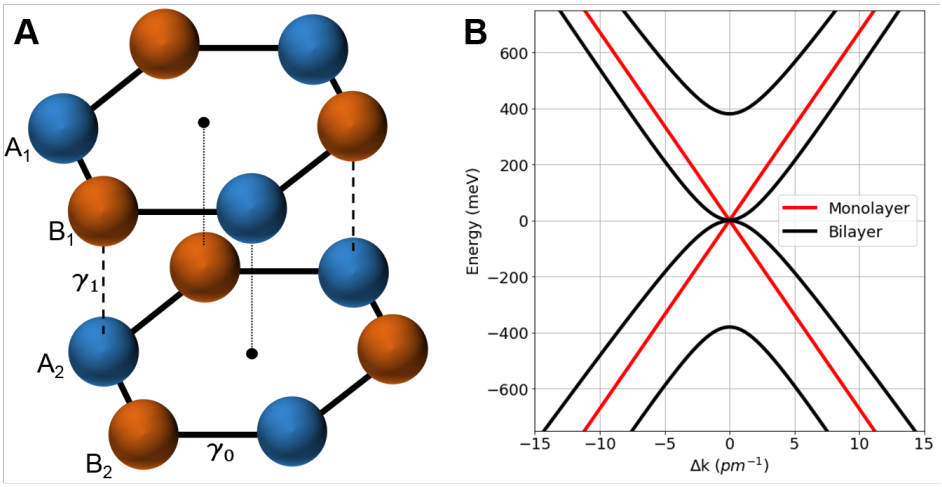

Figure 2.2: **a)** An atomic model of bilayer graphene. The A sublattice is in blue while the B sublattice is in orange.**b)** Band structure near the K or K' points for bilayer graphene, plotted alongside that of monolayer graphene. The addition of γ_1 hopping flattens the two bands near the Fermi level, and pushes the other two away from the Fermi level.

The Hamiltonian for this system is described in the (layer) $\times$ (sublattice) basis $(\psi_{A1}, \psi_{B1}, \psi_{A2}, \psi_{B2})$ below:

$$H = \begin{pmatrix} 0 & \gamma_0 \sum_j e^{ik\cdot\delta_j} & 0 & 0 \\ \gamma_0 \sum_j e^{-ik\cdot\delta_j} & 0 & \gamma_1 & 0 \\ 0 & \gamma_1 & 0 & \gamma_0 \sum_j e^{ik\cdot\delta_j} \\ 0 & 0 & \gamma_0 \sum_j e^{-ik\cdot\delta_j} & 0 \end{pmatrix}$$

and the eigenvalues describing the band structure around the K point are plotted in figure 2.2b alongside that of the monolayer. In the absence of γ_1 hopping, the two graphene sheets would behave as two uncoupled copies of the monolayer, displaying linear bands touching at the K point. However when γ_1 is turned on, the bands split apart. Away from the K-point, the bands retain the linear dispersion with the same monolayer band velocity v_F, offset from each other by γ_1. At the K-point, two bands associated with the A_2 - B_1 dimer move away from the Fermi level by $\pm\gamma_1$ while the other two bands remain at low energies, gaining an approximate *parabolic* shape, $E \sim k^2$, as opposed to the linear dispersion seen in a single layer. These low energy parabolic bands are associated with the two sublattices that do not have a γ_1 hopping partner, A_1 and B_2 in this case, and it is specifically this lack of a γ_1 partner that causes the bands to remain at low energies. This gives bilayer graphene a semimetallic character, and several interesting phenomena including gaps opening due to applied electric field, unorthodox Landau level sequences and crossings, and much more have been observed in this material [33, 34].

2.1.3 Hexagonal Graphite and Rhombohedral Graphite

The addition of a third layer of carbon adds a degree of freedom absent in the bilayer case: stacking order. There exist two common phases of 3+ layer graphite: the thermodynamically-stable hexagonal graphite and the meta-stable rhombohedral graphite, both of which are illustrated in figure 2.3. In hexagonal graphite, the third layer stacks exactly over top of the first, resulting in an "ABA"-style stacking. The A sublattice on this new layer lies over top the B sublattice on the layer below, resulting in a contiguous chain of A-B-A atoms throughout the bulk of hexagonal graphite that are all connected by γ_1 hopping. The remaining sublattices in each layer do not have a γ_1 hopping partner. The resulting band structure for a trilayer stack, shown in figure 2.3e, has a similar form as the bilayer but with an additional band added near the Fermi level. The quadratic band near the Fermi level arises mostly from the atoms on the middle layer without a γ_1 partner, while the states pushed well away from the Fermi level arise mostly from atoms in the middle of the γ_1 chain running through the bulk of the material. The remaining bands are almost evenly split amongst atoms on either surface. The addition of more ABA-stacked layers continues this trend: more states are added near the Fermi level with a large weight on atoms in the bulk, and thus a bulk semimetallic behavior is seen.

In rhombohedral graphite, the third carbon layer stacks in a unique position that is not directly over top either of the layers below, resulting in an "ABC"-

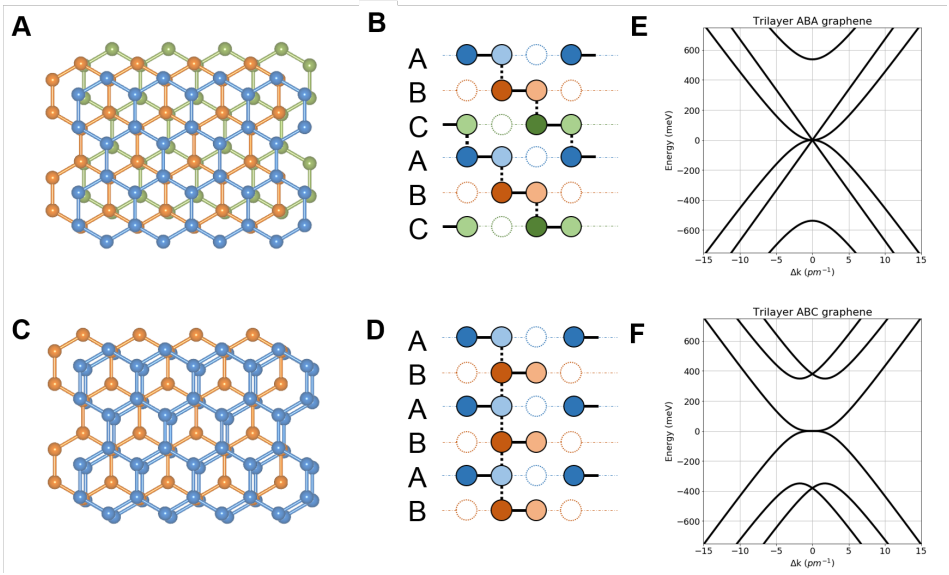

Figure 2.3: **a-b)** Top-down view (a) and side-view (b) of the crystal structure of hexagonal (ABA) graphite. **c-d)** Top-down view (c) and side-view (d) of the crystal structure of rhombohedral (ABC) graphite. **e-f)** Band structures for trilayer hexagonal (ABA) graphite and rhombohedral (ABC) graphite.

style stacking that is detailed in figure 2.3. The B sublattice of this new layer lies on top of the A sublattice on the layer below, which previously did not have a γ_1 partner. In fact, a careful inspection of figure 2.3d shows that every atom in the bulk of rhombohedral graphite has a γ_1 partner, leaving no unpaired atoms. There does not exist a pathway through the bulk that utilizes only interlayer nearest-neighbor hopping, and electrons must instead utilize both γ_0 and γ_1 pathways to travel between either surface. The resulting band structure for a trilayer of rhombohedral graphite, shown in figure 2.3f, shows the additional bands have been pushed away from the Fermi level to higher energies. Only two bands, those arising from the sublattices on either surface without a γ_1 partner, remain at the Fermi level. These surface states gain a *cubic* shape, $E \sim k^3$, as opposed to the quadratic dispersion of the bilayer and the linear dispersion of the monolayer. As a result, the bulk of rhombohedral graphite behaves as an insulator while the surfaces are metallic in nature.

Another way to think about these conducting states is in the context of the Su-Schrieffer-Heeger (SSH) model for a 1D topological insulator. In the typical SSH model, a 1D chain with a two atom basis in established, and two

different hopping strengths characterize electron motion: u for hopping within the unit cell and v for hopping outside of the unit cell. For any v $\neq$ u, this model describes an insulator, however the insulators described by v $>$ u are topologically distinct from the v $<$ u insulator, which is itself equivalent to the vacuum. Thus the boundary between a v $>$ u insulator and the vacuum must host a zero-dimensional edge state residing at this boundary, which for the SSH chain exists on each end of the chain [35]. Rhombohedral graphite can be thought of in this exact manner: chains of carbon atoms connected by γ_0 and γ_1 hoppings exist from one surface to the other. In order to complete this chain in rhombohedral graphite, an electron must necessarily utilize both hopping pathways. In this way, the rhombohedral graphite chains are exactly analogous to the SSH 1D chain, and one should expect insulating behavior in the bulk with metallic character at the surface [36]. One can generalize this 1D model to a 3D material by considering several of these 1D SSH chains lined up next to each other, with their zero-dimensional edge states forming a 2-dimensional surface state on either side of the rhombohedral stack.

As more layers are added to the rhombohedral graphite stack, this trend from the trilayer case continues. Bulk layers are pushed away from the Fermi level due to γ_1 hopping while states from the opposite sublattices on opposite surfaces remain at low energies. The surface states gain a flatness proportional to the thickness of the sample, $E \sim k^N$. The low-energy band structure for samples of thickness N = 5, 9, and 14 are plotted together in figure 2.4a. These flat bands result in sharp peak in the density of states centered around E = 0, which is shown in 2.4b. Additionally as thickness increases, the number of valence and conduction bands that have been pushed away from the Fermi level increases. The onset of these bands are clearly seen as peaks above and below the Fermi level in the density of states calculation.

2.1.4 Hexagonal Boron Nitride

Hexagonal boron nitride (hBN) is another layered material similar to graphene, containing atomic sheets in a covalently-bonded hexagonal lattice held together by relatively weak van der Waals forces. Instead of having identical atoms on the A and B sublattices like graphene, hBN has alternating boron and nitrogen atoms, each occupying its own sublattice. This results in hBN being a wide band gap insulator, with a gap around 6 eV [37].

hBN acts as a great substrate for 2D devices. The SiO_2 often used as a substrate is extremely rough, with surface roughness on the order of 1 nm. This results in introduction of short-range scattering sites that limit the mobility of graphene devices. Using hBN as a substrate causes roughly a 3

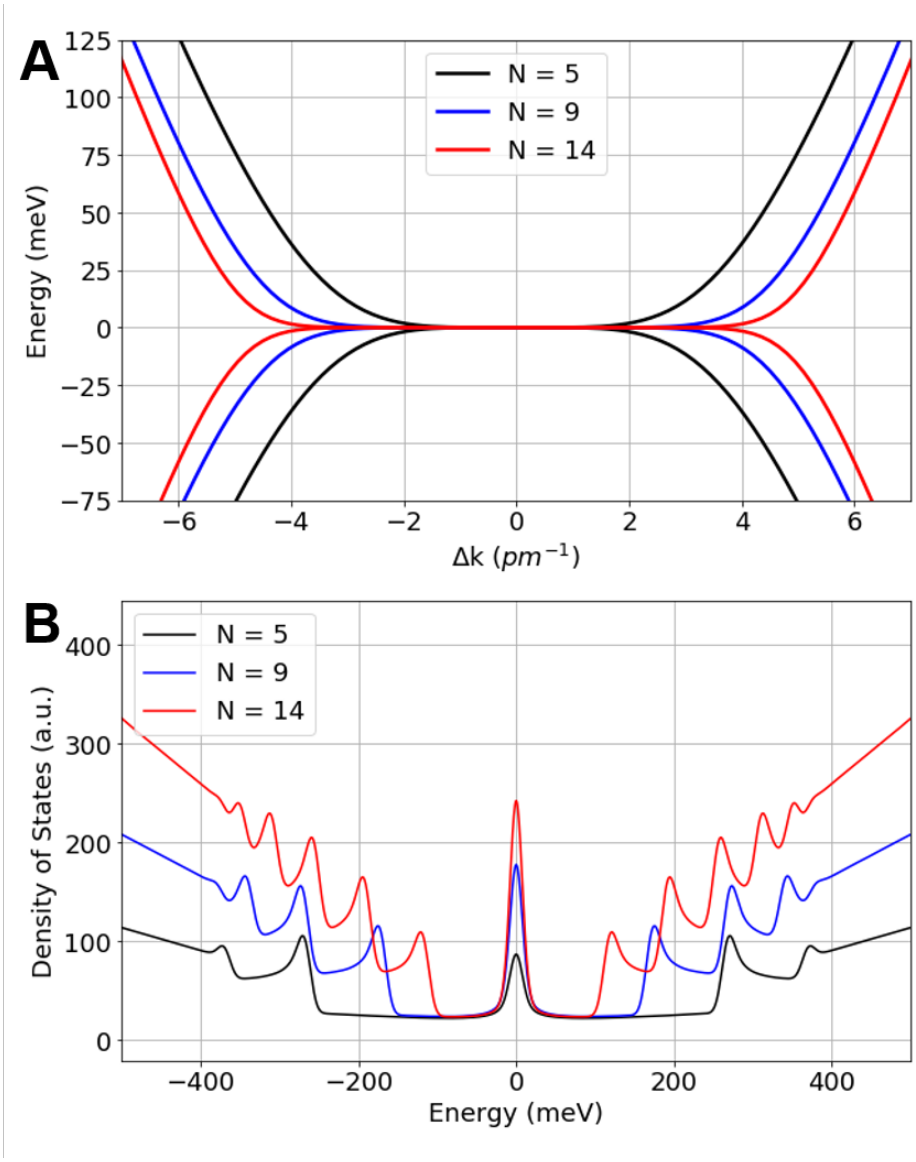

Figure 2.4: **a)** Band structure of ABC graphite stacks of N = 5, 9, and 14 layers. **b)** Density of states of the band structures above plotted together, showing a sharp peak at E=0 that grows as sample thickness is increased.

times improvement in surface roughness, resulting in extremely high mobilities >100,000 cm^2/Vs [23], greater than the usual ∼10,000 cm^2/Vs in graphene on SiO_2 [18, 19].

In addition to being a useful substrate, hBN can also be used to encap-

sulate air-sensitive materials. Many of the interesting phenomena discussed later in this thesis exist in materials that degrade in ambient conditions, either from oxidation, absorption of water, or other means. Measurement often requires bringing the material out into atmosphere before loading into a cryostat for measurement, so protective measures must be used to ensure the material doesn't degrade before measurement. A sensitive material can be sandwiched between two flakes of hBN, and the van der Waals forces that usually hold together layers of bulk van der Waals materials instead "seal" in the air-sensitive material. This allows handling of the sensitive material in ambient conditions, which is necessary for device fabrication and study by transport.

2.1.5 Transition Metal Dichalcogenides

Transition metal dichalcogenides (TMDs) are another layered structure consisting of a transition metal atom coordinated with six chalcogens (S, Se, or Te). The metal atoms arrange in a hexagonal lattice like graphene, but with an additional metal atom at the center of the hexagon (i.e. a trigonal lattice). Hexagonal nets of chalcogen atoms sandwich this transition metal layer, completing the structure of a single layer of a TMD. Stacking between these layers occurs via the same mechanism as in graphene and hBN: relatively weak van der Waals forces hold together the bulk, allowing for mechanical exfoliation of these layers.

Two primary stable phases exist for TMDs: the 2H and 1T phases. The main difference between these phases is the alignment of the chalcogen nets on either side of the transition metal layer. In the 2H phase, these chalcogenide layers exactly line up, resulting in an ABA-style stacking. This stacking has a mirror symmetry in the plane of the layer, however inversion symmetry is absent. In contrast, in the 1T phase the chalcogen layers do not line up, resulting in an ABC-style stacking. Electronically, a TMD in 2H phase will display semiconducting character while the 1T phase will display metallic character [38]. The 1T and 2H unit cells are shown in figure 2.5.

Of particular interest in this work are TMDs of the chemical form (Mo, W)(S, $Se)_2$. These materials are thermodynamically stable in the 2H phase, and indirect gap semiconductors in the bulk. Interestingly, they show a shift from indirect to direct gap as they are thinned down to a single monolayer, which has made them particularly interesting in optical studies of 2D materials [24]. This direct gap is found at the K and K' points, which are inequivalent by lack of inversion symmetry, making these materials interesting for valleytronic applications.

Because of their semiconducting nature, these materials have the ability to

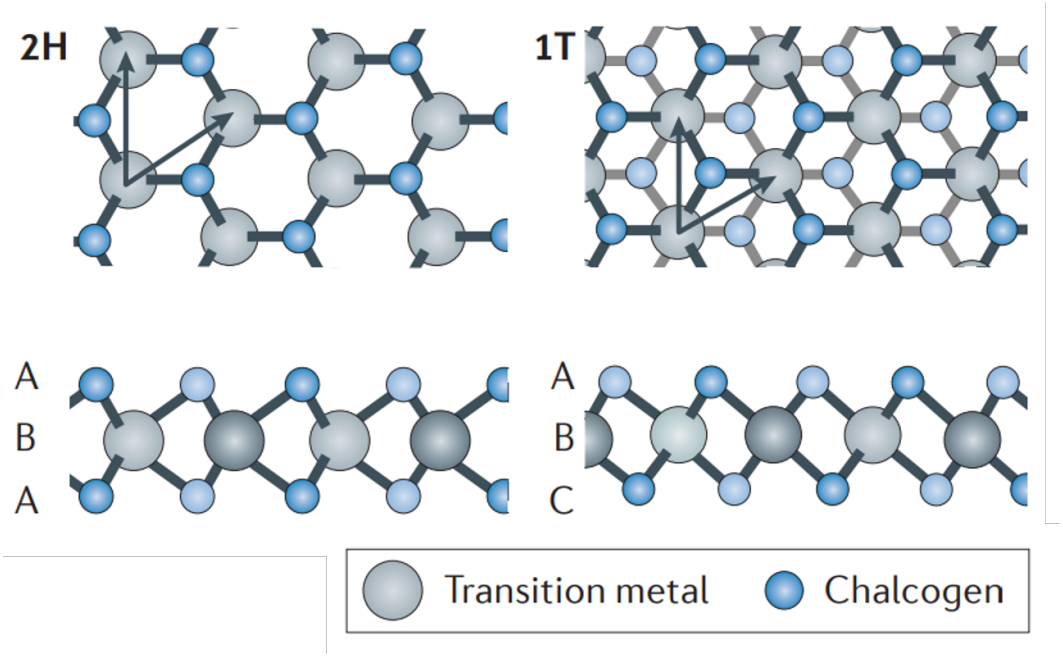

Figure 2.5: 2H and 1T phases of TMD monolayers. 2H phase exhibits semiconducting properties while 1T is metallic.

behave both as a gate dielectric and as a conductor depending on the applied gate voltage. In scanning tunneling microscopy (STM), a measurement technique used in abundance in this thesis and described in detail in section 3.4, an insulating sample ruins an experiment. TMD's can be used in place of insulating hBN as a substrate for other interesting 2D materials in experiments. Because of their small band gap, using a large bias voltage allows tunneling directly onto the TMD substrate, which would normally be impossible with an insulating substrate. Thus, TMDs have been the primary substrate used in STM experiments in this work.

2.1.6 Magnetic Materials

Much of the work of this thesis focuses on magnetism in 2D heterostructures. Materials demonstrating ferromagnetic order in the ultrathin limit have only recently been discovered, with simultaneous reports of magnetism in monolayer CrI_3 [16] and bilayer $Cr_2Ge_2Te_6$ [26] in 2017. Famously, the Mermin-Wagner theorem says magnetism should not exist in two dimensions, due to the diverging magnon density of states at finite temperature destroying any magnetic order [39], however the Ising model introduces a magnetic anisotropy that sup-

presses these magnetic fluctuations. CrI_3, and all ferromagnetic materials used in this work, displays this model of magnetism, which is described in-depth later in this chapter. $Cr_2Ge_2Te_6$, however, hosts Heisenberg ferromagnetism, which does not have a magnetic anisotropy. Hence magnetic order was only observed in the bilayer, while the Curie temperature (T_c, the temperature below which magnetic order is observed) extrapolates to zero in the thinnest limit. [26]

Chromium trihalides, such as CrI_3 and $CrBr_3$, are used extensively in this work. Both CrI_3 and $CrBr_3$ are Ising ferromagnets, with an easy axis perpendicular to the atomic planes. CrI_3 has a bulk $T_c = 61$K, which is lowered to 45K in the monolayer limit, and is a semiconductor with an indirect band gap of 1.53 eV in the monolayer limit [16, 40]. $CrBr_3$ has a bulk T_c of 37K that is only slightly lowered to 34K in the monolayer limit, and is also a semiconductor with an indirect band gap of 2.54 eV in the monolayer limit [25,40]. Figure 2.6b shows the structure of a single layer of these chromium trihalides. The monolayer consists of a halide-Cr-halide triple layer, with the halides forming edge-sharing octahedra surrounding the central Cr atom. These octahedral units form a hexagonal net that makes up the monolayer [41].

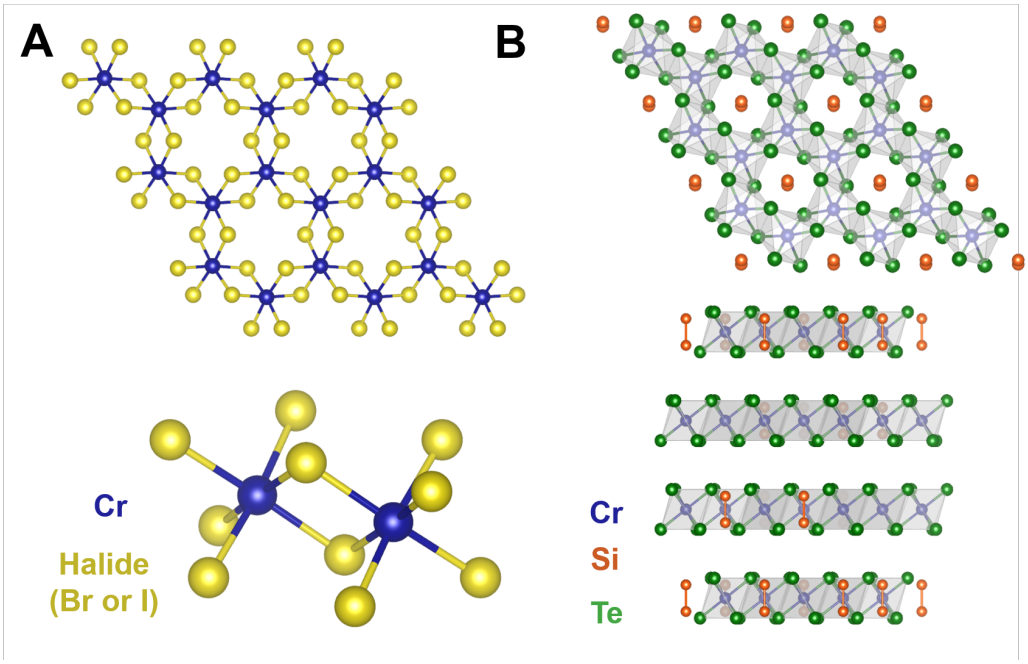

Figure 2.6: **a)** Crystal structure of $CrBr_3$ and CrI_3. **b)** Crystal structure of CST. A single layer consists of a quintuple layer of Te-Si-Cr-Si-Te.

These chromium trihalides differ in the magnetic ordering between adjacent layers. In CrI_3, spins are aligned within each layer, but these spins between layers align anti-ferromagnetically. This means flakes with an even number of layers should have zero net magnetization, while those with an odd number of layers should have some magnetization at zero external field. Huang *et. al* demonstrated this using technique that takes advantage of the magneto-optical Kerr effect. Briefly, this technique uses linearly polarized light reflected off the sample's surface, and the polarization of this light after reflection is recorded. The difference between the incoming and outgoing polarization is called the Kerr rotation (θ_k), and is directly proportional to the magnetization in the material. Huang *et. al* measured the Kerr rotation of samples with 1, 2, and 3 layers, and their results are shown in figure 2.7. Both 1 and 3 layers display a nonzero magnetization at zero applied magnetic field, with a hysteretic loop observed between forward and backward traces, a hallmark of a ferromagnetic state. In the bilayer sample, zero net magnetization was observed at zero applied external field, indicative of an anti-ferromagnetic state [16]. In $CrBr_3$ however, this is not the case. Bilayer $CrBr_3$ exhibits a magnetic hysteresis, indicating layers of this material align ferromagnetically [25].

In addition to CrI_3 and $CrBr_3$, ferromagnetic $CrSiTe_3$ (CST) is also used extensively in this work. CST is similar in structure to $Cr_2Ge_2Te_6$ (or $CrGeTe_3$), but exhibits Ising ferromagnetism instead of Heisenberg ferromagnetism, with an easy axis perpendicular to the atomic planes. CST has a bulk T_c of 33K, and is a semiconductor with an indirect band gap of 0.4eV [17]. The crystal structure of CST is shown in figure 2.6a. The Cr atoms form an underlying hexagonal lattice while the Te atoms coordinate in a slightly-distorted octahedron to these Cr. Two Si atoms are placed in the middle of the Cr-hexagon both above and below the Cr-layer, but not beyond the Te-layer. This forms a sandwiched structure of Te-Si-Cr-Si-Te when viewed from the side. Since there are no dangling bonds beyond the Te layers, these layers form a van der Waals stack, stacking in ABC style [42].

The last magnetic material I'll discuss is α-$RuCl_3$ (henceforth just $RuCl_3$), which is also used extensively in this work. Single-layer $RuCl_3$ is a Mott Insulator, exhibiting a Mott gap in the 4d band [43]. Mott insulating states often hold interesting magnetic phenomena [44], and $RuCl_3$ is no exception: the material hosts a zigzag antiferromagnetic ground state with a Néel temperature of 7-14K. Above this temperature, $RuCl_3$ may exhibit an exotic phase of matter known as the quantum spin liquid. This is a phase where spins are not aligned or anti-aligned, but instead are "fluid", fluctuating between many different degenerate ground states. The degeneracy of these ground states has a geometric origin: in lattices with a trigonal motif, electrons on atoms on the

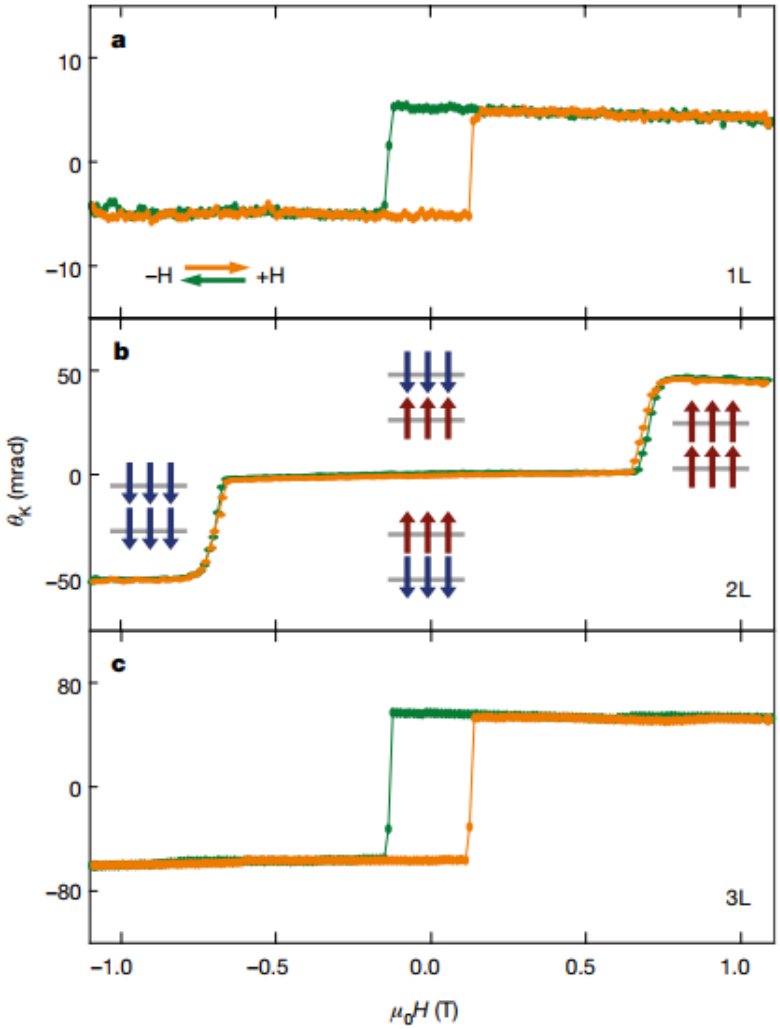

Figure 2.7: Kerr rotation of different thicknesses of CrI_3. **a)** Monolayer CrI_3 showing ferromagnetic hysteresis. **b)** Bilayer CrI_3 shows the antiferromagnetic interlayer coupling of ferromagnetic CrI_3 layers. **c)** Trilayer CrI_3 recovers the behavior of the monolayer. Data from reference [16].

three corners of the triangular unit can never be mutually anti-aligned. All combinations of 2-up, 1-down in this geometry are therefore degenerate [45,46]. $RuCl_3$ is an example of such a lattice: the spins are expected to order but are geometrically "frustrated", placing it in a quantum spin liquid phase. This has experimental support from neutron diffraction experiments performed by

Banerjee *et al.* [27, 28].

A summary of all materials used in this thesis is presented in the following table:

Material	**Type**	**Properties / Applications**
graphene	semi-metal	high mobility, linear dispersion
rhombohedral graphite	topological insulator	intrinsic flat bands on surface
CrI_3	semiconductor	Ferromagnetic monolayer, layered antiferromagnet
$CrBr_3$	semiconductor	Ferromagnetic monolayer, layered ferromagnet
$CrSiTe_3$	semiconductor	Ferromagnetic monolayer, layered ferromagnet
α-$RuCl_3$	Mott insulator	Antiferromagnetic, Kitaev quantum spin liquid
hBN	insulator	substrate for transport experiments
TMDs	semiconductor	substrate for STM experiments

Table 1: All 2D materials used in this study, including electronic properties and other noteworthy properties

2.2 van der Waals Heterostructures and Proximity Effects

In the previous section, I described a variety of different 2D materials that are used throughout this work, each displaying a rich electronic structure and interesting physical effects on their own. However, the true utility of 2D materials shines when you *combine* these materials. Stacking monolayers of different materials together allows researchers to design novel devices with a precise arrangement of materials along the stacking direction, choosing exactly which atoms to place next to each other to engineer new materials exhibiting the properties of all of the constituents. The layers in a heterostructure can interact, giving a device that is more than just a stack of materials with independent electronic properties. These devices are clean, as the exfoliated surfaces only ever contact the materials with which they are being stacked, giving device quality that is on par with sophisiticated, time-consuming techniques such as molecular beam epitaxy (MBE). van der Waals Heterostructures offer an additional flexibility over MBE: materials with large lattice mismatch can be

easily stacked, and the relative twist angle between stacked materials offers a new degree of freedom that is impossible in MBE-created devices.

A proximity effect is a phenomenon where one material inherits the properties of another neighboring material simply by being in close proximity to it. Atoms of the constituent materials are in direct contact, and typically short-range effects such as ferromagnetic exchange can impact the properties of all contacted atoms. In 3D materials this would only affect atoms at the surface, but in 2D materials everywhere is a surface, and the entirety of a 2D material can be affected by a proximity effect.

Many different proximity effects in 2D materials have been discovered to date. Heterostructures of graphene and hBN with very little rotational misalignment cause an electrostatic mismatch between the usually-symmetric A and B sublattices of graphene, causing the addition of a sublattice potential which opens a gap in the graphene spectrum. This was demonstrated experimentally by multiple research groups, famously creating a fractal pattern of topologically distinct insulating phases called the Hofstadter butterfly [47, 48]. Additionally, heterostructures of bilayer graphene and WSe_2 exhibited skewed Landau level crossings when a perpendicular electric field was applied, indicating inheritance of spin-orbit coupling in graphene due to proximity with the neighboring WSe_2 [34]. Even further, heterostructures of 1T'-WTe_2, a quantum spin Hall insulator, with $NbSe_2$, a 2D superconductor, exhibited simultaneously a quantum spin Hall edge state with a superconducting gap, indicative of proximitized superconductivity in a topological edge state [49].

In a later chapter, I'll discuss my own efforts towards realizing a magnetic proximity effect between graphene and several different 2D ferromagnetic insulators. For a better appreciation of the efforts of that work, I'd like to introduce several concepts central to magnetism and explain why we expect a magnetic proximity effect to possibly exist. In the following sections, I'll give a brief overview of the magnetic exchange effect, the Heisenberg and Ising models of magnetism, and the expected effects of magnetic proximity.

2.3 A Brief Overview of Magnetism

2.3.1 Magnetic Exchange Effect

Magnetism in materials describes the behavior of the material in response to a magnetic field. When a magnetic field is tuned, electrons in a material respond by changing the orientation of their individual magnetic moment called spin, and the behavior of these spins determines the type of magnetism in the material. The most common response to a magnetic field is paramagnetism, where

a material is weakly attracted by an externally applied field and does not form a permanent magnet in the absence of such field. The most well-known form of magnetism is ferromagnetism, where the spins in a material spontaneously align in the absence of an external magnetic field, forming permanent magnets.

Ferromagnetic exchange is an electron-electron correlation effect that is a consequence of the exchange effect, a quantum mechanical effect rooted in the Heisenberg uncertainty principle. The exchange effect refers to energetic contributions that result from wavefunction symmetry of fundamental particles. Fermions are defined by the symmetry of their wavefunctions, gaining an overall -1 sign on their wavefunction under particle exchange. The impact of this on the electronic structure of a material can be seen by considering the electron correlation as a small perturbation to the Hamiltonian. Using perturbation theory, the energy eigenstates for this system are:

$$E = \begin{cases} (E^0 + K) + J & \text{when } \Psi = \chi_{AS} \\ (E^0 + K) - J & \text{when } \Psi = \chi_S \end{cases}$$

where E^0 is the non-interacting system ground state energy, K and J are the Coulomb and exchange integrals describing the effects of electron correlation, and χ_S and χ_{AS} are symmetric (triplet) and anti-symmetric (singlet) spin states. The sign of J determines the magnetic behavior of the system: a positive J will result in the triplet state having energetic favorability, while a negative J will result in the singlet state being energetically favorable.

2.3.2 Heisenberg Model and Ising Model

We can rewrite the energy eigenstates in terms of the expectation value of the dot product of the spins $\langle s_1 \cdot s_2 \rangle = \frac{1}{2}(\langle (s_1 + s_2)^2 \rangle - \langle s_1^2 \rangle - \langle s_2^2 \rangle)$. For the singlet state, $\langle s_1 \cdot s_2 \rangle = -3/4$. For the triplet state, $\langle s_1 \cdot s_2 \rangle = 1/4$. In both of the above cases, the energy reduces to:

$$E = (E^0 + K + \frac{1}{2}J) - 2J \langle s_1 \cdot s_2 \rangle$$

All of the interesting physics is contained within this last term of the energy eigenstates. This is therefore often used as a simplified Hamiltonian of a magnetic system. Broadening our system from two particles to an infinite lattice of fermions on atomic sites, we can write the Hamiltonian as:

$$H = -\sum_{i,j} J_{ij} \vec{s_i} \cdot \vec{s_j} \tag{1}$$

where the sum is over all pairs of lattice sites i, j, and the tensor J_{ij} is a coupling constant between the spins on these sites. The factor of two is removed since the summation counts each pair of spins twice. This magnetic model is called the **Heisenberg model**.

Much work in this model is done characterizing J_{ij} for different lattices. The character of J_{ij} determines the magnetic properties of a material: $J_{ij}>0$ implies the material orders ferromagnetically while $J_{ij}<0$ implies it orders antiferromagnetically. Many different exchange models are used to find the characteristics of J: for example, the Hubbard model used often for antiferromagnetic systems gives $J = -t^2/U$ where t is a kinetic energy hopping term and U is a coulomb interaction strength. In the RKKY model for indirect exchange in metals, the coupling constant is $J \sim \frac{cos(2rk_F)}{r^3}$, which is oscillatory in distance between spins r and therefore can be either ferromagnetic or antiferromagnetic [2].

The Heisenberg model, however, fails in the 2D limit. As described in the famous Mermin-Wagner theorem, the magnon density of states diverges at finite temperature in two dimensions, and these spin fluctuations completely destroy long-range magnetism [39]. This instability of magnetism in 2D is actually a result of the isotropy of the Heisenberg model. Materials with anisotropic exchange interaction, say due to a crystalline anisotropy or spin-orbit interactions, can still behave ferromagnetically in the 2D limit. The **Ising model** of magnetism is a small simplification of the Heisenberg model, where instead of considering the spins as vectors, we consider the spins as scalars taking the values either -1 or +1, such that the idea of an easy-axis of magnetization is built in to our model. We can write the Ising model as:

$$H = -\sum_{i,j} J_{ij}\sigma_i\sigma_j$$
$$\sigma_i, \sigma_j = +1 \text{ or } -1$$

This is identical to the Heisenberg Hamiltonian in the absence of the $s^{\pm}$ terms, including only the $s_i^z s_j^z$ potion. Thus the eigenstates of the s^z operator are now eigenstates of the full Hamiltonian (unlike in the Heisenberg model). It was first solved in the 1D case by Ernst Ising in 1924, and in 2D by Lars Onsager in 1944 [50]. Ising's 1D model does not have any phase transition to a ferromagnetic state, however Onsager's 2D model does, with a Curie temperature proportional to the spin coupling constant:

$$T_c = \frac{2J}{k_B \ln(1+\sqrt{2})}$$

Why don't magnons destroy ferromagnetism in the 2D Ising model like they do in the 2D Heisenberg model? For starters, they are mathematically prohibited from existing in this model. A magnon is specifically an oscillation of the magnetic moment, which requires the moment to be able to exist in more than one dimension. Mathematically, the Ising model does not allow this. But real materials are not perfect Ising ferromagnets: their spins are not completely restricted to the easy-axis. Instead, there is an energetic cost for the spin to align to a different axis. This energetic cost is what allows magnetism to exist in these materials. The density of states for magnons in shifted in energy due to misalignment with the easy-axis of magnetization, causing these low-wavelength magnon states to be unpopulated entirely. Thus, the magnetic anisotropy in the system allows breaking of the Mermin-Wagner theorem, and allows ferromagnetism to exist in two dimensions.

2.3.3 Mean Field Theory

Solving the Heisenberg and Ising Hamiltonians for an infinite lattice is a difficult problem, however it can be simplified by considering the average exchange field felt by a single spin. If the spin configuration preserves lattice translation symmetry, as it does in a ferromagnetic state, then the exchange energy of all spins should be identical. We can replace the double sum over all lattice sites with a single sum over lattice sites with a "mean field" felt by each spin:

$$H = g\mu_B \sum_i \vec{s_i} \cdot \vec{B_{mf}}$$

$$B_{mf} = -\frac{1}{g\mu_B N} \sum_{i,j} J_{ij} S_j$$

The term B_{mf} describes an average field felt by a single spin in the lattice. Using this model in conjunction with an external magnetic field gives the full mean field Hamiltonian:

$$H = g\mu_B \sum_i \vec{s_i} \cdot (\vec{B_{ext}} + \vec{B_{mf}})$$

The system acts as a paramagnet in an external magnetic field, however the strength of the magnetic field is increased by an amount B_{mf}, which is usually orders of magnitude larger than the external magnetic field B_{ext}. This new effective magnetic field persists even at zero external applied magnetic field, giving rise to the magnetization at zero field. One would expect this mean field to be proportional to the sample magnetization, $B_{mf} = \lambda M$ [2].

2.3.4 Proximity Magnetization

Usually we view the Heisenberg and Ising models only concerning spins within a single material, *i.e.* in the bulk of a large crystal lattice extending indefinitely in all directions. However, at the interface between the ferromagnet and another material (like graphene), the electrons on the outermost layer of the ferromagnet are free to interact with electrons from the neighboring material. We still expect the exchange effect present in the ferromagnet to affect the neighboring layer in a similar manner as it would in the bulk. We can use a simplified Hamiltonian for this system:

$$H = -\sum_{i,j} J_{ij}\vec{S}_i \cdot \vec{S}_j + g\mu_B \sum_j \vec{S}_j \cdot \vec{B}$$

Here, i and j refer to atoms on the outermost layer of the ferromagnet and on graphene respectively. The first term is the Heisenberg exchange term, where J_{ij} are positive, interlayer exchange constants, which are different than the J terms seen in the isotropic Heisenberg model in the previous section. The second term is the Zeeman energy given by having electrons with spin in an external magnetic field $\vec{B}$.

Using the same concept as the mean-field approach above, we can write an effective magnetic exchange field B_{MEF}, which is the average field felt by a charge carrier in graphene due to the underlying ferromagnet:

$$H = g\mu_B \sum_j \vec{S}_j \cdot (\vec{B}_{MEF} + \vec{B})$$

$$B_{MEF} = -\frac{1}{g\mu_B N} \sum_{i,j} J_{ij} S_j$$

Later in chapter 4, I will discuss experiments towards realizing a magnetic proximity effect in 2D materials. In these experiments, heterostructures of graphene and several different 2D ferromagnetic materials are fabricated, and magnetotransport is used to measure quantities proportional to the magnetic exchange field between the two materials. In the next section, I will describe the techniques used to create these heterostructures.

3 Experimental Methods

In this section, I'll discuss the techniques used to create devices with 2D materials. First, I'll discuss mechanical exfoliation, which is used to thin a layered material from bulk down to the ultrathin limit. Then I'll discuss the dry transfer technique, which is used to pick up and stack different 2D materials to create heterostructures for measurement. Then I'll discuss many of the sensitive 2D materials used in this work, as well as techniques for protecting them from degradation.

I'll also give an overview of scanning tunneling microscopy and spectroscopy, which is the primary technique I used to measure the intrinsic flat bands in rhombohedral graphite. This is a sophisticated scanning probe technique that relies on quantum mechanical tunneling to create a picture of the atoms that make up a surface. I'll describe the physics that go into the tunneling current, as well as measurement techniques used to directly probe the density of states of 2D materials.

3.1 Exfoliation and Search

Thin 2D materials are typically create din two different ways: either they are grown using techniques such as chemical vapor deposition to create monolayers from gaseous constituents, or bulk layered crystals are thinned out using a technique called mechanical exfoliation. In this thiesis, I exclusively use exfoliation to create 2D materials for study. To create a 2D material using this technique, a bulk crystalline piece of a layered material (such as graphene in figure 3.1) is placed between two pieces of tape. Pulling apart this tape divides the material approximately in half by cleaving apart along one of the 2D crystal faces of the material [13]. This cleaving is preferred because the interplane bond cleaving energy is orders of magnitude smaller than the intra-plane cleaving energy, implying the material preferentially forms large-area layers of this material. This process is then repeated multiple times, thinning out the initial bulk crystal with each successive step. After

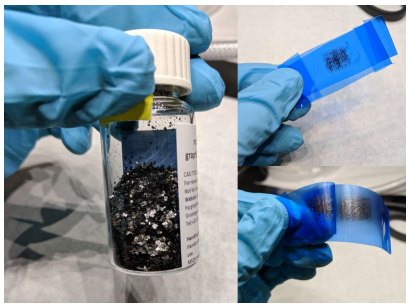

Figure 3.1: **Left:** bulk graphite flakes. Each flake contains many layers. **Right:** two pieces of tape sandwiching graphite that is ready to be exfoliated.

multiple cleavings, the 2D material forms a film consisting of many different thin crystalline fragments of the material, as shown in 3.1. Finally, the sample is exfoliated onto a chosen substrate (p-doped Si/ 300nm SiO_2 in most cases) by adhering the tape to the surface of the substrate, and is subsequently observed under an optical microscope.

Optical microscopy is primarily used to identify large-area thin flakes. The flakes have observable shifts in color that can be directly related to the thickness of the flake [51]. While this is not a concrete determination of layer thickness, it assists in finding choice flakes for further processing. Atomic force microscopy (AFM) or STM measurements can determine the thickness of a chosen flake and therefore determine the layer number of the flake. Additionally, Landau level symmetries change based on layer number, so electronic transport can also be used to confirm whether a given graphene flake is a monolayer. In practice, optical identification has proven to be a trustworthy tool to indicate thickness of a given flake.

Figure 3.2 shows optical images of flakes of graphene of varying thickness. The left image shows a 5x magnification and the right image shows a 100x magnification of the area in the rectangle. Terraces of constant optical constrast and thus constant thickness are labeled by the number of graphene layers. In my time here, I have written a program that measures the optical constrast of a flake (defined as $c = \sqrt{r^2 + g^2 + b^2}$) relative to the background light level, and can deterministically classify a graphite flake as 1, 2, or 3 layers of thickness. This program is used by most graduate students exfoliating graphene in our lab, and others on campus.

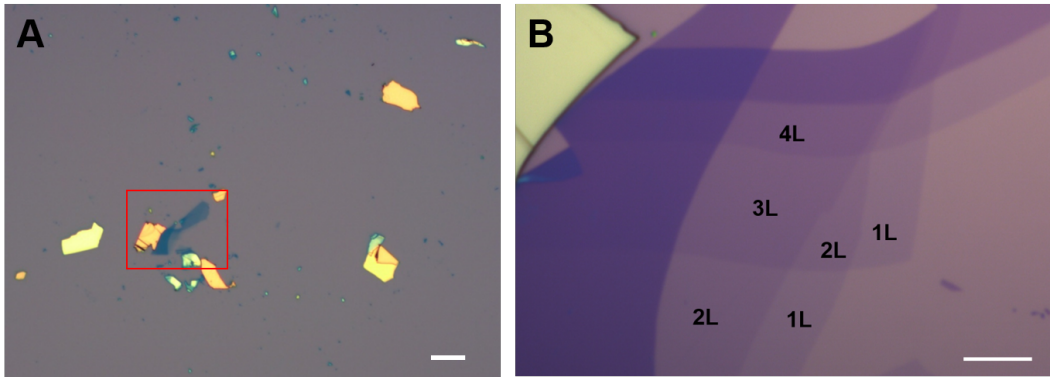

Figure 3.2: Pictures of exfoliated flakes of graphene indicating thickness in number of layers (L). Left shows a 5x image while the right shows a 100x image. Scale bar is 50 μm on the left, and 5μm on the right.

3.2 Dry-transfer Technique

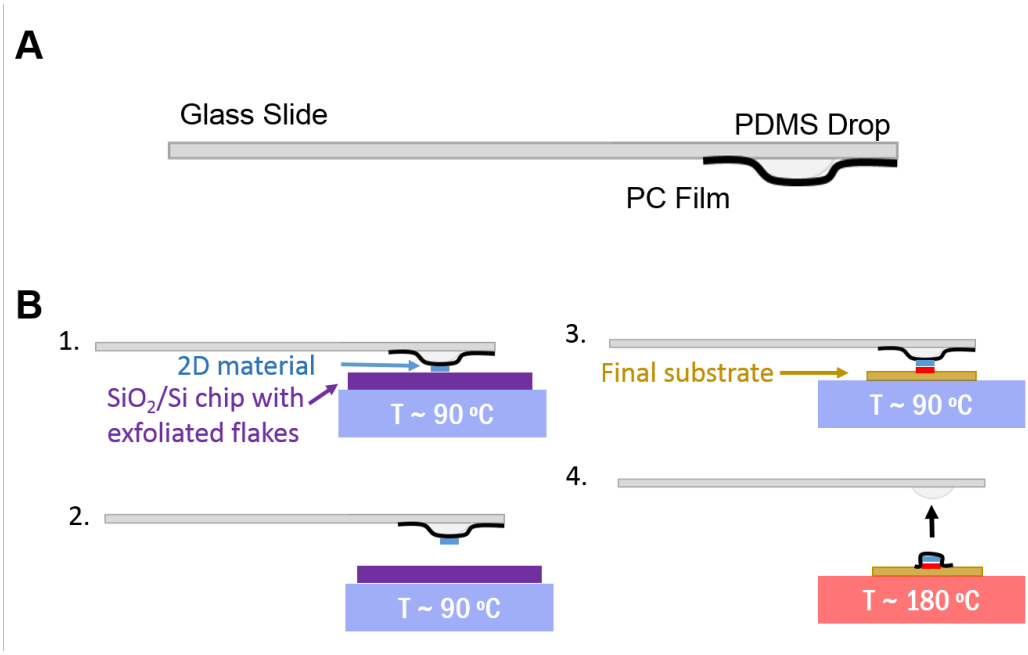

Figure 3.3: a) The transfer slide used to stack 2D materials. It consists of a glass slide with a PDMS drop mounted on it, and a thin PC film over top the droplet that contacts and picks up the 2D materials. b) Schematic of the typical transfer process. The transfer slide is brought into contact with the 2D material while the stage is heated to 90°. The slide is then lifted, lifting the 2D material with it. This is repated for any number of 2D materials. Set down occurs at 180°C, where the PC liqufies, leaving behind the stack.

Creating heterostructures of exfoliated 2D materials requires a method to pick up and stack thin pieces of these materials easily. Many different methods have been developed, including wet methods as described in reference [52]. Here, we use an all-dry polymer stamp to pick up and transfer thin pieces of 2D materials [53]. The stamp, shown in figure 3.3, consists of a thin film of polycarbonate (PC) on top of a bead of poly-dimethylsiloxane (PDMS) that is mounted on a glass slide. A thin film of PC is made by dissolving the polymer in chloroform and sandwiching the solution between two glass slides, which are then rapidly slipped apart leaving a thin film. Small squares of this film are picked up using Scotch tape and placed on top of a PDMS droplet that has been mounted on a separate glass slide. A diagram of the resulting structure, called the transfer slide, is shown in figure 3.3a and is used to pick

of 2D materials and stack them.

The PC film acts as a the "pick-up" layer, bonding to the 2D material in order to lift it off the SiO_2 surface. The PDMS is a soft stage for the PC film, enabling gentle contact to the 2D material without cracking the flake. While the PC film completely liquifies around 180°C, it becomes "sticky" around 90°C, becoming more likely to adhere to desired 2D materials. The entire procedure for stacking 2D materials is shown in fiigure 3.3b. The transfer slide is first brought into contact with the desired 2D materal while the stage is heated to 90°C, and this 2D material is picked up by simply lifting the stamp. This step can be repeated with subsequent 2D materials, allowing for the creation of complex structures of multiple different 2D materials. Once the complete stack has been picked up by the polymer stamp, the stamp is then brought into contact with the desired final substrate and heated to 180°C. This causes the PC film to liquify and delaminate from the PDMS surface. The glass slide is then lifted, leaving behind the heterostructure with a PC film on top. This film is then washed away using chloroform.

The entirety of this process is performed underneath a microscope to allow precise alignment of 2D stacks. The polymer stamp is completely transparent, so a wide field microscope objective can be used to look through the stamp and see flakes of 2D materials on the substrate below. Flakes that have already been picked up usually appear as slightly opaque portions of the stamp, with opacity being proportional to flake thickness. It is generally impossible to see isolated monolayers of a 2D material on the stamp, however small defects on the surface of the polymer film or neighboring thicker flakes that have been coincidentally picked up may be used to triangulate the location of the monolayer and allow accurate positioning of the flake. The glass slide is mounted on a micromanipulator, allowing for $\sim 1\mu$m precision with flake alignment.

One minor variation of this procedure involves using poly(propylene carbonate) (PPC) instead of the usual PC film. The primary advantage is decreased temperature during pick up and set down: pick up using PPC occurs around 40°C and set down occurs around 90°C. For materials that degrade at elevated temperatures, using PPC is a requirement to allow any heterostructure fabrication. Another advantage is that PPC can be removed by vacuum anneal instead of dissolution with a harsh solvent. This is advantageous for materials where contact to solvent may hurt device quality, and for air-sensitive materials that cannot be brought into ambient conditions to the fume hood for polymer removal. It is worth noting that PPC does not bond well to every 2D material, graphite is a notable example. For this reason, it cannot be used for every heterostructure.

3.3 Air-Sensitive Materials

All of the 2D magnetic materials used in this study degrade when exposed to either air, heat, light, or some combination of the above. Simple experiments to determine degradation pathways were performed for each material, and I'll quickly overview the results of these experiments. At the end, I'll summarize the degradation pathways for each material, and discuss techniques used to avoid degradation.

3.3.1 Degradation of Magnetic 2D Materials

CrI_3 degrades rapidly in ambient conditions under illumination with a white light source. Over the course of a few seconds under a microscope, the CrI_3 flakes appear to completely disintegrate. This is caused by CrI_3 absorbing water in atomsphere, given by the following chemical equation [54]:

$$CrI_3 + 6\,H_2O \xrightarrow{\text{Light}} Cr(H_2O)_6{}^{3+} + 3\,I^-$$

This degradation is aided by a light source. To confirm this, we observed the degradation of a CrI_3 flake under an optical microscope in real time. The rate of degradation decreased significantly when the light source power was at a minimum, and increased when at a maximum. Additionally, using higher magnification and focusing on the flake caused an increase in degradation rate.

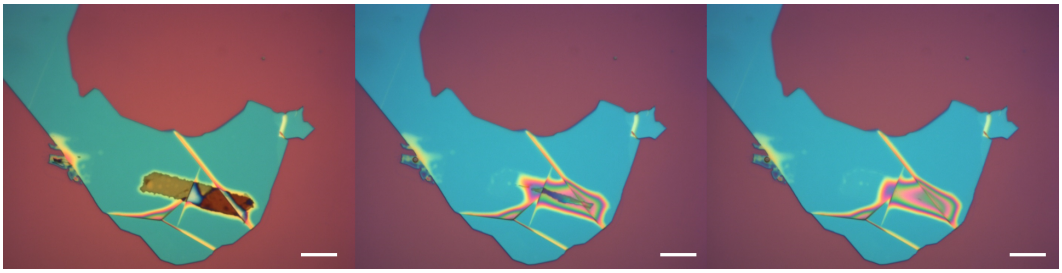

Figure 3.4: Degradation of CrI_3 under illumination.CrI_3 was capped on one side with hBN, and fully degraded over the course of 3 minutes in regular illumination. Scale bar is 5 μm in all images.

Figure 3.4 details the degradation of a flake of CrI_3. In the pictures shown, hBN is used to cover the flake in a fruitless attempt to protect it from ambient conditions. In this case, a single wrinkle in the hBN flake created a channel for H_2O to reach the flake, however in practice even the inherent roughness of SiO_2 is enough to allow H_2O to reach the CrI_3 flake and cause degradation.

$CrBr_3$ degrades in an identical manner as CrI_3, however the rate of this degradation is much slower. Figure 3.5 shows degradation of $CrBr_3$ and CrI_3 on a similar time scale with similar light conditions in ambient conditions. CrI_3 degrades entirely in this time frame, while $CrBr_3$ only has minor degradation. After 20 minutes, $CrBr_3$ finally starts showing signs of degredation.

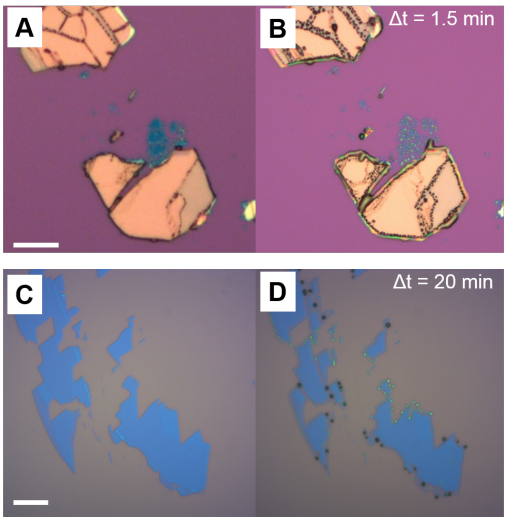

Figure 3.5: Degradation of CrI_3 and $CrBr_3$ under illumination in ambient conditions. **a-b)** shows degradation of CrI_3 while **c-d)** shows degradation of $CrBr_3$. CrI_3 degrades on a much faster time scale than $CrBr_3$. Visibile degradation was observed before the microscope could even be brought into focus for CrI_3. Scale bar in top images is 20 μm, scale bar in bottom images is 10 μm.

$CrSiTe_3$ degrades at high temperatures (T>150°C) over a short duration in ambient conditions. Under an optical microscope, small bumps are visible on the surface of the CST flake (as seen in figure 3.6), indicating a lack of atomic smoothness originally present in 2D layers. Many of the fabrication techniques used (e.g. baking electron beam resist) require high temperatures in ambient conditions, thus posing an obstacle to device fabrication with CST. To combat this, we use a lower maximum temperature of 100°C for any nanofabrication steps with devices including CST. Although this may have detrimental effects on the quality of devices produced, we found these effects were not detrimental to the success of our devices.

It is worth noting that the dry-transfer technique described above requires temperatures in excess of the aforementioned 150°C limit. This portion of the procedure is performed inside of a nitrogen glovebox, and the CST appears to be stable under these conditions. We therefore hypothesize that CST exposed to heat in ambient conditions oxidizes to form Cr_2O_3, thus forming the small bumps on the surface and discoloring the flakes.

$RuCl_3$ degrades under high temperatures, regardless of external conditions. Figures 3.6 and 3.7 shows two conditions through which $RuCl_3$ has been observed: annealing at 350°C in a vacuum, and heating to 180°C in an N_2

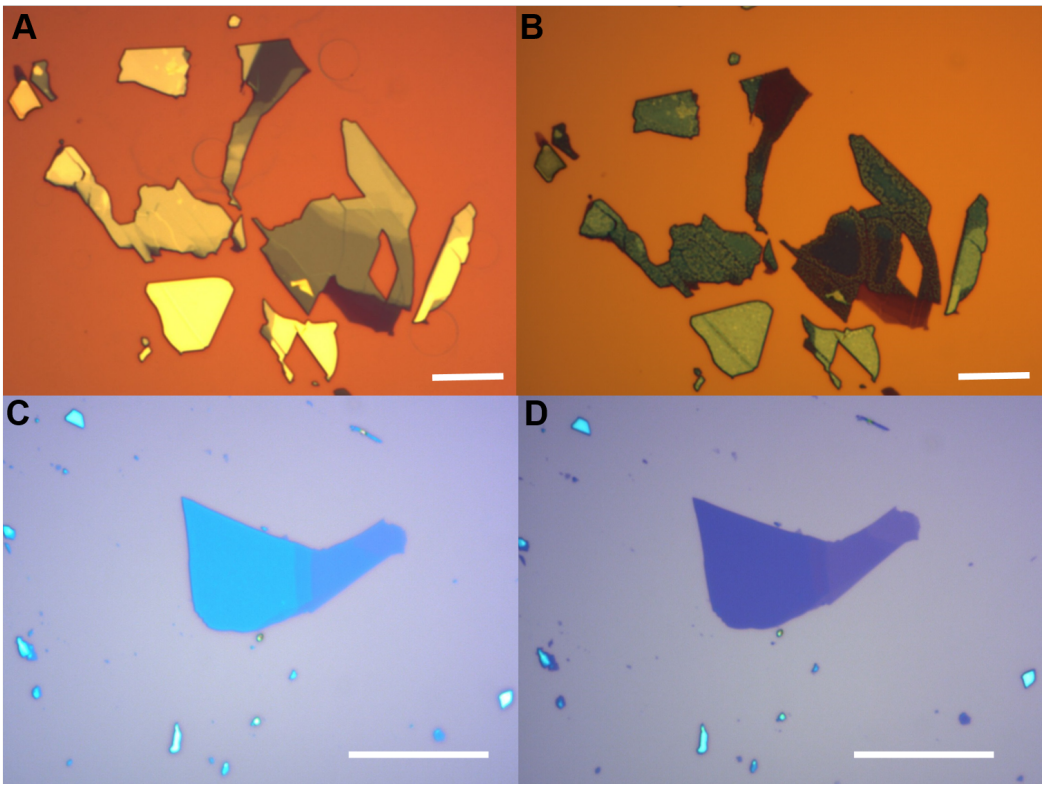

Figure 3.6: Degradation of CST and $RuCl_3$. **a)** CST after heating to 180°C in a N_2 environment.**b)** CST after heating to 180°C in ambient conditions. Scale bar for both images is 10 μm **c-d)** $RuCl_3$ before (c) and after (d) heating to 350°C in a vacuum annealer. Scale bar in both images is 20 μm.

environment inside the glovebox. The former causes an obvious visible degradation: the light blue hue of the $RuCl_3$ shifts to a purple color, indicating some structural change of the material. Changes of this type can be associated with either the material thinning out (as thinner materials usually appear more purple on the SiO_2/Si substrates), or a structural change of the material. Neither of these outcomes are desireable.

Figure 3.7a-b shows a graphene/$RuCl_3$/graphite heterostrucure. The AFM images show an extremely rough surface, indicative of contaminants trapped at the interface between either graphene and $RuCl_3$ or $RuCl_3$ and the underlying graphite. When creating heterostructures, bubbles like this are often found due to contaminants on the surface becoming trapped as the van der Waals forces start to attract the two 2D layers, leaving nowhere for the contaminants to go. This can usually be avoided by heating sufficiently slowly, which allows contact

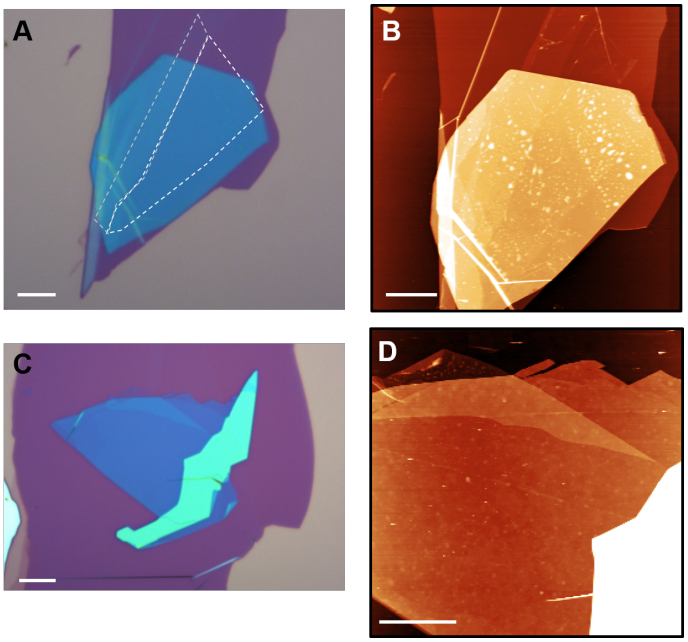

Figure 3.7: Two devices made using $RuCl_3$ and graphite. **a)** Optical image showing a graphene-$RuCl_3$-graphite heterostructure made using PC. The graphene is outlined in white, while a thicker portion is outline in grey. **b)** AFM image of this stack, showing large bubbles across the $RuCl_3$, indicating degradation. **c)** a $RuCl_3$-graphite heterostructure made using PPC. **d)** AFM of this heterostructure, showing minimal degradation of the $RuCl_3$. Scale bar is 5 μm in all images.

between the two layers to occur slowly, "ironing" out any contaminants that may otherwise become trapped. The top portion of the heterostructure in 3.7a-b shows a section with graphene/graphite overlap (i.e. no $RuCl_3$ present), and interfacial bubbles are absent in this portion of the stack. This indicates that stacking was sufficiently slow to prevent formation of trapped contaminants, and that these bubbles on the surface are likely formed from degradation of the $RuCl_3$. To further test this, a $RuCl_3$-graphite heterostructure was fabricated using PPC instead of PC, which has a lower set down temperature of $90°C$ (as opposed to 180° for PC). The resulting heterostructure and AFM images are shown in figure 3.7c-d. This stack showed decreased surface roughness, indicating a substantial decrease in the amount of $RuCl_3$ degradation that had occurred.

The degradation pathways for all air-sensitive materials used in this thesis are summarized in the following table:

Material	Degradation	Notes
CrI_3	Air + light	Rapid degradation
$CrBr_3$	Air + light	Slower degradation than CrI_3
$CrSiTe_3$	Heat + Air	
α-$RuCl_3$	Heat	Degradation not always apparent

Table 2: Air-sensitive materials used in this study, including the degradataion pathway.

3.3.2 Techniques for Handling Air-Sensitive Materials

Because of the above concerns, many special considerations must be made in order to allow study of air-sensitive materials by electron transport or STM. In the followin, I describe many precautions taken when handling air-senstive materials, as well as device design considerations for different degradation cases.

All air-sensitve materials are handled in a N_2 environment inside a glovebox. H_2O and O_2 levels are carefully monitored, and are found to be $\sim$1 ppm, minimizing degradation of materials by oxidation or water absorption. All bulk crystals are stored in the glovebox, and exfoliation of air sensitive materials is performed there as well. An optical microscope in the glovebox is used to search exfoliated materials for suitable flakes for stacking, and a dry-transfer station also in the glovebox is used to create the heterostructures. For many devices, every step of device fabrication can be done entirely inside the glovebox. For devices measured by scanning tunneling microscopy, the sensitive material will never see ambient conditions: the PPC layer left behind from transfer is annealed in vacuum, then the sample in transported in a N_2-suitcase to the STM and placed in UHV. For devices measured by electron transport, unavoidable exposure to ambient conditions occurs, as the sample must be wirebonded and loaded into the cryostat for measurement.

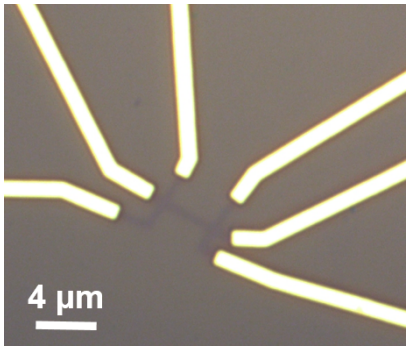

Figure 3.8: A pre-patterned graphene device, ready for transfer of an air-sensitive material.

One tool for minimizing exposure of air-sensitive materials is to pre-pattern devices before transfer of the air-sensitive material. Air-stable portions of the device can be stacked and any necessary fabrication can be performed before transferring the air-sensitive material onto the device. For the purposes of this work, this usually involves creating a graphene/hBN heterostructure, evaporating metal contacts and shape-etching the graphene into a Hall bar geometry, and then rigorously cleaning the resulting stack before transfer of the air sensitive material. An example of a device made with such planning in mind is shown in figure 3.8.

Observing the proximity effect requires a clean interface between the two materials. Fabrication and stacking can cause many contaminants on the surface due to resists and other polymers coming into direct contact with the graphene layer. It is therefore important to perform many cleaning steps to ensure the best possible interface quality between graphene and its proximitizing 2D material. To do this cleaning, an AFM-based cleaning method is employed [55]. Utilizing the contact mode of the AFM, multiple scans are made across the device, and any loose debris the tip contacts during these scans is removed from the surface. This debris is pushed to the sides of the scan area by the tip, cleaning the graphene surface in preparation for transfer of the magnetic material. Downward force of the AFM tip and the scan speed can both be adjusted in order to push off any heavier contaminants on the surface.

Figure 3.9 shows a graphene device both before and after AFM cleaning. The surface roughness of the device is 0.08 nm when the underlying SiO_2 'waviness' is subtracted out. This means the device is well cleaned and ready for measurement or transfer of the proximitizing material.

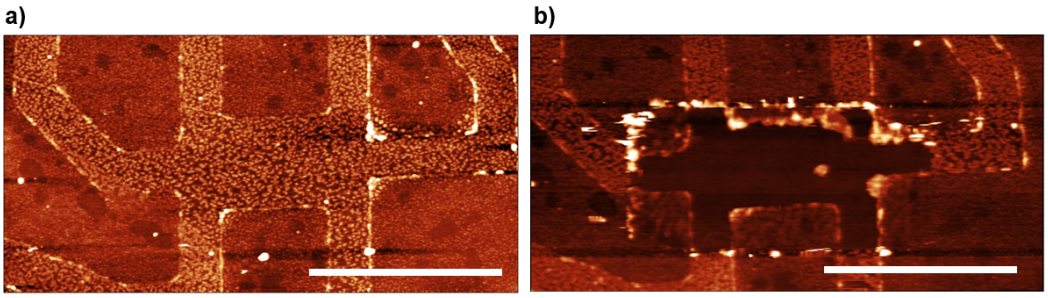

Figure 3.9: A graphene Hall bar both before and after cleaning using contact-mode AFM. The bright spots are contaminants on the surface of the sample. With the exception of one large contaminant, the graphene Hall bar is completely cleaned using this method. The scale bar is 5 μm in each picture.

Oftentimes air-sensitve materials must be completely encapsulated to protect them from the environment. The primary example of this is CrI_3, which will very readily absorb water from the air and degrade even when covered on one side with a large sheet of hBN. The two-sided encapsulation with hBN allows the van der Waals forces between the two hBN layers to seal the air-sensitive material inside, creating a completely enclosed area where there exist no pathways for atmosphere to reach the sensitive material.

This clearly poses a problem for study with transport: without any exposed graphene it is impossible to make the usual top-contacts that allow measurement of the device. However, it is possible to etch through the hBN to reveal an edge of the graphene underneath. Metal contacts can be evaporated onto this edge, and contact the graphene from within the plane of the graphene. These style of contacts have actually shown to have lower contact resistance, since it involves injecting the electrons directly into the open, dangling bonds on the edge of the graphene layer. This was first demonstrated by Wang et. al [56].

These above techniques are the primary tools used to minimize exposure of 2D ferromagnets to the conditions that cause their degradation. In chapter 4, I'll describe how various combinations of these techniques are used to create magnetic proximity devices to be measured by magnetotransport.

3.4 A Brief Introduction to STM

In the last two years of my research, I have used scanning tunneling microscopy and spectroscopy (STM/STS) as my primary measurement technique. STM is a microscopy technique that probes the surface of a conducting material. An atomically sharp tip is brought into close proximity with the sample surface, typically less than a nanomenter, using piezoelectrics to finely control the tip height, depicted in figure 3.10. When a small DC bias V_s is applied to the sample, a current on the order of nanoamperes is established between the tip and sample. Classically, this current is forbidden, since a vacuum gap exists between the tip and sample which acts as a potential barrier. However at small tip-sample separations d, quantum mechanical tunneling can occur, and a tunneling current of the order of a few picoamperes can be established.

This technique offers many advantages to researchers. The tunneling current depends, among other things, on the density of states in the sample: a larger density of states means there are more electron states available for tunneling and thus a larger tunneling current. A raster of the tip over the sample gives a spatially-resolved map of the sample's local density of states (LDOS), and since majority of a material's electron density is over the positions of its

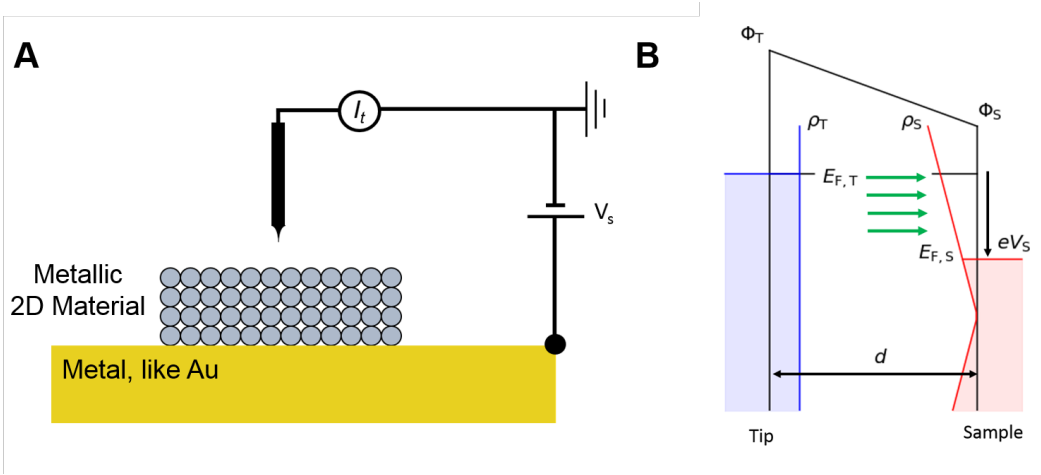

Figure 3.10: **a)** Diagram of the STM experimental setup. An atomically sharp tungsten tip is brought within a nanometer of a metallic surface. A bias is applied to the sample and a tunneling current can be measured. Atoms are not drawn to scale. **b)** Energy diagram of a typical tunneling measurement. The Fermi level of the sample is shifted downward by eV_s. Tunneling can occur in the area marked by green arrows. Diagram courtesy of Dacen Waters.

atoms, this gives us a map of the atomic lattice of the surface. Additionally, measurement using a lock-in technique allows researchers to directly probe the density of states, and create spatially-resolved maps of the electronic structure of a material.

In the following, I'll start with a brief description of tunneling, and give a basic model of tunneling in an STM that is sufficient to understand the results of this thesis. Then I will discuss several of the operating modes used within this thesis, including constant current topographic scanning and single-point spectroscopic measurements to extract a sample's density of states. Lastly, I will discuss some details of practical STM: what instrumental effects cause spectral broadening, what considerations need to be made when fabricating a sample, what care must be taken to ensure the highest quality measurements, and some techniques we use to perform measurements on 2D material systems.

3.4.1 Tunneling Current

The one-dimensional potential barrier is a classic problem seen in any introductory quantum mechanics course [57]. In this problem, a free electron with energy E incident on a potential barrier $\Phi > E$ with width d can pass through

such a barrier given d and Φ are sufficiently small. This process is known as tunneling, and is the primary mechanism by which an STM establishes a current between the tip and sample.

In a real STM, a metallic tip is separated from a metallic sample by a vacuum gap. An electron residing in the electronic states of the tip can tunnel across the vacuum gap into the electronic states available in the sample, as depicted by the green arrows in figure 3.10b. The barrier height is given by the average work functions of the tip and sample, $\Phi = \frac{1}{2}(\Phi_T + \Phi_S)$. The probability this tunneling occurs is given by the transmission coefficient, $T(E, V_s, d, \Phi)$. Using the Fermi level of the tip as the zero level of our energy, the tunneling current can be expressed as [58]:

$$I_t = \frac{4\pi e}{\hbar} \int_0^{eV_s} \rho_{tip}(\epsilon)\rho_{sample}(\varepsilon - eV_s)T(\epsilon, V_s, d, \Phi)d\epsilon \tag{2}$$

Here, ρ_{tip} and ρ_{sample} are the density of states of the tip and sample respectively. In the above, the effects of a nonzero temperature have been excluded. They can be introduced via the inclusion of Fermi-Dirac distributions centered around the Fermi level for the tip and sample. However, measurements are performed at T = 4K, and, for the purpose of this thesis, the distributions effectively act as step functions that select the integration window written above. Minor effects due to thermal broadening are mentioned later in this section. $T(\varepsilon, V_s, d, \Phi)$ describes the probability that the tunneling event will occur, as is given by the equation:

$$T(\varepsilon, V_s, d, \Phi) \propto \exp\left[-2d\sqrt{\frac{2m}{\hbar^2}\left(\Phi + \frac{eV_s}{2} - \varepsilon\right)}\right] \tag{3}$$

The term in parentheses is an effective barrier height, and can be deduced geometrically from figure 3.10.

From the above equations, it can be noted that the tunneling current depends on both the tip and sample density of states. Typically we assume the tip density of states is constant like a perfect metal, however it is possible that small features on the tip or contaminants near the apex of the tip can change this. Thus it is necessary to repeat all measurements with multiple different tips to ensure features measured actually come from the sample itself. This is accomplished by *in situ* tip forming on gold that is nearby the sample being measured, whereby the tip is intentially dipped into the gold surface while pulsing a large DC voltage. The tip is withdrawn, and Au atoms are either picked up or shed off of the tip. This process is repeated multiple times until a new, atomically sharp tip is formed.

3.4.2 STM Topographic Imaging

By far the most common mode of STM operation is the constant-current imaging mode. In this mode, the bias voltage V_s between tip and sample is held constant, and, using a feedback loop, the tunneling current is held at a desired setpoint I_t by adjusting the height of the tip. The tip is then rastered over top of the sample, and any features that would cause a change in the tunneling current, like variations in the local density of states or physical height changes on the sample, cause the feedback mechanism to withdraw the tip to maintain the same setpoint current. By recording the height changes of the tip, a map of the surface topography can be generated.

This technique is well known for its ability to create high-resolution maps of the atomic lattice of the surface of a sample. In regions where the sample density of states is large, say over locations of atoms in the lattice, tunneling current is enhanced and the tip withdraws in order to maintain constant current. Similarly, in areas where the density of states is low, say between atoms, the tip must move closer to maintain this same current. Thus the generated image shows a map of the atomic locations on the surface.

Figure 3.11 shows two atomic resolution images I've taken using this techinque. The first shows the surface of rhombohedral graphite, where the top layer consists of a hexagonal net of carbon atoms. In this image, the bright spots corresponding to atomic locations on the surface show an apparent trigonal symmetry, instead of the hexagonal symmetry of the lattice being measured. This results from a high density of states on only one sublattice of the surface states of rhombohedral grahpite, while the other has its states pushed to higher energies outside of the tunneling window. The sublattice with a drastically reduced density of states appears dark in comparison. The second image shows a graphene/WSe_2 heterostructure. Here, a graphene lattice is visible as a small hexagonal grid, but overlaid on top of this is a Moiré resulting form the low rotation angle between graphene and WSe_2. The high points of this pattern correspond to locations where the graphene and tungsten atoms lay directly over top one another, while the low points correspond to locations where the lattices do not align and atoms can pack more tightly. This is a particularly short-range effect for graphene and WSe_2 due to the large incommensurability of their lattices, and is only visible for small rotations less than $\sim 10°$. For materials with similar lattice constants like graphene and hBN, or materials with identical lattice constants but a slight rotation between them like twisted bilayer graphene, this Moiré is a much longer range effect, often encompassing hundreds or thosuands of unit cells.

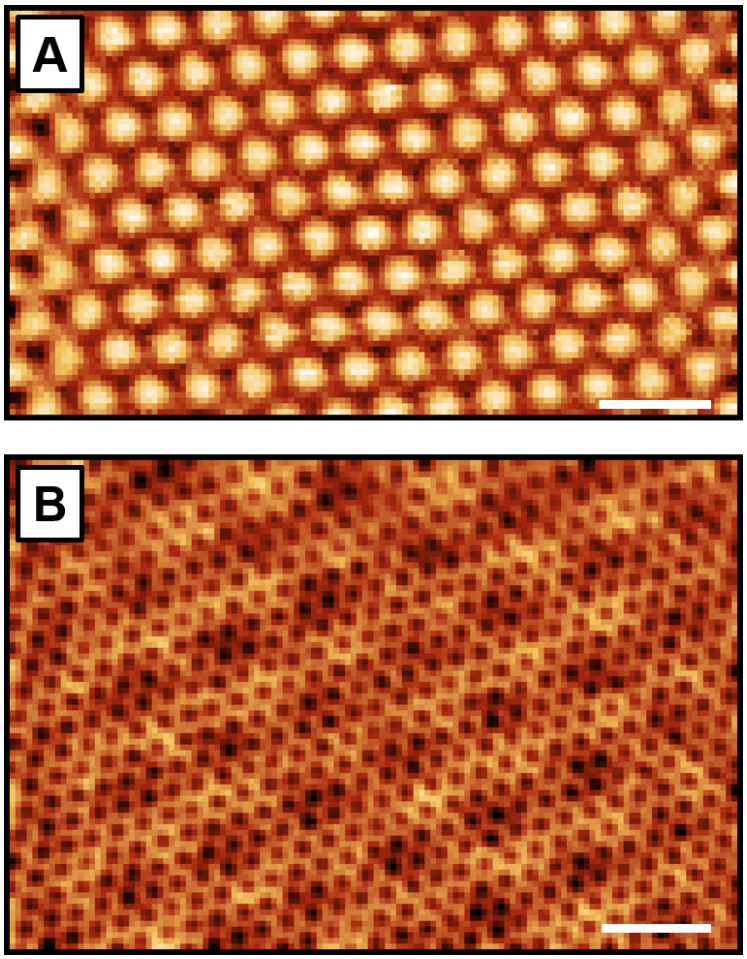

Figure 3.11: **a)** Atomic resolution image of the rhombohedral graphite surface. Scale bar is 5 $\mathring{A}$. **b)** Atomic resolution image of graphene on WSe_2 with an approximately 8° rotation. A small moiré is visible. Scale bar is 10 $\mathring{A}$.

3.4.3 Scanning Tunneling Spectroscopy

The tunneling current descibed in equation 2 describes the integrated local density of states. Oftentimes we are interested in measuring the sample's density of states directly. We can directly probe the differential conductance, dI_t/dV_s, to extract this information. In this measurement, the tip is held over a fixed lateral position of the sample at a fixed height, and the sample bias V_s is varied. A small AC modulation voltage $V_M \cos(\omega t)$ is added on top of the DC sample bias, and the resulting current $I_t = f(V_s + V_M \cos(\omega t))$ is measured using a lock-in amplifier. The signal from the lock-in gives only the

portion of the current at the frequency ω, which is directly proportional to the differential conductance dI/dV.

To understand what this means, consider the derivative of the tunneling current equation 2 above. A small increase in sample bias dV_s moves the samples states downwards in energy, giving a contribution dI at the upper limit of the integral $\varepsilon = eV_s$. Thus a simple appoximation of the differential conductance is given by:

$$dI_t \approx \frac{4\pi e}{\hbar}\rho_{tip}(0)\rho_{sample}(eV_s)T(eV_s, V_s, d, \Phi)dV_s$$

This neglects that the current contributions of the lower energy levels are modified by a reduced transmission factor (i.e. their effective barrier height has now increased). In this work, the work functions of the tip and sample are much larger than the sample biases used, and the transmission factor can be considered constant for all V_s. Additionally, for a perfectly metallic tip, ρ_{tip} is also constant, meaning that for measurements reported in this work, we can assume:

$$\frac{dI}{dV} \propto \rho_{sample}(eV)$$

By varying the bias voltage of the sample, the density of states around the Fermi level can be measured. This resulting plot, called the tunneling spectrum, is often qualitatively compared to similar plots to show changes in the density of states at different positions in the unit cell of a crystal, or at different positions in long-range structures such as Moiré patterns between 2D materials.

To meausre dI/dV directly, we use a lock-in amplifier to measure only the portion of the tunneling current oscillating at the same frequency as our modulation voltage. This quantity is dirctly proportional to dI/dV, as can be inferred from figure 3.12b showing a hypothetical I-V curve. The derivative is smaller at V_1 than V_2, and the resulting ΔI_1 is smaller than ΔI_2. Thus I_M, the amplitude of the tunneling current oscillating at frequency ω, is directly proportional to the slope of the I-V curve, dI/dV. A more formal derivation of this showing an exact relation is given in reference [58].

Source of broadening in STS

The measurement scheme itself introduces a few sources of broadening that are important to note. First, while measurements are performed at low temperatures to reduce thermal broadening, they are never completely removed.

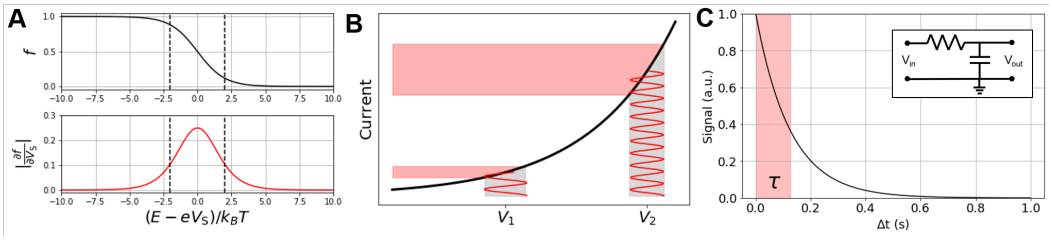

Figure 3.12: Sources of Broadening in STS measurements. **a)** Thermal broadening, which can be characterized by calculating the FWHM of the Fermi-Dirac distribution. **b)** The modulation voltage, which is used to directly measure dI/dV, introduces a small broadening denoted by the gray area. **c)** Lock-in time averaging from the low-pass filter introduces broadening by averaging measurements within τ.

The full width at half maximum of the Fermi-Dirac distribution gives a good measure of the thermal broadening in our system, as illustrated in figure 3.12. This comes out to $\Delta E \approx 3.5 k_B T = 1.35$ meV for measurements in our system, which usually occur at T = 4.5K, just above liquid helium temperature.

A second source of broadening comes from the modulation voltage applied on top of the bias voltage. This modulation voltage $V_M \cos(\omega t)$ averages dI/dV within $\pm V_M$ of the bias voltage. Minimizing V_M reduces the broadening caused by this, however this also causes a lower signal-to-noise ratio. In practice, the modulation voltage is regularly adjusted to have sufficient signal-to-noise while minimizing the effects of broadening. For our measurements, $V_M \approx 1-10$ meV (2 - 20 meV peak-to-peak) is used, making $\Delta E \approx 2 - 20$ meV based on the choice of modulation amplitude.

A third source of broadening comes from the time-averaging effect of the lock-in amplifier itself. The lock-in amplifier utilizes a low-pass filter to integrate the multiplied signal and reference waves, and the length of this time-averaging serves as an energy resolution of the measurement. The measurement at a time t actually averages every measurement from (t - τ) to t (weighted by an exponential), where $\tau = RC$ is the time constant of the low-pass filter. Thus the spectral broadening caused by this is $\Delta E \approx \tau \frac{E_{max} - E_{min}}{\Delta t_{spectrum}}$, where E_{max} and E_{min} are the maximum and minimum energy of the spectrum and $\Delta t_{spectrum}$ is the total time of the spectrum. For measurements in this thesis, $\Delta E \approx 7.5 - 50$ meV, however for measurements where higher energy resolution is required, longer spectra over a smaller energy range were used.

4 Magnetic Proximity Effect in a van der Waals Heterostructure

This chapter focuses on efforts to observe a magnetic proximity effect in an all-2D van der Waals heterostructure. As I discussed in 2.3, a magnetic proximity effect is where a non-magnetic material, like graphene, inherits the magnetic exchange from a nearby ferromagnetic material. This non-magnetic material would thus align its own electron spins in the absence of an external magnetic field.

The ability to induce ferromagnetism in a material via a proximity effect is an enticing idea from the perspective of designing topological effects in materials. The boundary between topologically distinct phases of matter often hosts interesting physical properties, such as the dissipationless edge states present at the boundary between topologically distinct insulating phases [59]. Often, a critical ingredient to observing these phenomena is a means to break time-reversal symmetry. Such is the case in the quantum anomalous Hall effect, where spin-polarized dissipationless edge states exist in the absence of an external magnetic field [60], or in the observation of Majorana zero modes at the boundary of 1D superconductors, which have applications in topological quantum computing [61]. This can be achieved via proximity to a ferromagnetic material, where the material system inherits the exchange effect of the neighboring ferromagnet, and the net magnetization of the resulting system breaks time-reversal symmetry.

To this end, van der Waals heterostructures offer an ideal stage on which to design topological phenomena. Critical ingredients to these phenomena such as exchange effects or spin-orbit coupling may be induced via proximity effects within a heterostructure, and combination of multiple such effects in a single 2D device is possible. One famous such proposal involving the quantum anomalous Hall effect in graphene requires the addition of both Rashba spin-orbit coupling and an exchange effect [62, 63], both of which could be induced via proximity effects. The intrinsically-high mobility of graphene is key here, as the spin-orbit coupling induces a gap that is only 5.5 meV wide, which means any electron scattering would broaden transport features such that this small gap is unobservable. Spin-orbit coupling has been induced in graphene heterostructures with WSe_2 in the past [34], however a magnetic proximity effect in graphene has yet to be observed in an all-2D-material device.

A couple research groups have observed magnetic proximity between graphene and *3D* magnetic materials. P. Wei *et. al* studied magnetic exchange between 3D ferromagnetic insulator EuS and graphene [64]. They measure nonlocal

resistance in this device, where the current and measurement probes are separated by a small distance of the order of microns, making any transport features a result of magnetic effects. They observe an enhancement of the nonlocal resistance at the CNP of graphene, which is attributed to a magnetic exchange field induced in graphene by EuS. Z. Wang *et. al* studied magnetic exchange between graphene and 3D ferrimagnetic Yttrium Iron Garnet and observed a classical anomalous Hall effect, indicating a net magnetic moment exists in graphene as a result of a proximity effect [65].

Both of these studies utilize a 3D magnetic material to induce ferromagnetism in graphene by proximity. However, the intrinsic roughness of these materials causes a large decrease in the electron mobility of graphene, which limits the ability to observe small gaps in the electronic structure, and thus they cannot observe any topological phenomena. Additionally, neither study showed a net magnetization of graphene in the absence of an external magnetic field, instead only observing enhancement of the external field applied. Both of these limitations leave much room for improvement. Proximity magnetization induced by an atomically-flat magnetic material could preserve the intrinsically high mobility of graphene, allowing the measurement of fine gaps in the electronic spectrum, while use of a harder ferromagnet could allow observation of this at zero applied magnetic field.

In this work, I create proximity devices using multiple different two-dimensional ferromagnetic insulators in order to observe signs of a magnetic proximity effect in graphene. To measure this, I primarily utilize low temperature magnetotransport. By creating devices to measure the longitudinal and transverse resistance of graphene and varying parameters such as carrier density and perpendicular electric field, we can observe many different effects such as the quantum Hall effect, the Zeeman spin Hall effect, and other phenomena related to magnetism in the system. In the following sections, I'll describe measurements of several different magnetic proximity devices: graphene/CrI_3 transport devices, graphene/$CrBr_3$ STM devices, graphene/$RuCl_3$ transport devices, and lastly graphene/$CrSiTe_3$ transport devices.

4.1 Graphene - CrI_3

First I will describe graphene/CrI_3 proximity devices. We performed a before/after measurement process, where we first create a bare graphene device, measure its magnetotransport properties to ensure it is high quality, and then transfer CrI_3 on top and re-measure the device. In this measurement scheme, we can directly observe the effects of adding the ferromagnetic insulator by comparing transport results of the final heterostructure to those from the exact

same device minus the magnetic material. Additionally, this method minimizes exposure of CrI_3 to water and oxygen that could degrade it, since all of the fabrication steps occur before CrI_3 has been added to the device. Thus we can minimize the chance of this highly sensitive material degrading before we have a chance to measure it.

4.1.1 Graphene on hBN, Pre-transfer

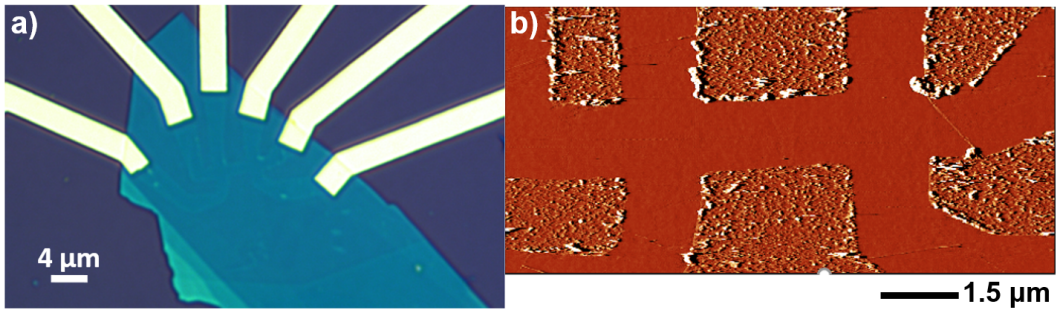

Figure 4.1: **a)** Graphene on hBN before transfer of the ferromagnetic material. **b)** AFM scan of this image showing cleanliness of the graphene channel.

The procedure for device fabrication goes as follows. First, graphene and hBN and exfoliated, and suitable flakes of both materials are optically identified. hBN that is 30-50 nm thick is selected in order to fully blanket the roughness of the underlying SiO_2 and provide a truly atomically-flat substrate for graphene. Then, using the dry transfer technique mentioned in section 3.2, the graphene flake is stacked on top of the hBN. The stack is characterized using atomic force microscopy, and the cleanest, flattest portion is identified. Reactive ion etching is used to create a Hall bar shape for the graphene, where the graphene is selectively etched on top of the hBN without etching the hBN flake. A recipe was developed specifically for this purpose utilizing the fact that oxygen plasma both chemically and physically etches graphene while only physically etching hBN, meaning the rate of etching can be finely tuned to maximize the chemical portion of the etch. Subsequently, Cr/Pd/Au leads are evaporated on top, where the introduction of Pd to the evaporation recipe serves to harden the resulting metallic bond pads and prevent accidental punch-through of the 300 nm SiO_2 layer and short the measurement leads to the global p-doped Si back-gate. The device is cleaned using both a vacuum anneal and AFM tip cleaning, which has been described in section 3.3.2. After wire-bonding, the device is then loaded into the cryostat for measurement, and

detailed magnetotransport measurements are performed. This helps us ensure that the graphene device is high quality, and gives us the ability to compare results both before and after transfer of CrI_3 onto the device channel.

We made several devices in the manner described above. Images of one such device before transfer of CrI_3 are shown in figure 4.1. From the AFM scan, it is immediately clear that while the nearby hBN is dirty, the graphene portion of the device is pristine, free from contaminants and particulates. The roughness on the hBN surface comes from either resists used during fabrication (found near the edges of the graphene), or from a natural roughness caused by the reactive ion etching process (in the middle of the hBN portions). The roughness of the surrounding hBN is of no consequence during this portion of the measurement.

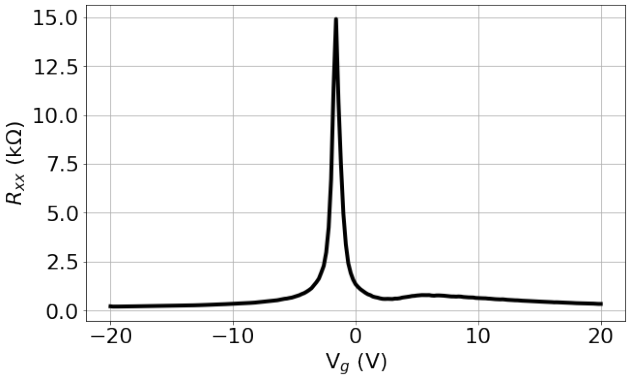

Figure 4.2: Sweep of longitudinal resistance vs gate voltage at zero field. The peak is associated with charge neutrality in graphene.

A gate voltage sweep of this device is shown in figure 4.2 at a temperature of 25 mK. A sharp resistance peak is seen around -2V, which is attributed to the charge neutrality point (CNP) in graphene. Its presence at relatively small gate voltage indicates negligible doping due to surface contaminants and is the first sign of a clean graphene device. While some devices have large shifts in the neutrality point due to potential fluctuations in the graphene from nearby charged contaminants, we found that the tip-cleaning procedure used on this device and similar devices causes nearly zero shift in the position of the neutrality peak.

Field-effect mobility for this device is calculated by linearly fitting the steepest portion of the CNP in the zero-field gate sweep. In this device, we measured $\mu \sim$ 110,000 cm^2/Vs, which is on par with some of the highest quality graphene devices reported in literature [20, 21, 23, 31, 56, 66].

This device also shows Landau level formation and quantum oscillations in as little as 0.1 T external magnetic field. Shubnikov-de Haas (SdH) oscillations are oscillations in the resistivity of a 2D electron gas as the magnetic field is increased. These oscillations are periodic in inverse magnetic field,

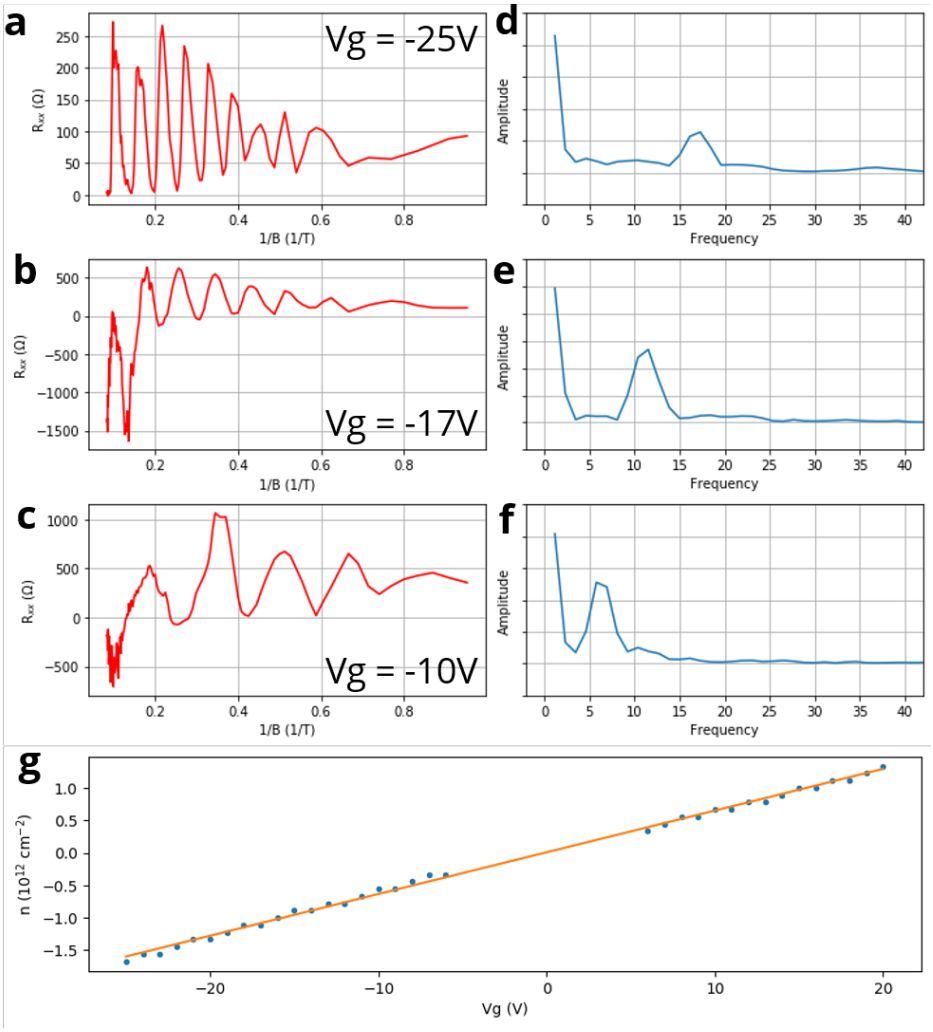

Figure 4.3: Shubnikov-de Haas oscillations in graphene. **a-c)** R_{xx} oscillations vs inverse magnetic field for various gate voltages. The fast Fourier transform of these is shown in figure **d-f)**, and the frequency of oscillation is seen to shift to the left. The density of electrons can be extracted from the frequency of oscillation, and is plotted with a linear fit vs. gate voltage in **g)**.

with frequency $f_{SdH} = \frac{nh}{4eB}$ for graphene. Thus they can be used to calculate the density of charge carriers in graphene [19]. Figure 4.3 shows this calculation. SdH oscillations are shown versus inverse magnetic field with the Fourier transform of the signal shown next to it. The frequency shifts lower as gate voltage decreases, and the corresponding density is plotted with a linear fit.

To further show the quality of the device, a full mapping of longitudinal and transverse device resistances in B and V_g parameter space is shown in figure 4.4. In some plots, conductivities are plotted as opposed to measured resistivity, where $\sigma_{xx(xy)} = \frac{\rho_{xx(xy)}}{\rho_{xx}^2+\rho_{xy}^2}$. The σ_{xx} plot shows peaks in conductivity with regions of zero conductivity in between. The σ_{xy} map shows plateaus of $\nu e^2/h$ for integer ν at the same positions where σ_{xy} is zero. This is the signature of the quantum Hall effect: transport is dominated by conducting

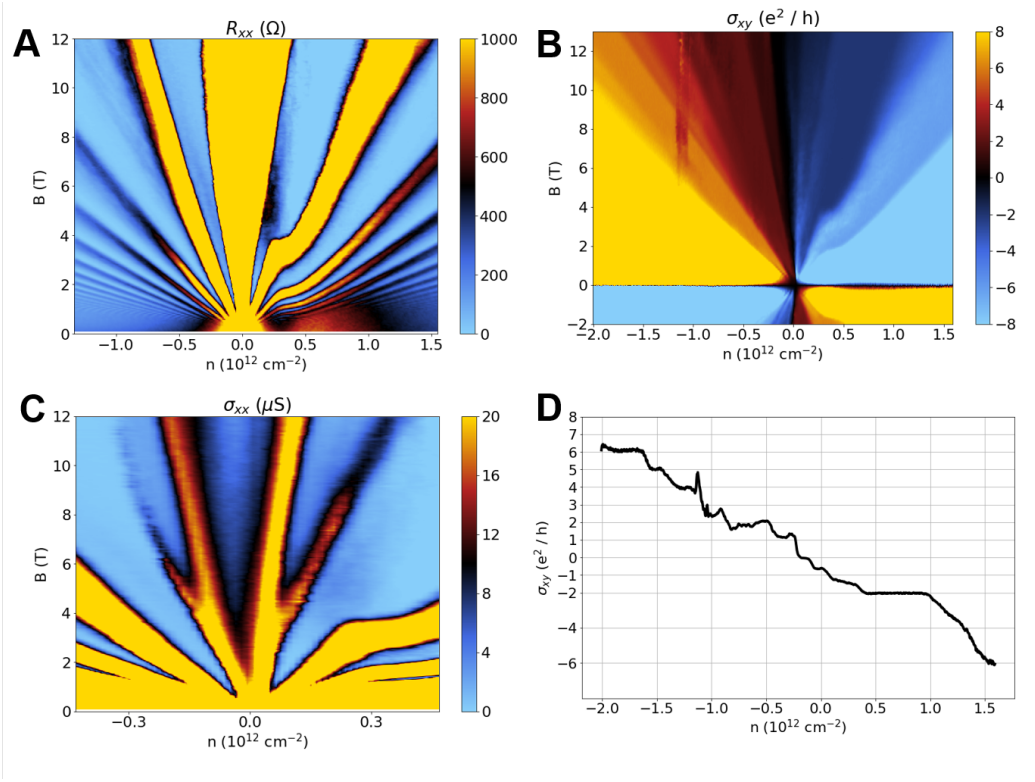

Figure 4.4: Quantum Hall effect in graphene on hBN with full symmetry breaking. **a)** The longitudinal resistance R_{xx} vs. gate voltage and magnetic field. A Landau fan is observed, indicating the formation of Landau levels. **b)** Hall conductivity σ_{xy} vs gate voltage and magnetic field. Plateaus of usual graphene sequence (ν = -6, -2, +2, +6) are seen at low magnetic fields. At high magnetic fields, intermediate integers are seen and labeled.**c)** Longitudinal conductivity σ_{xx} vs. gate voltage and magnetic field, centered on the zeroth Landau level. A full symmetry-breaking of the 4-fold spin and valley degeneracies in graphene is observed. **d)** Linecut of σ_{xy} at B = 12T. Plateaus of given integers are seen.

edge channels carrying ν conductance quanta surrounding an insulating bulk.

The expected graphene quantum Hall plateau sequence ($\nu = \pm 2, \pm 6$, ...) is seen at relatively low fields of 1-4T. At higher fields of 10+T, intermediate integer filling factors ν = -1, 0, +1, +3, +4, +5 are observed as well. Additionally, looking at the top of the σ_{xx} map, the zero Landau level is observed breaking apart into four separate Landau levels. This is due to breaking of spin and valley pseudospin degeneracy as magnetic field increases. In graphene, the lowest Landau level, called the zero Landau level due to its position at charge neutrality, is actually a combination of four degenerate Landau levels. This is because graphene exhibits a degeneracy in both spin and valley (i.e. K / K' in momentum space). Together, these act as a four-fold 'spin' basis. Via an analog to a Zeeman effect, these four degenerate levels are expected to split apart in energy at high magnetic fields as depicted in 4.5, distinguishing each spin ($\uparrow$ and $\downarrow$) and valley (K and K') separately. In this case, whenever the Fermi level lies between two of these now-resolved Landau levels, an intermediate-ν Hall plateau is expected. This is usually only visible in extremely clean devices, where mobility is large enough to fully resolve gaps between these Landau levels, indicating extremely high quality of the graphene device.

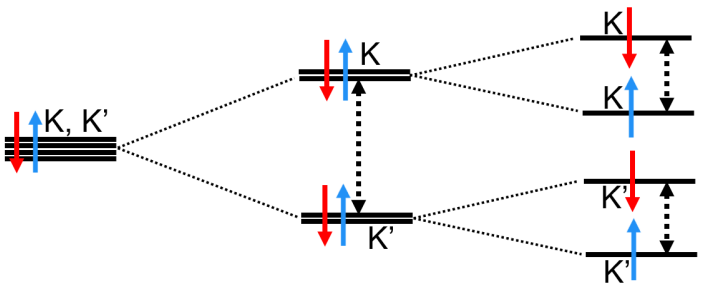

Figure 4.5: Splitting of the quadruply-degenerate zeroth Landau level in graphene as magnetic field is increased.

4.1.2 Post-CrI_3 Transfer

After measurement of the graphene-hBN pre-patterned heterostructure, the device is carefully removed from the cryostat and placed in the glovebox. Fresh CrI_3 is exfoliated, and a heterostructure of hBN-CrI_3 is placed on top of the existing graphene-hBN Hall bar. The CrI_3 flake is chosen so that it exactly fits overtop the Hall bar channel, and the flake is carefully aligned over top to ensure the best possible alignment. The outer two hBN layers seal in the CrI_3 as best as possible, attempting to protect it from degradation when brought

out of the glovebox.

The device is then brought into ambient conditions and quickly wire-bonded and loaded into the cryostat for more measurement. The device is in ambient conditions for no more than an hour, during which it is protected from light as much as possible. Together with the double-sided encapsulation, we hope that this adequately protects the material from degradation.

Figure 4.6 shows the device both before and after transfer of the hBN/CrI_3 heterostructure, along with a schematic detailing the final device structure. In the final image, the Hall bar is no longer visible due to the presence of the top layer of hBN and CrI_3 (outlined in black), however careful alignment of before and after images shows that the CrI_3 layer was successfully placed over top the device channel.

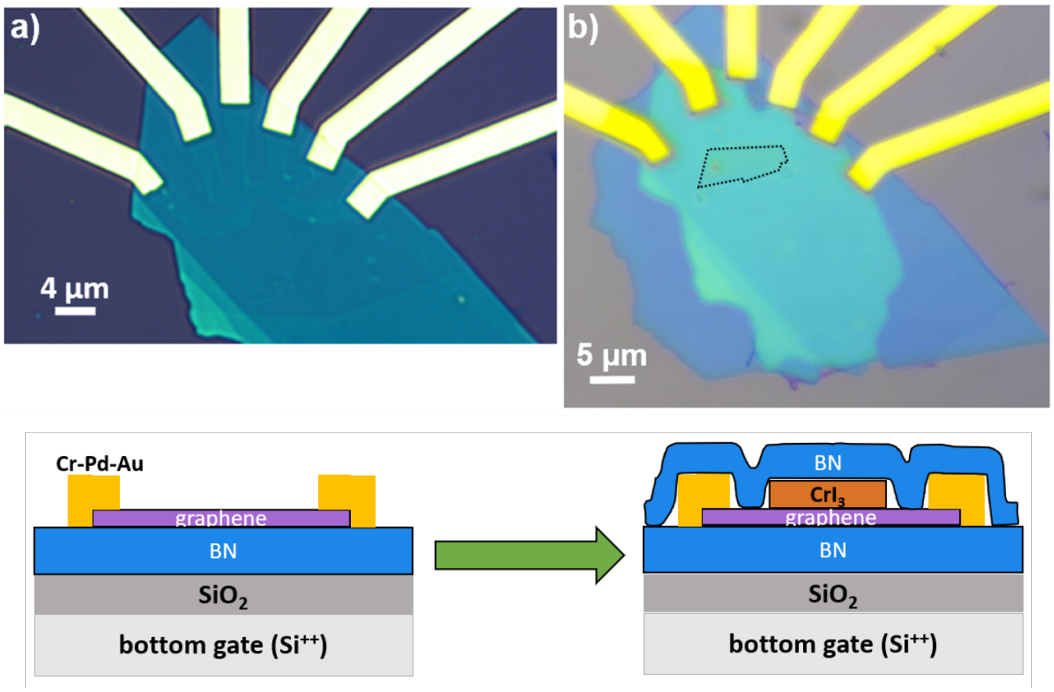

Figure 4.6: Graphene on hBN device **a)** before transfer of CrI_3 and **b)** after transfer of CrI_3. The final device has been encapsulated in hBN to protect the CrI_3 layer from degradation.

Longitudinal resistance of the device versus gate voltage is shown in figure 4.7 at zero field. A shallow positive slope is observed, but no resistance peak associated with charge neutrality in graphene is seen. In fact, the CNP is not observed even up to gate voltages of +60V, at which point the possibility of

dielectric breakdown of SiO_2 destroying the device becomes very high. This would correspond to a *minimum* hole doping of 4.5×10^{12} cm^{-2}. The zero-field slope suggests that the CNP is at a large positive inaccessible gate voltage, and that the device has been incredibly doped after the transfer of CrI_3. While the inability to find the CNP of graphene prevents accurate measurement of the field-effect mobility, using the measurement shown in 4.7 indicates $\mu \sim$ 1,000 cm^2/Vs, two orders of magnitude less than that of the bare graphene device.

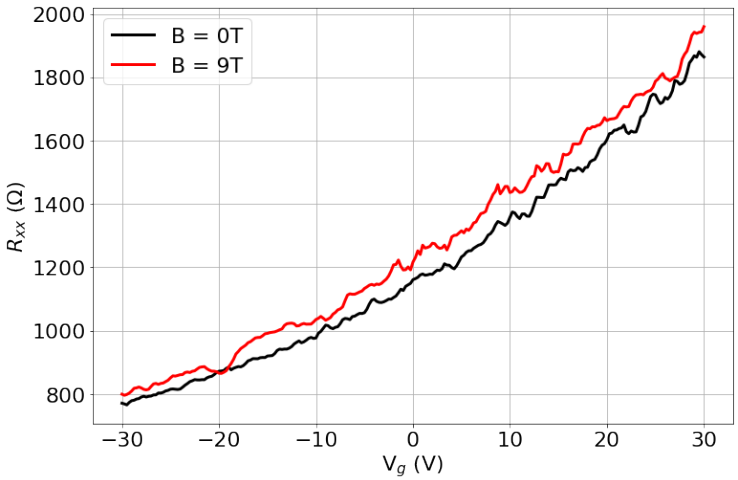

Figure 4.7: Longitudinal resistance sweeps at B = 0T and B = 9T. While the charge neutrality peak is not visible, the upward slope indicates that it may be at an inaccessible positive gate voltage.

A B = 9T gate sweep is also show in 4.7. This measurement shows similar behavior as the B = 0T measurement, and quantum oscillations are completely absent. We are unable to resolve the pseudospin-degenerate Landau levels ($\nu = \pm 2, \pm 6, \ldots$) even at 9T external field, indicating that device mobility has been drastically reduced after the transfer of CrI_3. A full map of the four-terminal resistance is shown in figure 4.8a. While a weak magneto-resistance is seen at all gate voltages, the map is featureless and devoid of any signature of quantum Hall physics, a complete departure from the behavior seen in the graphene-only structure.

We considered two possible causes of the electrostatic doping and reduced mobility. The first scenario is that contaminants from the surrounding hBN were pushed onto the graphene Hall bar. If these contaminants are charged in any way, they would electrostatically dope the graphene and explain the observed shift in the CNP. Additionally, their presence would cause deforma-

tion of the graphene, which would reduce the mobility similar to how graphene has a reduced mobility on rough substrates like SiO_2. Since the contaminants were near the very edges of the Hall bar (as shown in figure 4.9), it is reasonable that small lateral shifts in the CrI_3 could cause these contaminants to be pushed onto the surface of the graphene.

The second scenario is that CrI_3 degraded despite our attempts to protect it. CrI_3 absorbs water to form an aqueous solution of a complex chromium ion $Cr(H_2O)_6{}^{3+}$ and I^- ions, which form an electric double layer with the I^- ions closest to the graphene. This would electrostatically p-dope the graphene, exactly as we observe. Additionally, the presence of this degraded compound pinned closely to graphene would cause similar ripples in the graphene as the first scenario and similarly reduce the mobility. This behavior is reported in bilayer graphene/CrI_3 devices measured previously [54].

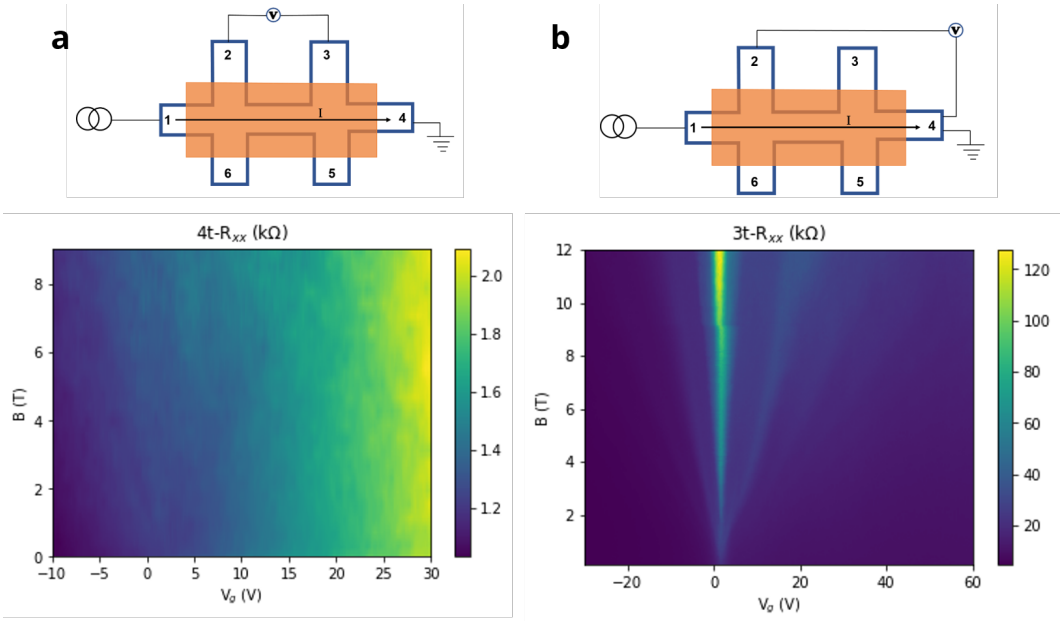

Figure 4.8: **a)** Four and **b)** three terminal resistance maps. In the three terminal map, a graphene contact is included in the measurement, and this contact is not in proximity with CrI_3. The graphene features are recovered, indicating degradation of the CrI_3 and reduce quality of graphene have occurred.

In order to test these two scenarios, we performed two-terminal and three-terminal transport measurements of the graphene-CrI_3 device. This measurement includes the resistance of a measurement lead in series with the device channel. For example, in a four-terminal measurement between leads 2 and 3

in figure 4.8, the measurement leads are outside of the current channel, so a voltage measurement in this scheme will return a value proportional only to the channel resistance $V_{23} = IR_{channel}$, independent of the resistance of the two measurement leads. However in a three-terminal measurement between leads 2 and 4 in figure 4.8, one of the measurement leads is in the current channel, so a voltage measurement will return a value proportional to both the channel resistance and the lead resistance $V_{24} = I(R_{channel} + R_4)$. This lead resistance R_4 contains both the contact resistance from metal evaporated onto graphene, and resistance from the graphene portion of the lead between the metal contact and the device channel. In our device, the CrI_3 covers all of the device channel, however the measurement leads are partially uncovered by CrI_3. The graphene in the measurement leads should be unaffected by any doping and impurity scattering that may be induced by the degradation of CrI_3 if the second scenario is accurate. Any contaminants that may have been pushed onto the device channel would also have been pushed onto the measurement leads, so we would expect similar doping and mobility reduction if the first scenario is accurate.

Interestingly, we recover typical graphene behavior when performing two-terminal or three-terminal measurements. A map of three-terminal resistance over magnetic field and gate voltage is shown in figure 4.8b. A resistance peak near 0V is seen in the B=0T sweep, and a fan of resistance peaks separate in gate voltage as magnetic field is increased, indicative of the formation of Landau levels. This resembles the usual graphene behavior seen in previous measurements of the device. The recovery of pre-transfer behavior in this region indicates that the graphene here is of similar quality as before the transfer of CrI_3. This supports the hypothesis that CrI_3 degradation is the cause of the reduced device quality.

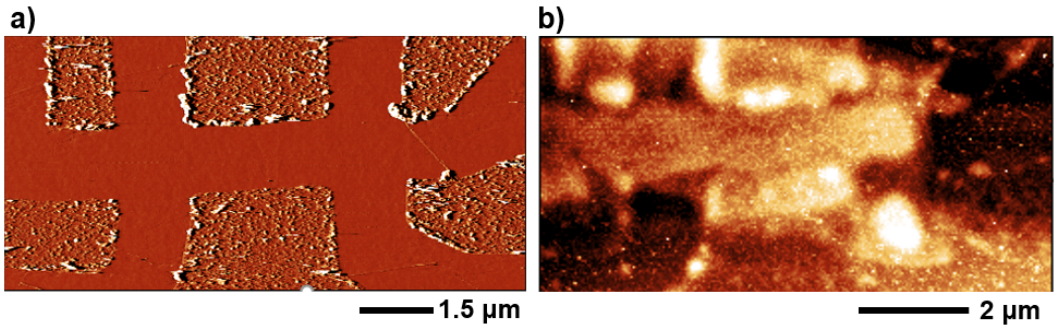

Figure 4.9: AFM scans of the device **a)** before and **b)** after transfer of CrI_3.

AFM scans of the device after removal from the cryostat are shown in fig-

ure 4.9. While a thick hBN flake on top prevents direct measurement of the topography of the interface, it is still fairly clear that there is roughness that shouldn't be present in an atomically-flat device. Additionally, the contaminants that were observed at the edges of the graphene Hall bar remain in their original locations, indicating that transfer of the CrI_3 did not move them onto the surface of the device. We therefore conclude that CrI_3 degradation is the root cause of the reduced device quality.

I'll quickly discuss another possible mechanism behind the strong p-doping present in this system, as well as an argument for why it cannot be responsible for features seen in this measurement. Heterostructures of 2D crystals with large differences in work functions will induce a transfer of charge between the two so that the Fermi levels of the two materials align. This type of modulation doping can have several consequences, including the opening of conduction channels in typically-insulating materials (which I'll discuss in detail in section 4.3) or the shift of graphene features such that they exist far away from the Fermi level. The work functions of graphene (4.6 eV [67]) and CrI_3 (5.3 eV [68]) indicate charge should transfer from the graphene layer into the CrI_3, causing a uniform p-doping of the graphene layers. However, in this situation the high mobility of graphene should be retained. Instead, we observe a large reduction in mobility of the graphene/CrI_3 heterostructure compared to the bare graphene device. With pure charge transfer, quantum oscillations should still be present in the heterostructure, however they are absent post-transfer of CrI_3. This indicates that charge transfer is likely not responsible for the strong p-doping, and instead CrI_3 degradation is the culprit.

Although we cannot state with confidence the cause of this degradation, we predict that it occurred due to the tenting of hBN around the thick Au electrical leads. When hBN is placed on a rough surface, it cannot conform to the exact topography of the surface. Where sudden changes in height occur, the hBN will have a "tenting" effect, where the hBN layer drapes over the rough underlying surface like a blanket. This has the effect of smoothing out the rough surface, which is why hBN serves are a good substrate for graphene, smoothing out the rough underlying SiO_2. However, it has the unintended consequence of opening up small channels where large changes in topography occur, for example near the Au leads. These channels allow air and water to seep underneath the hBN. We hypothesize that these channels are the unintended pathways for water from the atmosphere to reach the CrI_3 and cause degradation.

Due to the prominence of CrI_3 in the condensed matter community as a promising 2D magnetic proximity material, we since learned of additional attempts at Columbia University to observe magnetic proximity to graphene

that similarly failed. In these attempts they used via contacts in hBN to contact graphene. Via contacts are made by etching holes into an hBN top layer and evaporating Au contacts in these holes. The entire flake, hBN and Au, is then picked up using the dry transfer technique, and the exposed gold on the bottom can be used to electrically contact other 2D materials. In this work, researchers created a heterostructure of via-hBN/graphene/CrI_3/hBN and measured this with electron transport. They observed similar degradation of the CrI_3, indicating that small gaps between the evaporated Au and hBN were enough to allow atmospheric water to reach the CrI_3 and cause degradation.

Due to the incredible sensitivity of CrI_3, we decided not to pursue future transport devices using this material.

4.1.3 Nonlocal Transport and Temperature Cycles

Although local transport measurements showed CrI_3 measurements were detrimental to device quality, I'll still discuss other avenues pursued to measure long-range magnetic order in graphene-CrI_3 heterostructures.

Nonlocal Transport

Nonlocal transport measurements were performed on this device both before and after transfer of CrI_3. Briefly, a nonlocal measurement is where the source current and measurement leads are physically separated from one another by a small distance, usually on the order of microns. In the absence of magnetic effects, zero voltage difference between the measurement leads is expected, however a nonzero voltage difference is expected when either a magnetic field is applied or the sample has net magnetization in the absence of an external field. Figure 4.10a shows graphene nonlocal transport before transfer, where the x-axis shows Landau level filling factor ν. A large $\nu = 0$ peak is present that dwarfs any other features, and two small peaks at $\nu = \pm 4$ are also present. This behavior resembles previous graphene nonlocal transport performed by Abanin et al. [66].

After transfer of the CrI_3, the signal has much weaker, nonsensical features. Since the device is extremely doped, we would not expect to see the $\nu = 0$ peak associated with the Zeeman spin Hall effect at the CNP. Since the device mobility is extremely low and prevents the observation of Landau levels, we would also not expect to see any $\nu \neq 0$ peaks since they are associated with edge transport in the quantum Hall regime. Thus this noisy, meaningless signal is expected.

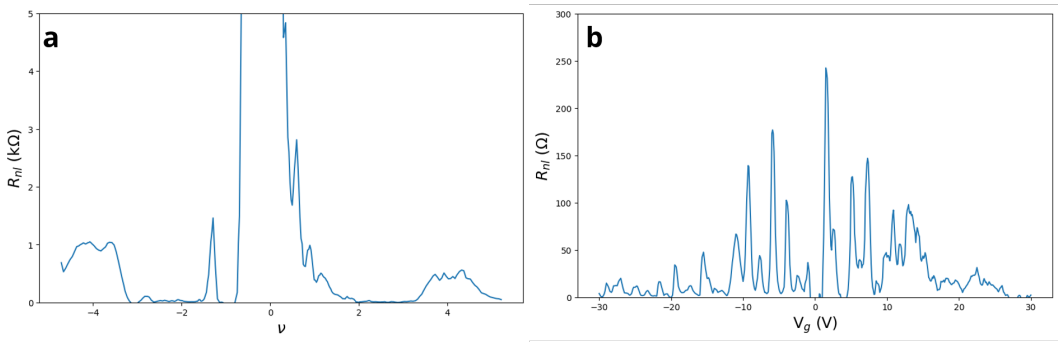

Figure 4.10: Nonlocal transport in the device **a)** before and **b)** after transfer of CrI_3.

Divergence of Repeated Zero-Field Cooldowns

We additionally observed differences in four-terminal resistance measurements as the device was cooled at zero field. A CrI_3-graphene device was cooled to 2K in the absence of a magnetic field, followed by an immediate warming back to room temperature. This process was repeated multiple times while recording the transverse resistance R_{xy}, and is shown in figure 4.11. High temperature behavior is identical for each cool/warm. However around 80K these traces start to separate, settling on a different value of R_{xy} after each subsequent warm/cool. The temperature at which this behavior begins is conspicuously close to the Curie temperature of bulk CrI_3, 61K.

When a ferromagnet is cooled below the Curie temperature, magnetic domains in the material randomly choose a spin orientation. In the limit of large number of magnetic domains, this implies the net magnetization will be zero almost every time a ferromagnet is cooled since there are nearly equal numbers of oppositely polarized magnetic domains. However, with a small number of magnetic domains, the system performs less coin-flips, and there is a high likelihood of a net magnetization present before an external magnetic field is applied. This magnetization could give rise to an anomalous Hall effect, which would cause different values of R_{xy} for subsequent cooldowns. Since the magnetic structure doesn't change until the ferromagnet is heated above the Curie temperature, the R_{xy} traces would lay exactly on top of one another.

However, the lack of a magnetic hysteresis destroys this hypothesis. If this is correct, we would expect to see a magnetic hysteresis and an anomalous Hall effect as magnetic field is swept, which is not observed. To additionally refute this hypothesis, field cool/warms at B=1T were performed and are shown in figure 4.12. This is well above the coercive field of 50mT of CrI_3, so R_{xy}

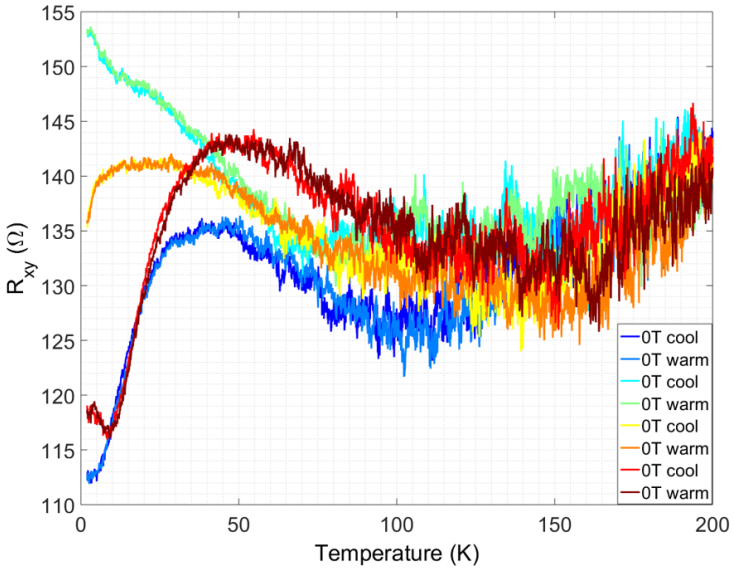

Figure 4.11: Zero-field cools / warms of a graphene/CrI_3 device. R_{xy} diverges to different values, which may be a sign of different configurations of magnetic domains in the material.

traces should lie on top of one another for all warm/cools. Instead, we observe difference in the R_{xy} upon repeated cools/warms. This indicates that magnetic structure is not the cause of this phenomenon.

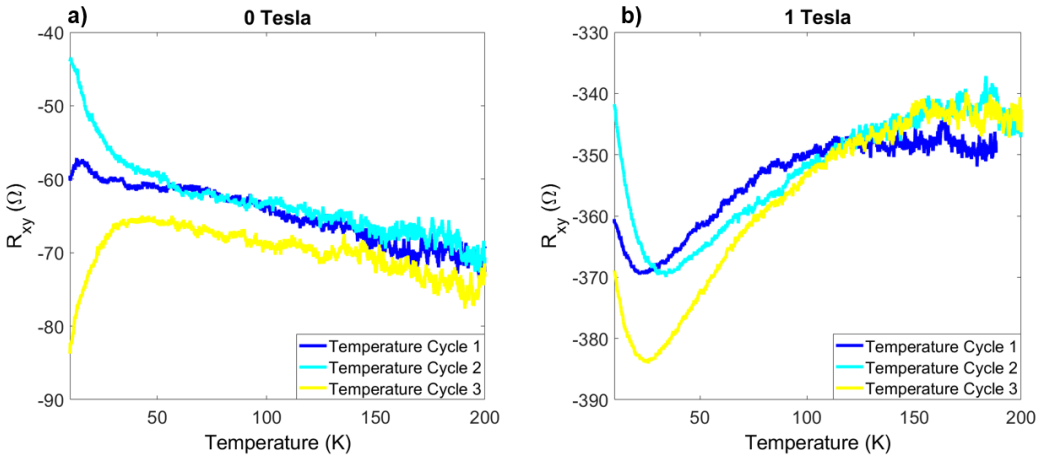

Figure 4.12: **a)** Zero field temperature cycles and **b)** 1T temperature cycles of a graphene/CrI_3 device. They show remarkably different behavior.

We instead attribute this divergence upon cooling to rearrangement of non-magnetic impurity sites due to disorder. At higher temperature we expect these sites to be mobile, and freeze in place as temperature is lowered. When the temperature is again raised, these sites can rearrange, giving rise to the much noisier signal seen at higher temperatures. As the temperature is again lowered, these scattering sites would freeze in place at a different R_{xy} value.

4.2 Graphene-$CrBr_3$ in STM

Results from the transport studies detailed above made clear that ferromagnet degradation was inhibiting measurement of a magnetic proximity effect in graphene. In order to combat this, I made two major changes to the measurement scheme. First, I decided to measure the samples using scanning tunneling microscopy (STM). As I mentioned in 3.4, STM measurement occurs entirely in ultra-high vacuum, and sample preparation techniques developed in this lab can be used to ensure the sample doesn't need to enter ambient room conditions before being loaded into the STM. This is in contrast to the aforementioned transport experiments, where samples must be brought into ambient conditions for wire-bonding and loading into the cryostat. Additionally, the degree of material degradation likely varies across the material surface, meaning there can be regions of the sample that are locally less degraded than others. Transport measurements would measure both degraded and non-degraded portions of the device in series, while an STM measurement can focus on only the non-degraded portions of the sample. Second, I decided to use $CrBr_3$ in place of CrI_3. As mentioned in 2.1.6, $CrBr_3$ is another ferromagnetic material similar in structure to CrI_3, however it is more stable and degrades at a much slower rate than CrI_3. Thus it is more likely to survive until measurement than CrI_3. For these two reasons, I decided to make heterostructures of graphene/$CrBr_3$ for measurement in the STM.

Despite these attempts to protect these delicate ferromagnets, many heterostructures still exhibited ferromagnet degradation. Figure 4.13 shows a before/after comparison of a couple such devices, with the top two images showing a device made using CrI_3 and the bottom two images showing a device made using $CrBr_3$. In the before image, the ferromagnet is outlined in a white dashed line to increase visibility. In both cases, nearly complete degradation of the ferromagnet has occurred, and only small portions of the initial flake remain. This level of destruction makes measurement with the STM meaningless. After carefully considering all possible sources of failure, I assumed that the small O_2 and H_2O levels present in the glovebox (which are currently 1.8 ppm and 5.2 ppm respectively at the time of writing this thesis)

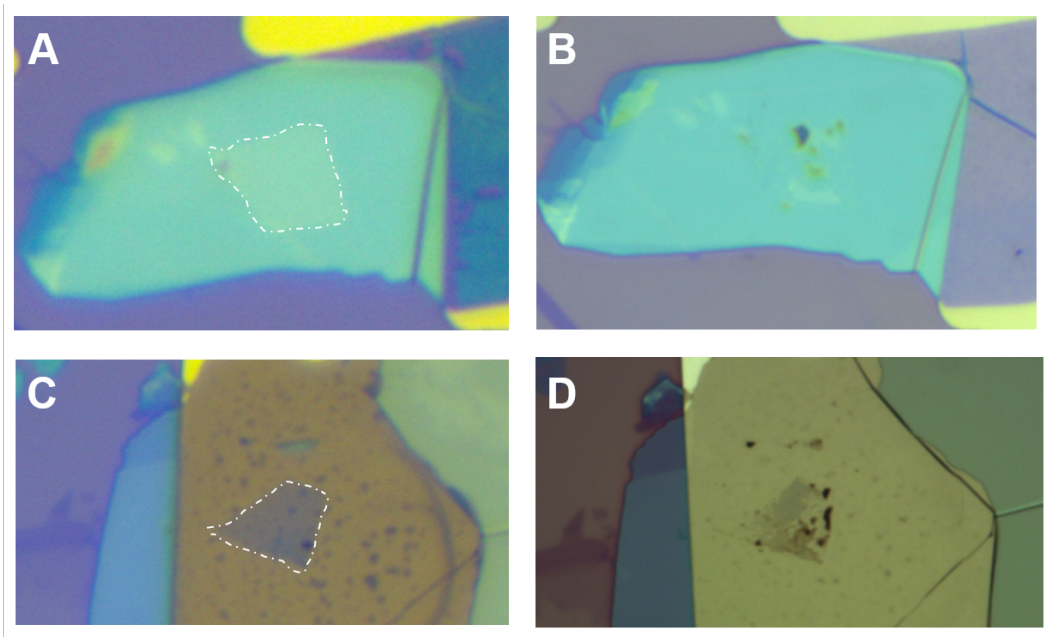

Figure 4.13: Degradation of two different graphene-chromium halide heterostructure. **a)** and **c)** show before an anneal, while **b)** and **d)** show after an anneal. Near total degradation of the ferromagnet is observed in both cases.

were enough to cause degradation of these materials. This is the only part of the fabrication process that introduces the materials to even small amounts of these harmful contaminants. Because of this, I decided to use a device geometry that fully encapsulated the ferromagnet in a sheet of graphene. This technique minimizes the amount of time that the ferromagnet is exposed to the small O_2 and H_2O levels, increasing the chance of creating a successful device. This technique allowed me to create two devices that survived the fabrication process and were loaded into the STM.

Figure 4.14 shows a completed device, as well as the device structure used in these measurements. In addition to the graphene and $CrBr_3$, a WSe_2 substrate is used. The WSe_2 acts as an atomically flat stage for graphene, and blankets out ripples from both the Au/Pd/Cr tunnel contact and the SiO_2 substrate. It is used in place of hBN due to its semiconducting nature, making it possible to tunnel on exposed portions of the WSe_2 flake by using a large bias voltage. Exposed hBN in this situation would ruin measurement, as the feedback mechanism would be unable to establish a tunneling current and would push the tip deep into the hBN layer.

Figure 4.15 shows one complete STM proximity device. A topographic

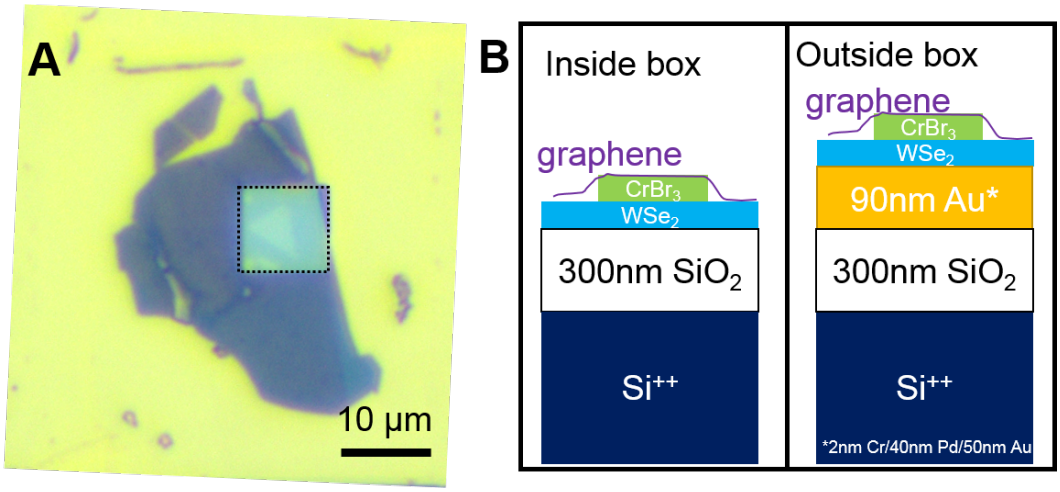

Figure 4.14: **a)** Optical image of one graphene-$CrBr_3$ heterostructure. $CrBr_3$ is visible within the black dashed line (small triangle). Graphene is not visible. **b)** Side-view of the device structure. Within the box, the Au tunnel drain is not present.

map of the device in STM shows many large bubbles in the heterostructure. Small-area scans over these bubbles show a hexagonal atomic lattice with the spacing of graphene, indicating these bubbles contain materials trapped at the graphene/$CrBr_3$ interface. This indicates that degradation of the $CrBr_3$ likely still occurred in spite of efforts to prevent it. Figure 4.15b shows an STS spectrum from this device, taken between the large bubbles on the surface. The minimum in this spectrum shows the location of the CNP in graphene, and is located at a moderate positive sample bias. This means the graphene layer is p-doped, which is consistent with results of degraded CrI_3 from transport. This behavior was observed in both graphene/$CrBr_3$ devices measured.

In total, ten graphene/chromium halide heterostructures were fabricated for this experiment. Eight of them exhibited visible degradation that prevented their measurement with the STM. The remaining two showed a strong p-doping of the graphene layer, indicating degradation of the $CrBr_3$ layer had likely still occurred. Because of this incredible sensitivity of this system, I decided not to pursue future STM devices using these materials.

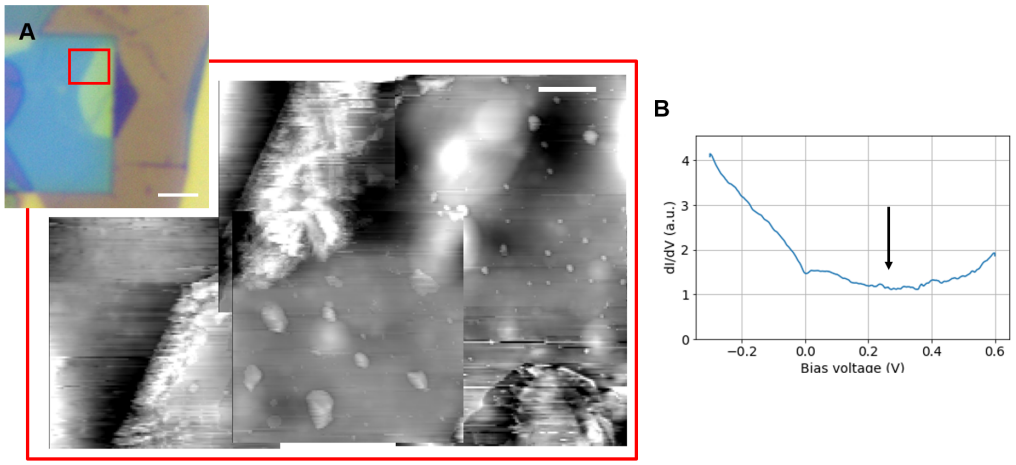

Figure 4.15: **a)** Several topographical maps taken in the STM stitched together. They make up the area in the red square of the inset. Scale bar is 2.5 μm in the inset, and 200 nm in the map. **b)** STS spectrum on the cleanest portion of a). A minimum associated with the CNP in graphene is observed.

4.3 Graphene - α-$RuCl_3$ Results

Around this time, a new paper indicating a possible ferromagnetic transition in graphene/$RuCl_3$ heterostructures was published. Zhou et al. [69] fabricated $RuCl_3$/graphene heterostructures by first fabricating graphene Hall bars, cleaning using contact-mode atomic force microscopy, and then transferring $RuCl_3$ on top before measurement. They measure an increased conductivity compared to compared to that expected from bare graphene, and attribute this to parallel conduction through nearby $RuCl_3$ layers. $RuCl_3$ is usually a Mott insulator, but charge transfer from the nearby graphene could cause the Fermi level to shift out of the Mott gap and cause conduction in the $RuCl_3$.

They also measure R vs. T in their heterostructures, and notice a peak-dip feature in the temperature range 12-35 K that can be tuned by gate voltage. They attribute this feature to a ferromagnetic transition at some gate voltages and an anti-ferromagnetic transitions at others, based on early work characterizing critical behavior or metals and semiconductors [70–72]. The presence of a ferromagnetic transition at some densities and an anti-ferromagnetic at others has been predicted in Mott insulators in the past [73], but a gate-tunable magnetic transition in a 2D material like this has never been observed. Either of these would be interesting, since they imply the onset of magnetic order in graphene, and imply a magnetic proximity effect could exist between these materials, hence motivating our interest.

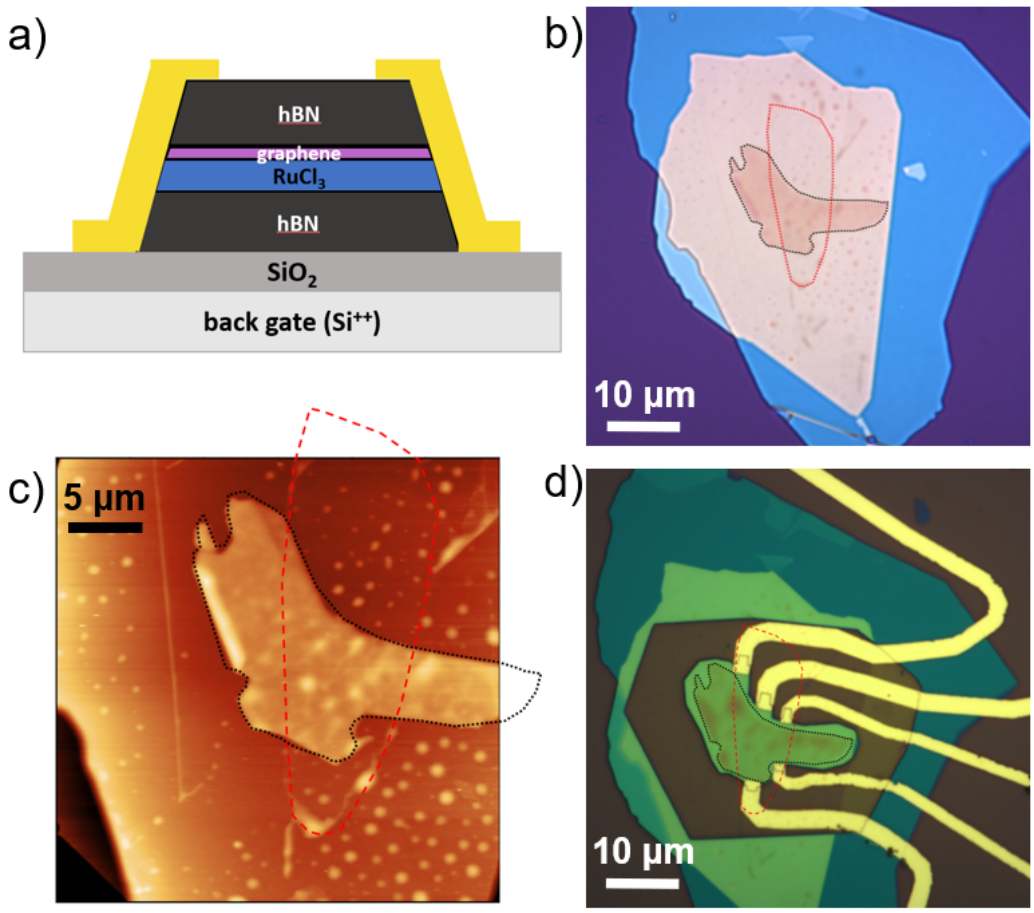

Figure 4.16: $RuCl_3$ device fabrication. **a)** Planned device structure with encapsulation and edge contact. **b)** Finished stack, with graphene and $RuCl_3$ outlined in red and black respectively. **c)** AFM of the device with graphene and $RuCl_3$ outlined. **d)** Finished device with etching and electrical leads.

In order to further investigate this magnetic proximity effect, heterostructures consisting of hBN/graphene/α-$RuCl_3$/hBN were fabricated. A schematic of the device plan is shown in figure 4.16a. Since $RuCl_3$ degrades at high temperatures, PPC was used as the transfer polymer during stacking. Set down using this material occurs as 90°C instead of 180°C, significantly reducing the chance of degradation of $RuCl_3$. PPC was spin-coated onto a SiO_2/Si chip, and hBN was exfoliated on top of the PPC. A transfer slide is made using this PPC film in the same manner as previously described, being sure to center the chosen hBN flake at the apex of the PDMS droplet. Then, this transfer slide

was used to pick up graphene, $RuCl_3$, and finally set down on another layer of hBN.

Optical and AFM pictures of this stack are shown in figure 4.16. We etched the surrounding hBN and graphene so that the $RuCl_3$ is entirely encapsulated by hBN and the graphene edge is exposed. This device was then contacted using the edge-contact method described in section 3.3.2. Due to the small size of the graphene layer, we were only able to make five contacts, and thus limited the measurements so that we were unable to make pure-R_{xx} or pure-R_{xy} measurements. However, fruitful physics was still observed using this preliminary device.

A four-terminal resistance measurement performed over temperature and gate voltage parameter space is shown in figure 4.17 along with some linecuts at various temperatures. From these measurements, typical graphene quality is immediately apparent, with the CNP visible at only slightly positive voltages. This indicates minimal electrostatic doping. Interestingly, instead of the typically kΩ-range peak height of the charge-neutrality point, the overall resistance is an order of magnitude smaller, reaching around 300 Ω at its max. This is consistent with reports from previous graphene/$RuCl_3$ devices [69, 74].

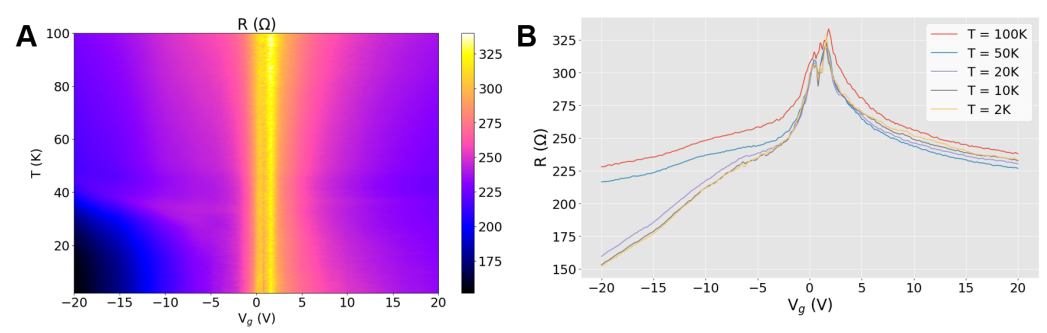

Figure 4.17: **a)** Four-terminal resistance vs. temperature and gate voltage.**b)** Line cuts at various temperatures are shown.

This can be explained by the large work function difference between graphene and $RuCl_3$. Graphene has a work function of 4.6 eV [75] while $RuCl_3$ has a much larger work function of 6.1 eV [76]. This means when the materials come into contact, charge will transfer from the graphene into the $RuCl_3$ in order to align their Fermi levels. This charge transfer moves the top few layers of $RuCl_3$ out of the Mott gap, opening up a conducting channel in $RuCl_3$ itself. This parallel conduction channel is responsible for the enhanced conductivity observed.

This explanation implies the CNP of graphene should be shifted to positive gate voltages, due to the p-doping induced by the charge transfer. However, we observe the charge neutrality point remain at nearly zero gate voltage, which seems to contradict this theory. However, this can be explained by the roughness of the graphene/$RuCl_3$ interface. Careful observation of the device shown in figure 4.16 shows several small bubbles exist between the graphene and $RuCl_3$. These contaminants physically separate graphene from $RuCl_3$, preventing charge transfer from occurring. In these regions, we expect the CNP in graphene to remain close to zero. Our transport results measure both these portions and the portions with graphene and $RuCl_3$ in good contact, so we expect to see both features simultaneously.

4.3.1 Magnetic Transition

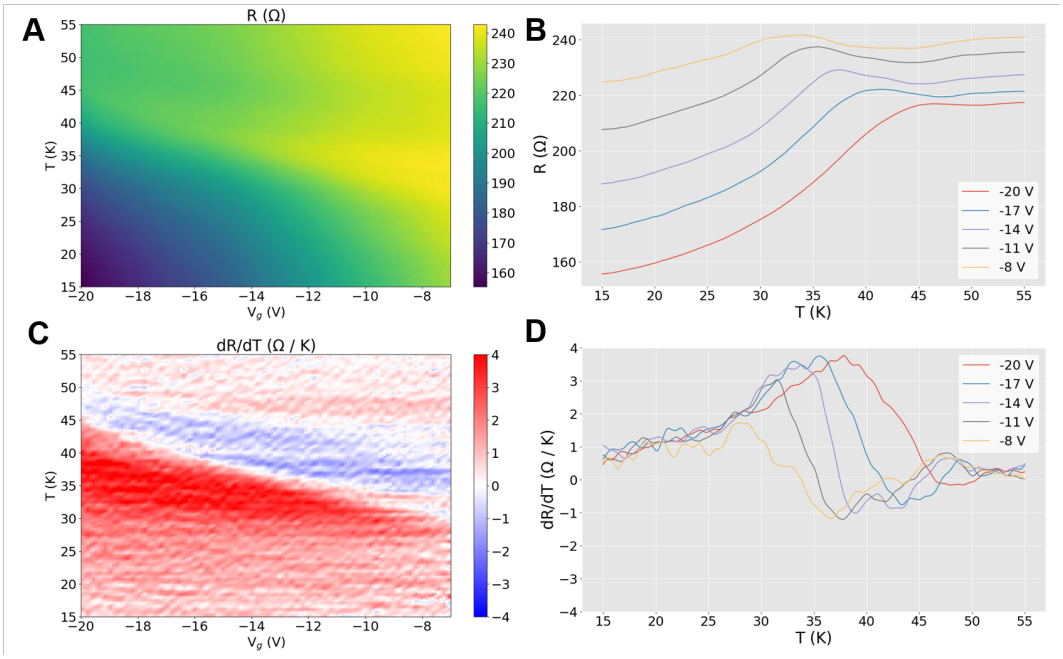

Figure 4.18: Transport in graphene-$RuCl_3$ at zero magnetic field. **a)** Four terminal resistance T-Vg map, zooming in on the feature at negative gate voltages.**b)** Linecuts of the previous T-Vg map. **c)** dR/dT map in the same region of T-Vg as before. **d)** Linecuts of the previous dR/dT map

In addition to the enhanced conductivity, we also observe an interesting feature in the four-terminal resistance at elevated temperature and negative

gate voltages of this device. Figure 4.17 shows the four-terminal resistance as temperature and gate voltage V_g are varied, and a sudden decrease in resistance is seen for large negative gate voltages, indicated by the big black spot on the colormap in the bottom left. Figure 4.18a zooms in on this region, showing the four-terminal resistance over a smaller gate and temperature range. Linecuts at constant gate voltages reveal a small hump in resistance and a large decrease as temperature is decreased. Figure 4.18c shows a colormap of dR/dT, where a peak-dip feature is observed. Linecuts of this feature at several gate voltages are presented in figure 4.18d.

This hump may be attributed to a magnetic phase transition in the heterostructure. Early work on critical behavior of semiconductors [70–72] revealed that an anti-ferromagnetic transition is accompanied by a peak-dip feature in the dR/dT signal. In figure 4.18d, we see this peak-dip feature at several different gate voltages. Assigning the minimum of the dip in this peak-dip feature as the Néel temperature of the antiferromagnetic transition, we see a range of Néel temperatures from 35-50K for different gate voltages. This suggests an antiferromagnetic transition in either the graphene layer or a parallel conducting channel in the $RuCl_3$, and that this transition is electrically tunable. In contrast to the work of Zhou *et al.*, we do not observe signs of a ferromagnetic transition at any gate voltage. Additionally, the temperature of the anti-ferromagnetic transition is higher than that observed in Zhou *et al.*, where they observe a magnetic transition around T = 20K. Both of these observations are higher than the Néel temperature of bare $RuCl_3$ (7 - 14K depending on stacking).

In order to corroborate the lack of a ferromagnetic transition, we collaborated with Xiaodong Xu's group at the University of Washington to perform RMCD measurements, shown in figure 4.19. RMCD, is an optical technique similar to MOKE (described in section 2.1.6), but circularly-polarized light is used in place of linearly polarized light. The total reflected light is recorded, and the intensity of the reflected light is sensitive to the net magnetization in the sample. We should thus see a large RMCD signal for a ferromagnetic system, and a nearly-zero signal for an anti-ferromagnetic or very weakly paramagnetic system. Figure 4.19a and b show RMCD measurements on the graphene/$RuCl_3$ structure and a graphene-only portion of the same device. The RMCD signal is nearly zero for each of these locations, which is evidence that there is not a ferromagnetic state in this system.

We additionally measure this magnetic transition as a function of out-of-plane magnetic field. Figure 4.20 shows transport measurements at 1T external magnetic field. We observe similar phenomena as in the 0T case. This is expected, as $RuCl_3$'s robust in-plane antiferromagnetism has been observed

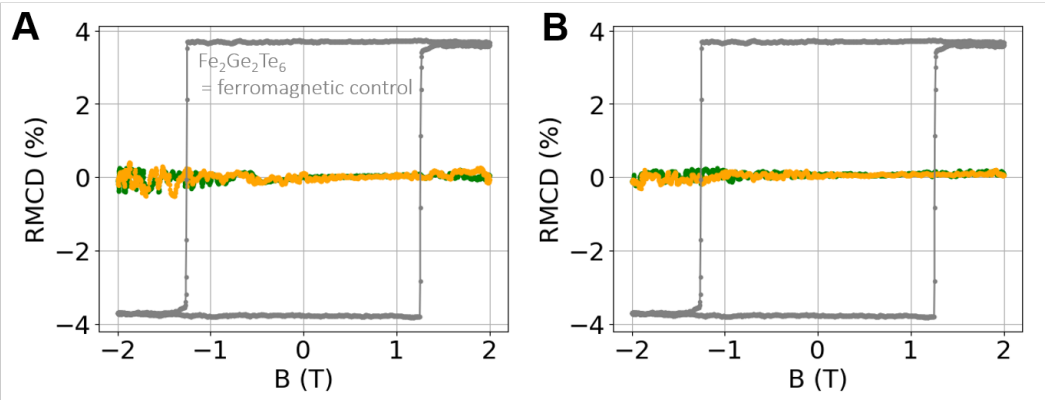

Figure 4.19: RMCD measurements of a graphene-$RuCl_3$ heterostructure. **a)** RMCD on the graphene-$RuCl_3$ region. **b)** RMCD on a graphene-only region. All measurements shown here were performed by Zaiyao Fei from Xiaodong Xu's group at the University of Washington

even at 9T perpendicular fields [77]. The largest magnetic fields we can apply in this system are 9T, and at this field quantum Hall features vastly dwarf the small magnetic transition feature seen here. Because of this, rigorous study of the magnetic transition with perpendicular field are impossible.

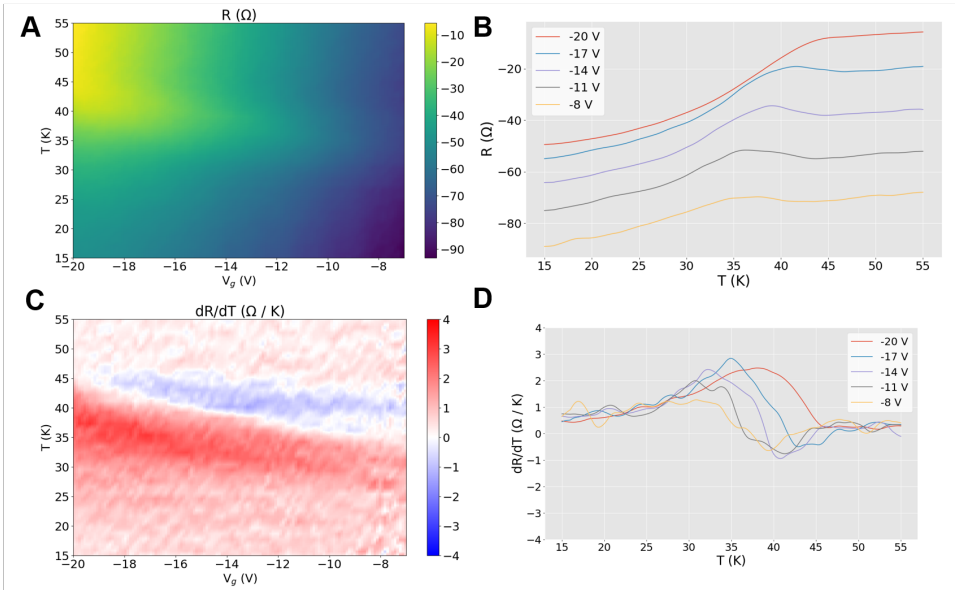

Figure 4.20: Transport in graphene-$RuCl_3$ at B=1T external magnetic field. **a)** Four terminal resistance T-Vg map, zooming in on the feature at negative gate voltages. **b)** Linecuts of the previous T-Vg map. **c)** dR/dT map in the same region of T-Vg as before. **d)** Linecuts of the previous dR/dT map

4.4 Graphene - CST Results

In this section, I'll briefly discuss experiments using $CrSiTe_3$ (CST) as the ferromagnetic insulator to induce proximity magnetization in graphene. These experiments were performed before either of the aforementioned experiments, taking place during the first year of my PhD.

Previously in section 4.1.3, I described how nonlocal transport can be used as a probe of magnetic interactions in graphene. Abanin *et al.* measured the nonlocal resistance peak in graphene as a function of external magnetic field, and found that the height of this peak is proportional to the square of the Zeeman splitting, $R_{nl} \propto E_Z^2$ [66, 78]. In a graphene-only device, this Zeeman splitting is proportional to the external magnetic field alone, $E_Z = \mu_B B_{ext}$. However, in the presence of a ferromagnetic material proximitizing the graphene, the effective magnetic field would be enhanced by the magnetic exchange field, and the Zeeman splitting that results from this would depend on both the external field and magnetic exchange field, $E_Z = \mu_B(B_{ext}+B_{MEF})$.

In the following section, I'll describe attempts to use nonlocal resistance measurements in graphene/CST devices to measure the magnetic exchange

field in graphene. These devices all follow the same pattern of fabrication and measurement. First, a graphene Hall bar is fabricated on an SiO_2 substrate. This device is then characterized using low temperature magnetotransport measurements, where device quality is assessed by measuring the mobility of the device and looking for quantum Hall features. We also perform nonlocal transport measurements and measure the height of the nonlocal resistance peak as a function of magnetic field in the absence of CST. We then remove the device from the cryostat and transfer freshly exfoliated CST on top of the channel of the Hall bar. The device is then loaded back into the cryostat, and the new heterostructure is characterized in a similar manner as the graphene-only device. Nonlocal measurements are again performed, and the height of the resistance peak in the presence of CST is compared to the height in the absence of CST. This before/after measurement allows us to extract information on the magnetic exchange field experienced by graphene.

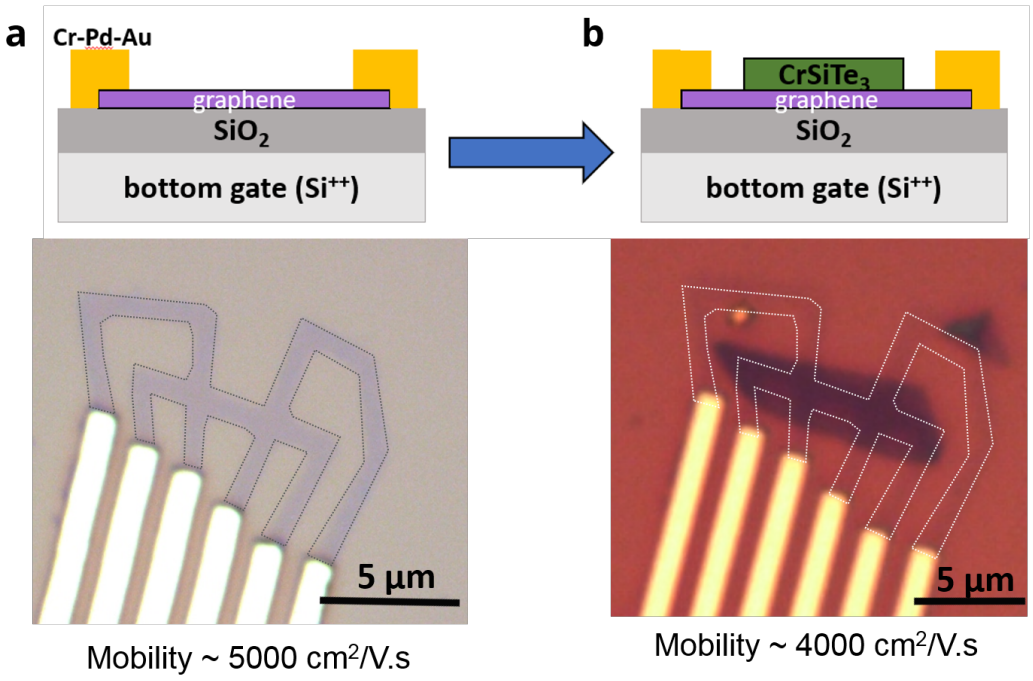

Figure 4.21: Pre-patterend graphene device **a)** before transfer of CST and **b)** after transfer of CST.

I will restrict discussion to one successful device, pictured in figure 4.21. We measured nonlocal transport in this device both before and after transfer of CST on top. Figure 4.22 directly compares the nonlocal resistance at 12T

external magnetic field. In the bare graphene device, a large peak at charge neutrality and a smaller peak at negative carrier densities (i.e. hole-doped) are observed. These two peaks have been measured in graphene before, and are located at the positions of $\nu = 0$ and $\nu = -4$ Landau level fillings. The $\nu = -4$ peak arises from orbital effects related to the quantum Hall effect, however the $\nu = 0$ peak is directly related to the Zeeman splitting in graphene, and thus can be enhanced by a magnetic exchange field. Transfer of CST causes an enhancement of the $\nu = 0$ nonlocal peak from $\sim$ 13 kΩ before transfer to $\sim$25 kΩ after transfer. This is nearly a two-fold enhancement of the nonlocal resistance due to proximity with CST. This peak appears much broader than before, such that the $\nu = -4$ nonlocal peak observed prior to CST transfer is no longer visible. We do not expect the position of the $\nu = -4$ peak to shift due to the presence of a proximitizing ferromagnet, since the quantum Hall effect is an orbital effect and magnetic proximity only affects spin, so we assume the broadening of the $\nu = 0$ peak obscures the $\nu = -4$ peak.

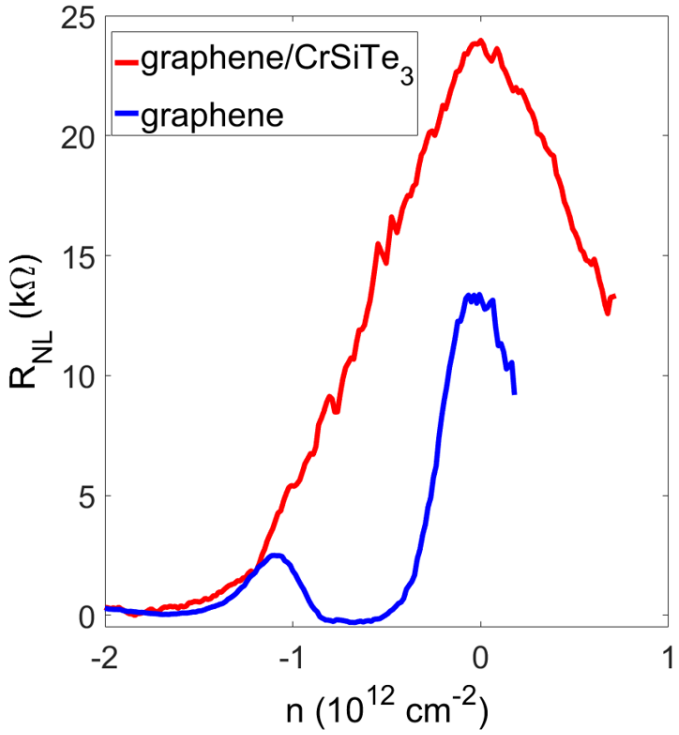

Figure 4.22: Nonlocal transport in graphene/CST device before/after transfer of CST. The CNP is seen to grow to a much larger resistance value, which would correspond to an enhanced effective magnetic field.

We initially attributed the increased nonlocal resistance to the magnetic exchange field between graphene and CST. In order to quantify the magnitude of the magnetic exchange field, we compared the height of the nonlocal peak vs. magnetic field both before and after transfer. The relationship between nonlocal resistance and external field is established by the bare graphene measurements before transferring CST. While a decreased mobility may affect the nonlocal resistance of bare graphene, this device experiences only a small decrease in mobility from $\mu = 5,000 cm^2/Vs$ before transfer to $\mu = 4,000 cm^2/Vs$ after transfer, so we expect nonlocal resistance to be roughly unaffected by the changed mobility. The increased nonlocal resistance is mostly due to the magnetic exchange field from the neighboring CST. The height of the nonlocal resistance peak, $R_{NL,D}$, is plotted versus magnetic field for both the graphene-only and graphene/CST structure in figure 4.23b. To extract the magnetic exchange field, we employ a fitting method used by Wei et al. in their study of graphene/EuS structures [64]. Here, they note that the nonlocal resistance, which has the following form:

$$R_{NL} \propto \frac{1}{\rho_{xx}} \left(\frac{\partial \rho_{xy}}{\partial \mu} E_Z \right)^2$$

can be recast into a much simpler form:

$$R_{nl} = R_0 + \beta(B) \cdot E_Z^2$$

where $\beta(B)$ is a parameter that represents the orbital effects manifest in the ρ_{xx} and ρ_{xy} terms. We determine the constant $\beta(B)$ from the graphene-only measurements, using $E_Z = \mu_B B$ as the Zeeman splitting energy, and assume it is unchanged when CST is transferred on top. After measuring the nonlocal resistance, the above equation is then used to determine E_Z in the presence of the magnetic exchange field. Using $E_Z = \mu_B B_{Zeeman} = \mu_B (B_{ext} + B_{MEF})$, we can calculate the magnetic exchange field experienced by graphene.

Figure 4.23 shows the calculated magnetic exchange field experienced by the spins in graphene. The value of 32 T at an externally applied magnetic field of 12 T indicates more than 2.5 times enhancement of the magnetic field, and points toward proximity magnetization in graphene.

These results have a few unexplained observations that differ from the proposed model of magnetic exchange in graphene. The first is the shape of the R_{nl} peak height vs B curves plotted in figure 4.23a. In a ferromagnet, the magnetization saturates above the coercive field, which is around 100 mT in CST. Using the model for the magnetic exchange field described above, we would expect the magnetic exchange field to saturate at the same external field

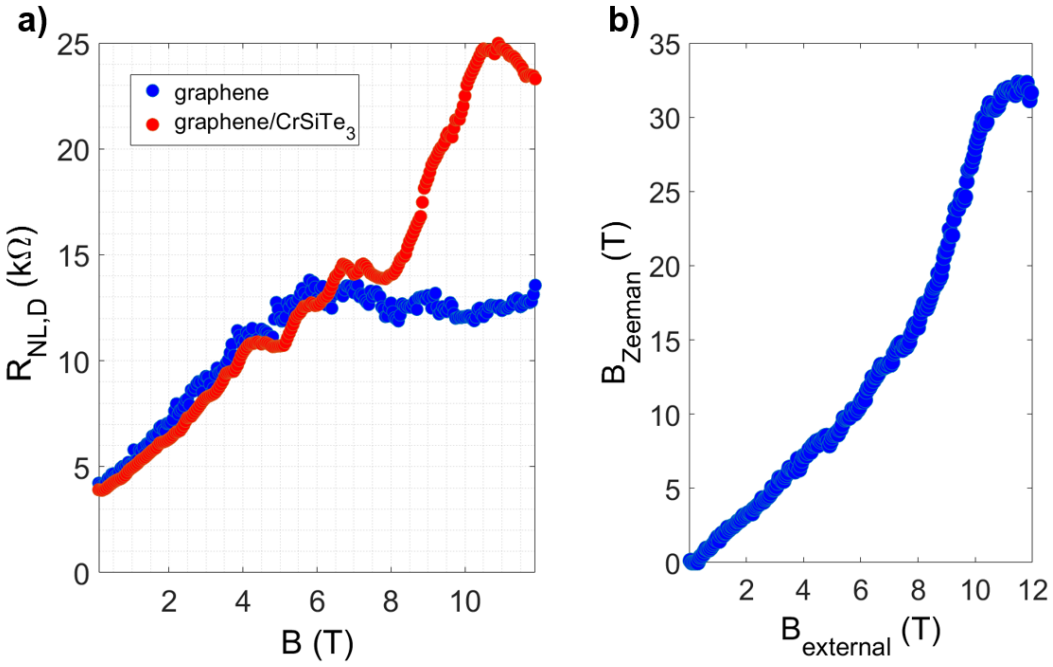

Figure 4.23: **a)** enhancement of the nonlocal resistance peak due to proximity to CST. **b)** Effective magnetic field experienced by graphene due to the MEF of CST. The effective field is more than 2.5 times the externally applied field.

as CST. In our measurement, this would correspond to a rapid increase in R_{nl} peak height below the coercive field and a relatively slower increase above it. Instead we observe steady growth of the nonlocal resistance even above the coercive field of CST. This is also observed in the graphene/EuS proximity study, where no saturation of the magnetic exchange field is observed.

Additionally, the R_{nl} peak heights for graphene and graphene/CST appear to line up well below $B_{ext} = 6T$ before the graphene/CST curve increases significantly over the graphene-only one. In the model presented above, we would expect the graphene/CST to be much greater than the graphene-only one at very low magnetic fields.

4.4.1 Electronic Difficulties and Non-Repeatability

After measurement of the device mentioned in the previous section, we became aware of a publication [79] discussing measurement artefacts in nonlocal transport. In this paper, they discuss that a spurious nonlocal signal can arise due to a "common-mode" voltage at the position of the red dot in figure 4.24. This voltage can cause a charge current down the channel of the device, and

due to differences in the contact resistance of the nonlocal leads, may cause a spurious nonlocal signal unrelated to the magnetic effects present.

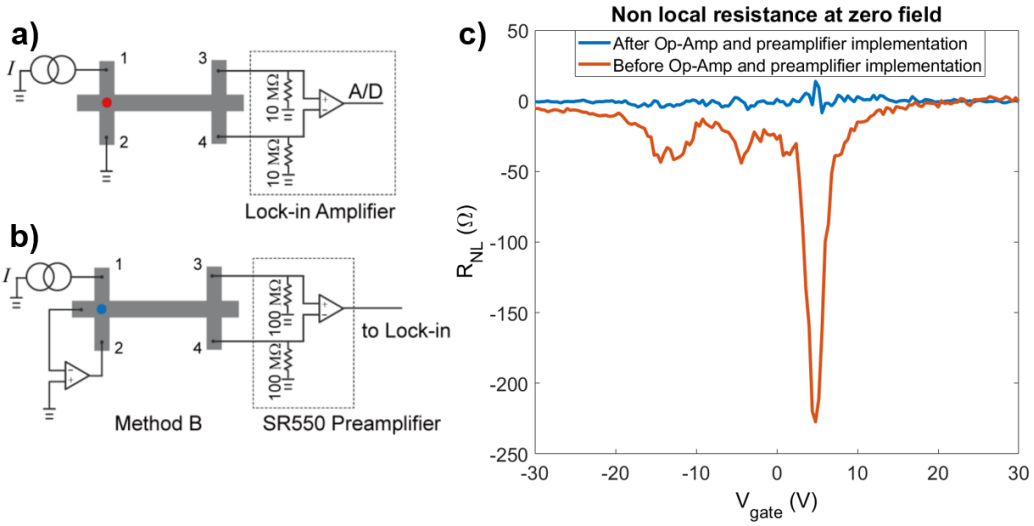

Figure 4.24: **a)** Measurement scheme for previous measurements. **b)** Same scheme but with precautions to account for a spurious voltage at the point indicated by the blue dot. This forces this point to be at a virtual ground. **c)** Nonlocal measurement at zero field both with and without the op-amp circuit. The spurious voltage signal is completely removed with the presence of the circuit.

Later measurements incorporated an op-amp circuit detailed in figure 4.24b. Here, an op-amp connected in feedback mode holds the point labeled by the blue dot at a virtual ground, eliminating the effects of a common mode voltage. Additionally, we used a voltage pre-amplifier which has a larger input impedance than the usual lock-in amplifiers (100MΩ vs 10MΩ). The gain of the pre-amplifier was set to unity so that the lock-in amplifier measured the same signal seen in the device, and is used exclusively for the high input impedance. Figure 4.24c shows the effect of the op-amp circuit on the nonlocal signal at zero magnetic field. The spurious peak at Vg = +5V is almost completely removed by the addition of this circuit.

The lack of this op-amp circuit in the device used in the previous section calls into question the validity of the results presented there. A large nonlocal signal at zero magnetic field is clearly seen in figure 4.23a, with the y-intercept of the plot at 5 kΩ both before and after transfer of CST. Unfortunately, during the course of measurement, majority of the electrical leads died, so subsequent measurement with the op-amp device were impossible.

Many additional graphene/CST devices were fabricated after the success of the previous device, however no device had large enough mobility to observe the enhanced nonlocal effects observed. Because of this, we are unable to confidently attribute the enhancement of the nonlocal resistance in the previous device to a proximity-induced magnetic exchange field.

4.5 Concluding Remarks

The above work represents approximately three years of research in magnetic exchange effects between graphene and magnetic 2D materials CrI_3, $CrSiTe_3$, and α-$RuCl_3$. Of these three, CrI_3 proved to be the most difficult, with incredible sensitivity to water in the atmosphere preventing any attempts to measure it. Despite precautions taken to reduce or eliminate degradation, devices proved to be unmeasurable after transfer of CrI_3. No transport features associated with the behavior of graphene or any 2D electron gas were observed. In graphene/$CrBr_3$ heterostructures measured in STM, material degradation still prevented measurement of a magnetic gap in graphene. Additional attempts at other universities also proved fruitless, leading us to abandon attempts to use chromium halides as a proximity magnet for graphene

In the graphene-$RuCl_3$ system, enhanced conductivity at all gate voltages points toward charge transfer between graphene and α-$RuCl_3$ bands. Signs of an antiferromagnetic transition are observed in this system due to a peak-dip feature in dR/dT, and the Néel temperature is well above the bulk α-$RuCl_3$ transition temperature. Additionally, the Néel temperature appears to be tunable in gate voltage, indicating an electrically tunable magnetic transition may be present in this system.

In one $CrSiTe_3$ device, enhanced nonlocal resistance in the presence of $CrSiTe_3$ implies a large magnetic exchange field in graphene as a result of the neighboring ferromagnet. Similar carrier mobilities are observed in both pre-transfer and post-transfer devices, indicating the presence of $CrSiTe_3$ does not detrimentally reduce device quality. However, other observations call into question the validity of these results, such as the lack of saturation of the magnetic exchange field, as well as the lack of repeatability following use of a more sophisticated electrical measurement.

5 Thickness Dependence of Intrinsic Flat Bands in Rhombohedral Graphite

I will now describe my recent measurement of intrinsic flat surface bands in rhombohedral graphite. The motivation for this work stems from the continued search for correlated states in materials. Electron interaction is usually excluded from models of solids, but some of the most exotic states of matter arise when they interactions become the dominant energy in the Hamiltonian. States such as superconductivity in cuprates, permanent magnetism in ferromagnets, and fractional quantum Hall states within a single Landau level are just a few such examples.

The search for strongly correlated materials had led researchers to flat bands: regions of the electronic band structure where electrons disperse weakly in momentum. This gives rise to a sharp peak in the density of states with a narrow band width W, implying the kinetic energy of charge carriers is small relative to the Coulomb energy. The assumption that electrons are non-interacting particles is thus invalid, and the ground state is determined by minimizing the Coulomb repulsion between electrons.

Recently, flat band states have been engineered in 2D material heterostructures by introducing a relative twist angle between constituent materials. In the most famous example of this, a superconducting state was observed in twisted bilayer graphene. In this work, researchers stacked two pieces of monolayer graphene together with a relative twist angle of $\sim 1.1^\circ$, and measured a transition to a superconducting state with a critical temperature of $T_c = 1.7$K. Fascinatingly, hybridization between adjacent Dirac cones in a moiré-induced "mini Brillouin zone" has the effect of reducing the Fermi velocity, flattening the band as twist angle approaches 1.1°, where the Fermi velocity drops to zero. In this flat band, the entire bandwidth is within 5-10 meV, and specific filling of this flat band gives rise to a superconducting state at low temperature [6]. The mechanism behind Cooper-pairing in twisted bilayer graphene is currently unknown, however many experimental and theoretical efforts have been made to further understand this state [5, 6, 80–84], with proposals suggesting either conventional electron-phonon coupling as in BCS theory or an unconventional Coulomb-driven pairing that resembles superconductivity in cuprates, which are well known for their relatively high critical temperatures. Critical temperatures in twisted bilayer graphene superconductivity have been measured as high as 3K by applying a large pressure to the heterostructure [5], however a further understanding of the mechanism behind this superconductivity holds the potential to elevate it further.

Since then, other interesting correlated phenomena have been measured in twisted bilayer graphene and other twisted-2D systems. Ferromagnetism was observed in twisted bilayer graphene at 3/4 filling of the flat band [8], leading to measurement of the quantum anomalous Hall effect without the need for magnetic dopants [7]. Additionally, in twisted WSe_2 bilayers and twisted WSe_2/WS_2 heterostructures, correlated insulator behavior is observed with a possible superconducting state in the former, indicating this phenomenon is not limited to just graphene heterostructures [9, 12]. Even further, heterostructures of trilayer rhombohedral graphite aligned to an hBN substrate showed signs of superconductivity at some fillings [85] and ferromagnetism at others [11]. Rhombohedral graphite, as mentioned previously in section 2.1.3, is an intrinsic flat band material, and the hBN substrate creates a moiré pattern that induces a small periodic potential, further flattening the existing flat bands and leading to observation of these phenomena.

In each of these works mentioned, flat bands are engineered in 2D heterostructures by taking advantage of the twist degree of freedom. It is more enticing however to work with a 2D material that has *intrinsic* flat bands. Rhombohedral graphite is an example of such a material, where a non-trivial bulk insulating state gives rise to topologically-protected flat surface states. These surface flat bands have motivated many experimental and theoretical studies, and early theoretical works suggested a number of different possible correlation-driven ground states, including high-temperature surface superconductivity from a BCS-like mechanism [86–88] and a weakly spin-polarized ferrimagnetic state [89, 90].

While early experimental works focused on an electric field-induced band gap in rhombohedral trilayers [91, 92], many recent experimental studies have observed correlation-induced effects, and the possibility of superconducting and ferromagnetic ground states in this system has reinvigorated interest in this system in recent years. As I mentioned previously, G. Chen *et al.* have measured rhombohedral trilayers aligned to a hBN substrate, and measured a tunable correlated Chern insulator in this system [10], where reversing the sign of the displacement field while the Fermi level is tuned to 1/4 filling of the moirè miniband switches between zero and finite Chern numbers. Additionally, this 1/4-filled insulator is ferromagnetic, exhibiting both magnetic hysteresis and a large anomalous Hall signal at zero magnetic field [11]. When doped away from the 1/4-filled insulating state, the system shows signatures of a superconducting transition for both electron and hole dopings [85], the nature of which (either correlation-induced or phonon-mediated) is still unknown. More recently, measurements of rhombohedral trilayers unaligned to hBN substrates have called into question the necessity of the moirè potential

induced by the hBN substrate in observing correlated states. H. Zhou *et al.* measured rhombohedral trilayer graphene unaligned to an hBN substrate and measured an unambiguous superconducting transition in multiple locations of displacement field/carrier density parameter space [93]. These transitions occur at the cusps of magnetic transitions in this system, where the system spontaneously transitions to a possibly spin- or valley-polarized state, breaking the intrinsic 4-fold spin and valley symmetries of graphene [94].

These correlated states in trilayer RG exist in only a narrow region of parameter space and only below a critical temperature in the millikelvin regime. A natural question is: how can one further enhance correlated effects in this system to potentially observe these effects at a larger temperature and a wider range of external parameters? While previous work attempted to use alignment to an hBN substrate to confine the bands enhance correlations, the flat bands in rhombohedral graphite grow flatter as thickness is increased, with electron dispersion loosely following $E \sim k^N$ for N-layer graphite [95]. This is a much simpler route to potentially enhance electron-electron correlations which does not require difficult alignment of atomic lattices, and would make these flat bands accessible to scanning probe techniques as well. While trilayer rhombohedral graphite has been measured extensively [10,11,85,91–94,96–99], multilayer rhombohedral graphite (defined as $N > 3$ for the purpose of this study) has received very little experimental attention [100–103]. Recently, rhombohedral multilayers have been studied experimentally via magnetotransport [100], and a magnetic transition was observed in samples ~ 10 layers thick at small hole-doping, indicating correlation effects similar to those measured in the trilayer exist in multilayers as well. A separate study measured rhombohedral tetralayers via scanning tunneling microscopy, observing a splitting of the surface flat band that may indicate either a charge transfer insulator or ferrimagnetic ground state [101]. Both of these studies leave many questions about true ground state of multilayer graphite systems and role of correlations in these materials.

In this chapter, I'll discuss my work measuring flat bands in rhombohedral graphite (RG). I utilize scanning tunneling microscopy and spectroscopy to measure the density of states of the metallic surfaces of three samples with $N = 5$, 9, and 14 layers each. This is the first thickness-dependent scanning probe measurement of rhombohedral graphite multilayers, as well as the first scanning probe measurement of RG greater than five layers in thickness. In the following sections I'll describe sample fabrication and characterization using Raman spectroscopy and the direct probing of the sharp density of states and other features as a function of thickness. I will also discuss our investigation of the rhombohedral/hexagonal phase boundary, as well as a thorough search

for correlated states in this system.

5.1 Thickness Dependence of Intrinsic Flat Band

5.1.1 Fabrication and Characterization

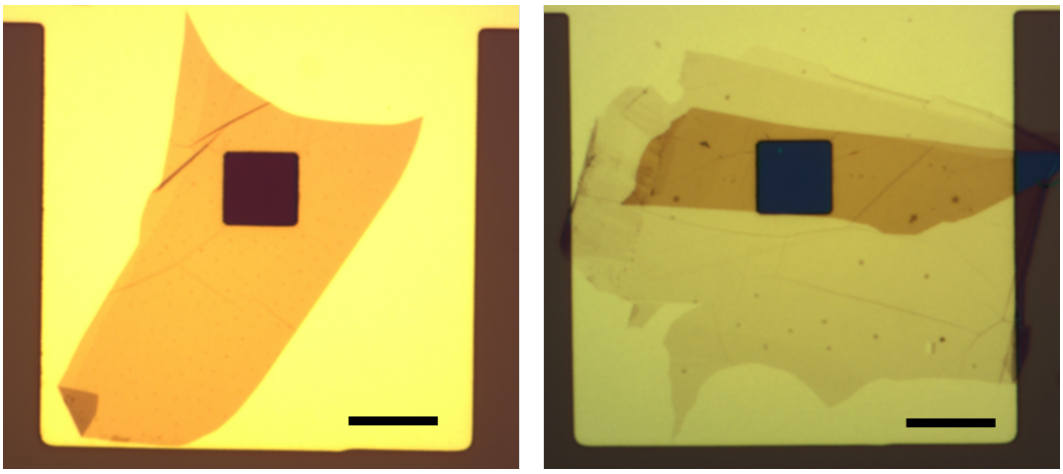

Figure 5.1: Images of two rhombohedral graphite devices measured in this study. **Left:** 14-layer thick RG on Au, with a small square in the middle on bare SiO_2 / Si. **Right:** 5-layer thick RG on an hBN substrate, all on the same substrate as the left. Scale bar is 10 μm in both images.

Graphite flakes of multiple thicknesses were mechanically exfoliated on 300 nm SiO_2/heavily doped Si substrates. Thickness was initially characterized optically, and flakes with thicknesses 5-15 layers were chosen. Cr/Pd/Au electrodes were pre-fabricated on 300 nm SiO_2/Si substrates, with a small square hole cut in the middle so that RG would lay on the insulating SiO_2 instead of the conducting Au. The square hole was added because RG has shown a smaller central peak width on insulating substrates in scanning probe measurements than RG on conducting substrates [97, 101, 103], however we were also interested in possibly gating the device. Unfortunately, for all thicknesses measured, gating was not possible due to strong electric field screening for thick flakes of rhombohedral graphite, where the effects of an external electric field are expected to be completely screened by the 4th graphite layer [104]. Exfoliated flakes were transferred onto the metallic electrodes using a dry transfer technique. It is well known that this transfer technique can alter the stacking order of RG, causing a mechanical shift in the layers and converting it to thermodynamically-favored hexagonal graphite (HG) phase [105]. Graphite

phase was only characterized post-transfer to ensure the rhombohedral portions remained on the finished device. Images of two devices are shown in figure 5.1. On the left is a 14-layer stack, and on the right is a 5-layer stack with an additional hBN substrate. The hBN acts as an atomically-flat substrate to improve STM measurement quality.

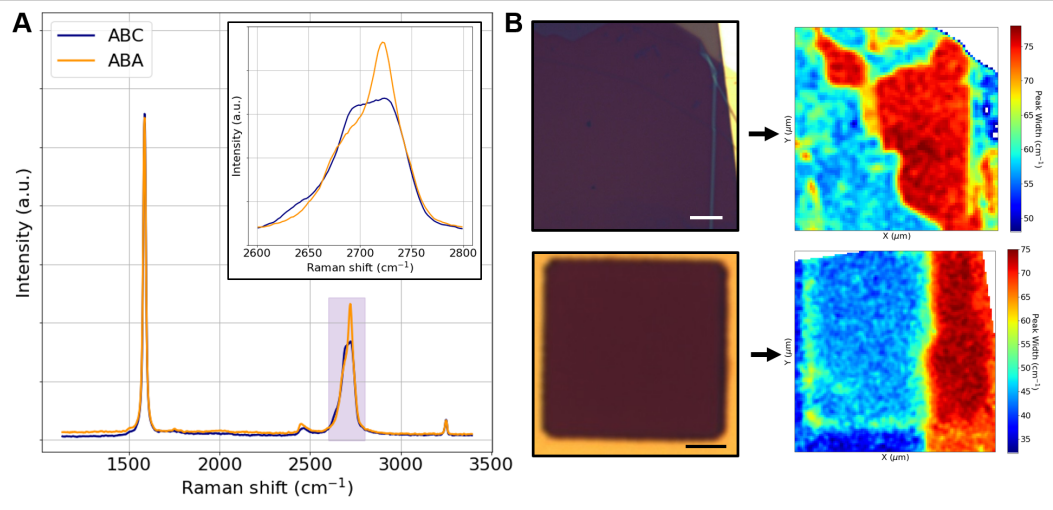

Figure 5.2: **a)** Raman spectrum for RG and HG. Inset shows a close-up of the 2D peak, with distinct lineshapes for RG and HG. **b)** Optical images and resulting Raman maps of two RG devices. Scale bar in the first image is 5μm. Scale bar in the second image is 2μm.

Raman spectroscopy is used to characterize stacking order of graphite flakes post-transfer. Raman spectra for both RG and HG are shown in figure 5.2a. The Raman signature of graphite has two peaks: the G-peak, located at a wavenumber of 1580 cm^{-1}, and the 2D peak, located at 2700 cm^{-1}. For rhombohedral graphite, the 2D Raman peak has a left skew and a larger width than the hexagonal phase, shown in the inset to figure 5.2a. The 2D peak width can be used to deterministically classify graphite phase of exfoliated flakes. By scanning over the sample and taking a grid of Raman spectra, the width of the 2D peak is used to generate a map of the sample area and classify regions as rhombohedral or hexagonal. Figure 5.2b shows both an optical image and the Raman mapping for two different devices, N=9 on top and N=14 on bottom. In both devices, a distinct line separating the rhombohedral and hexagonal phases is seen that is completely absent in the optical image. It is worth noting that areas of mixed phase were also observed in some samples, which is characterized by a decreased Raman width. This can be seen in the Raman

map of the N=9 flake in figure 5.2b, where a region with a peak width of 67 cm^{-1} is observed for a small portion of the flake. Fully rhombohedrally-stacked portions of graphite have the same peak width of 75 cm^{-1}, which was consistent between samples.

Devices were then annealed at 350°C under a flow of ∼5 sccm of forming gas (5% H_2 / 95% Ar) for 20 hours to remove polymers from the transfer process and clean the surface for STM measurements. This anneal does not destroy the rhombohedral portions of the flake, as confirmed by subsequent characterization of graphite phase. The devices were then loaded into the ultrahigh vacuum, low temperature scanning tunneling microscope. All measurements are taken on a commercial CreaTec low-temperature STM, with a helium bath temperature of 4 K, and resulting STM temperature of 4.7 K. The STM is equipped with an electrochemically etched tungsten tip, which was indented into gold before and between measurements. The lock-in frequency was set to f = 869 Hz in all dI/dV measurements.

5.1.2 Van Hove Singularity in N=5 sample

First, the topography of the sample was measured. Figure 5.3a shows a topographic image of the atomic lattice of rhombohedral graphite taken by constant-current scanning of the STM tip over top the sample. The atoms display an apparent trigonal symmetry, with the spacing between atoms a = 2.46 $\AA$ equal to the lattice constant of graphite. Only one sublattice in the unit cell of graphite is visible while the other appears dark, as illustrated in the inset of figure 5.2a. This phenomenon arises because, as mentioned in section 2.1.3, the low energy flat bands are centered on only one of the two sublattices on either surface, which act as the end-point of the SSH chain. The other sublattice has a γ_1 hopping partner on the layer below, which pushes its states to higher energies away from the Fermi level, resulting in a reduced local density of states on these sites and the dark appearance. This symmetry is expected for both RG and HG phases, and thus cannot be used to characterize stacking order.

The primary differences between RG and HG are in their spectroscopic signatures. Figure 5.3b shows spectra from both phases overlaid for the N=5 sample. While the HG spectrum smoothly increases as bias voltage is increased, RG displays a sharp enhancement of the dI/dV signal at positive bias voltage, around approximately +100 mV. This peak corresponds to the van Hove singularity in the surface states of RG, and is completely absent in the hexagonal phase. It occurs at slightly positive sample biases for all samples measured. In addition to the van Hove singularity, several ridges in the dI/dV

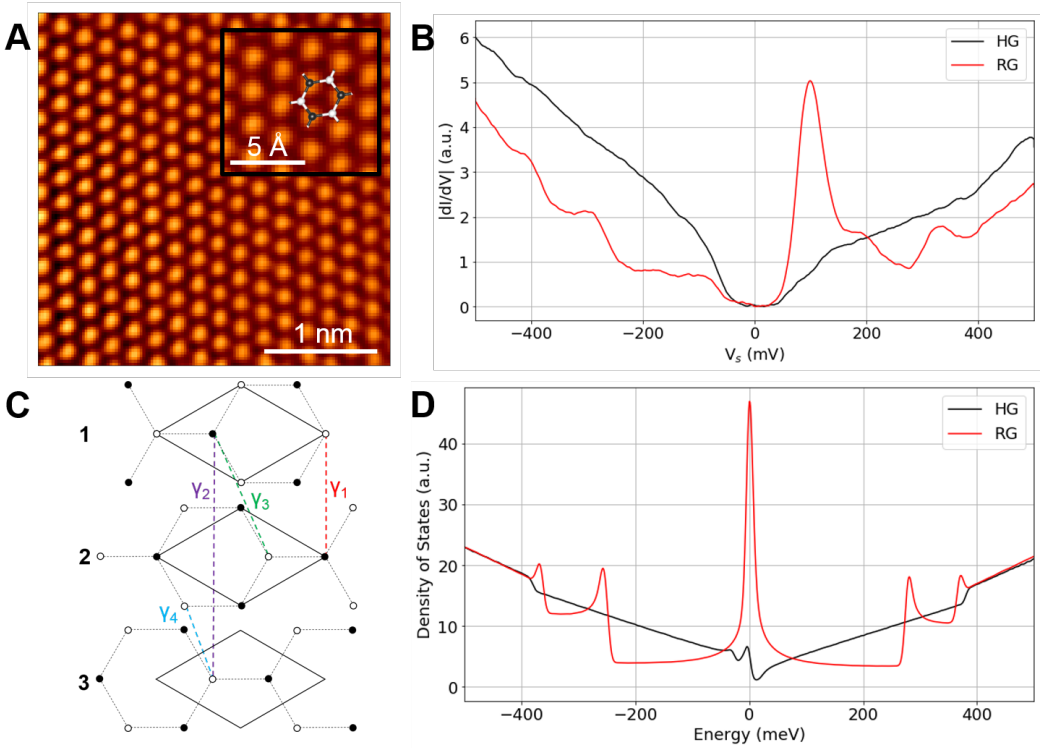

Figure 5.3: **a)** Topographic scan of RG. Inset shows a close up with a schematic of a graphene lattice overlaid. **b)** dI/dV measurements for both RG and HG. **c)** A schematic of the tight-binding model used for calculations of the density of states. **d)** Density of states for 50layer RG and HG, weighted to the top layer.

signal at negative bias voltages are observed. In the N=5 sample, these ridges occur at approximately -400 meV and -300 meV. These features correspond to valence band edges of states that have been pushed away from the Fermi level due to interlayer hopping γ_1 with the opposite sublattice on the layer below. While these bands can be thought of as "bulk bands", they are also expected in the local density of states of the "dark" atoms on the surface. Similar shoulders are observed at positive sample bias as well, however these features do not align well with conduction band edges expected for RG.

In addition to this peak, a gap feature between approximately ±65 mV about the Fermi level is observed in both spectra. This gap results from a phonon-mediated inelastic tunneling mechanism unique to graphite, which enhances all tunneling above or below the 67 meV out-of-plane graphene acoustic phonon mode at the K/K' points [106, 107]. Above/below ± 67 meV, electron

tunneling is strongly enhanced as electrons tunnel to the Gamma point, create an acoustic phonon with energy 67 meV and end in states close to the Fermi level at the K or K' points. This effectively shifts the position of all spectroscopic features by ±67 mV, depending on whether the feature is above or below the Fermi level, and appears as a gap pinned to the Fermi level. This phenomenon has been observed for multiple graphene/graphite tunneling spectra [106,108–111]. The gap exists in both rhombohedral and hexagonal graphite as the phonon-mediated process is expected in both systems. In our three samples, two exhibit this phonon gap while one does not. The presence or absence of this gap in graphite spectra has been extensively studied in literature, and it is related to the presence of adsorbed hydrogen at the surface of the sample [110]. This hydrogen can be picked up by the STM tip while scanning, and vibrational modes of adsorbed hydrogen create additional tunneling pathways that serve the same purpose as this inelastic tunneling mechanism. Thus, samples with excessive adsorbed hydrogen on the surface will not exhibit a phonon gap in their tunneling spectra. We clean these samples using a forming gas anneal containing 5% H_2, so the presence of hydrogen at the sample surface is not surprising.

The shift of the van Hove singularity to positive bias, which is expected to be centered around E = 0, can be explained by a couple of phenomena. First, the phonon gap previously mentioned shifts the peak by +67 mV. However if the peak were truly centered around E = 0, this would shift half of the peak to +67 mV and the other half to -67 mV. Instead, an apparent p-doping of the sample is observed, which shifts the van Hove singularity such that its entire width is found at positive bias. The magnitude of this doping changes between samples, and varies spatially across a single sample. We attribute this shift to surface contaminants that act as hole donors. The contaminants are likely adsorbed hydrogen on the surface layer, or interstitial hydrogen embedded just below the surface layer, the presence of which is expected due to the forming gas anneal used to clean the samples. This behavior has been observed in STM measurements of trilayer RG with similar cleaning processes as this study [91]. Accounting for both p-doping and the presence of the phonon gap, these measurements qualitatively match dI/dV measurements of three, four and five-layer RG measured previously [91, 96, 101, 102].

Shoulders at positive sample bias do not align well with conduction band edges. It is more likely that these features arise from tip-induced band bending, where the bands shift upwards at positive sample bias and cause the Fermi level to move into the first valence band, giving rise to an increased tunneling current and a peak in the dI/dV spectrum. This affects positive sample bias more strongly than negative bias due to the apparent p-doping of the sample

surface, causing the corresponding downward band bending at negative sample bias to be suppressed by the large density of states of the surface flat band. Because of this, conduction band peaks are not considered in further analysis.

5.1.3 Tight-Binding Modeling

In order to better understand the features of the density of states measurements, I created a tight-binding model of the electronic structure of rhombohedral graphite. The model is a pseudo-2D model, where k_z is not considered. The basis states are described by (layer) x (sublattice), giving a 2N-dimensional Hilbert space for an N-layer thick slab of rhombohedral graphite. In this model, I use the Slonczewski-Weiss-McClure tight-binding parameterization of graphite, which has commonly been used in both hexagonal and rhombohedral tight-binding models in the past [94, 95, 112]. This model includes γ_0 intralayer and γ_1 interlayer nearest-neighbor hopping between opposite sublattices located directly on top of one another, as well as additional higher order hoppings γ_2 through γ_4. The values used in this model can all be found in literature [94].

A brief summary of the hopping parameters for an RG stack are written below. I use the definition $\xi_i = \gamma_i \sum_{\langle j \rangle} \exp\left(-i\vec{k} \cdot \vec{\delta_j}\right)$, where δ_j are the lattice vectors to the nearest neighbors in graphene (described in section 2.1.1). Notice that $\xi_i(\delta_j) = \xi_i^\dagger(-\delta_j)$. All hopping pathways in RG can be described by the following:

$$\begin{aligned} A_i &\leftrightarrow B_i : \xi_0 & A_i &\leftrightarrow B_{i-1} : \gamma_1 \\ A_i &\leftrightarrow B_{i+2} : \frac{1}{2}\gamma_2 & A_i &\leftrightarrow B_{i+1} : \xi_3^\dagger \\ A_i &\leftrightarrow A_{i+1} : \xi_4 & B_i &\leftrightarrow B_{i+1} : \xi_4 \end{aligned}$$

An additional on-site energy reduction δ is included for the A sublattice on the top layer and the B sublattice on the bottom layer, as neither of these have an adjacent atom on the layer below/above. These hoppings are described pictorially in figure 5.3c, and generalizations to arbitrary thickness are straight forward. The Hamiltonian for a 5-layer RG stack is written below:

$$H\psi = \begin{pmatrix} \delta & \xi_0 & \xi_4 & \xi_3^\dagger & 0 & \frac{1}{2}\gamma_2 & 0 & 0 & 0 & 0 \\ \xi_0^\dagger & 0 & \gamma_1 & \xi_4 & 0 & 0 & 0 & 0 & 0 & 0 \\ \xi_4^\dagger & \gamma_1 & 0 & \xi_0 & \xi_4 & \xi_3^\dagger & 0 & \frac{1}{2}\gamma_2 & 0 & 0 \\ \xi_3 & \xi_4^\dagger & \xi_0^\dagger & 0 & \gamma_1 & \xi_4 & 0 & 0 & 0 & 0 \\ 0 & 0 & \xi_4^\dagger & \gamma_1 & 0 & \xi_0 & \xi_4 & \xi_3^\dagger & 0 & \frac{1}{2}\gamma_2 \\ \frac{1}{2}\gamma_2 & 0 & \xi_3 & \xi_4^\dagger & \xi_0^\dagger & 0 & \gamma_1 & \xi_4 & 0 & 0 \\ 0 & 0 & 0 & 0 & \xi_4^\dagger & \gamma_1 & 0 & \xi_0 & \xi_4 & \xi_3^\dagger \\ 0 & 0 & \frac{1}{2}\gamma_2 & 0 & \xi_3 & \xi_4^\dagger & \xi_0^\dagger & 0 & \gamma_1 & \xi_4 \\ 0 & 0 & 0 & 0 & 0 & 0 & \xi_4^\dagger & \gamma_1 & 0 & \xi_0 \\ 0 & 0 & 0 & 0 & \frac{1}{2}\gamma_2 & 0 & \xi_3 & \xi_4^\dagger & \xi_0^\dagger & \delta \end{pmatrix} \begin{pmatrix} A1 \\ B1 \\ A2 \\ B2 \\ A3 \\ B3 \\ A4 \\ B4 \\ A5 \\ B5 \end{pmatrix} \tag{4}$$

A small grid of k-points surrounding the K and K' points in the Brillouin zone is established, and eigenvalues of the Hamiltonian for every k-point in this grid are calculated. I calculate these eigenvalues only in a small vicinity around the K and K' points because the low-energy states accessible by tunneling only exist in these regions, and states at other k-values are too high energy for our tunneling measurements. Thus the entire behavior of our system can be captured considering only these points. The band structure centered around these points is calculated, and the density of states is found by taking a histogram of the band structure. The histogram can be weighted by the amplitude of each eigenvector on only the first layer in the sample, $|\psi_{A1}|^2 + |\psi_{B1}|^2$. This converts the full density of states into a local density of states of the surface, and thus more accurately reflects the measurements of a surface technique. Figure 5.4 details this calculation for a N=9 sample, with an additional broadening term $\sigma = 5$ meV included in the density of states calculation.

Figure 5.3d shows a calculation of the surface density of states for five layer samples of both RG and HG. A broadening term $\sigma = 5$ meV has been included as well, which is similar to instrumental broadening expected from the finite modulation voltage used in the experiment (5 mV for most measurements). Both calculations bear many similar qualities to our measurement. The sharp van Hove singularity resulting from the flat surface bands is seen close to zero. In dI/dV measurements, this peak is shifted to positive energy by both the overall p-doping as well as the phonon gap acting constructively, neither of which are included in this calculation. The lower energy valence band onsets are seen as peaks at negative energies. In dI/dV measurements at negative bias, the combined effects of the p-doping and phonon gap counter each other, resulting in the density of states peaks nearly aligning with the shoulders in the dI/dV measurements. With these effects in consideration, the density of

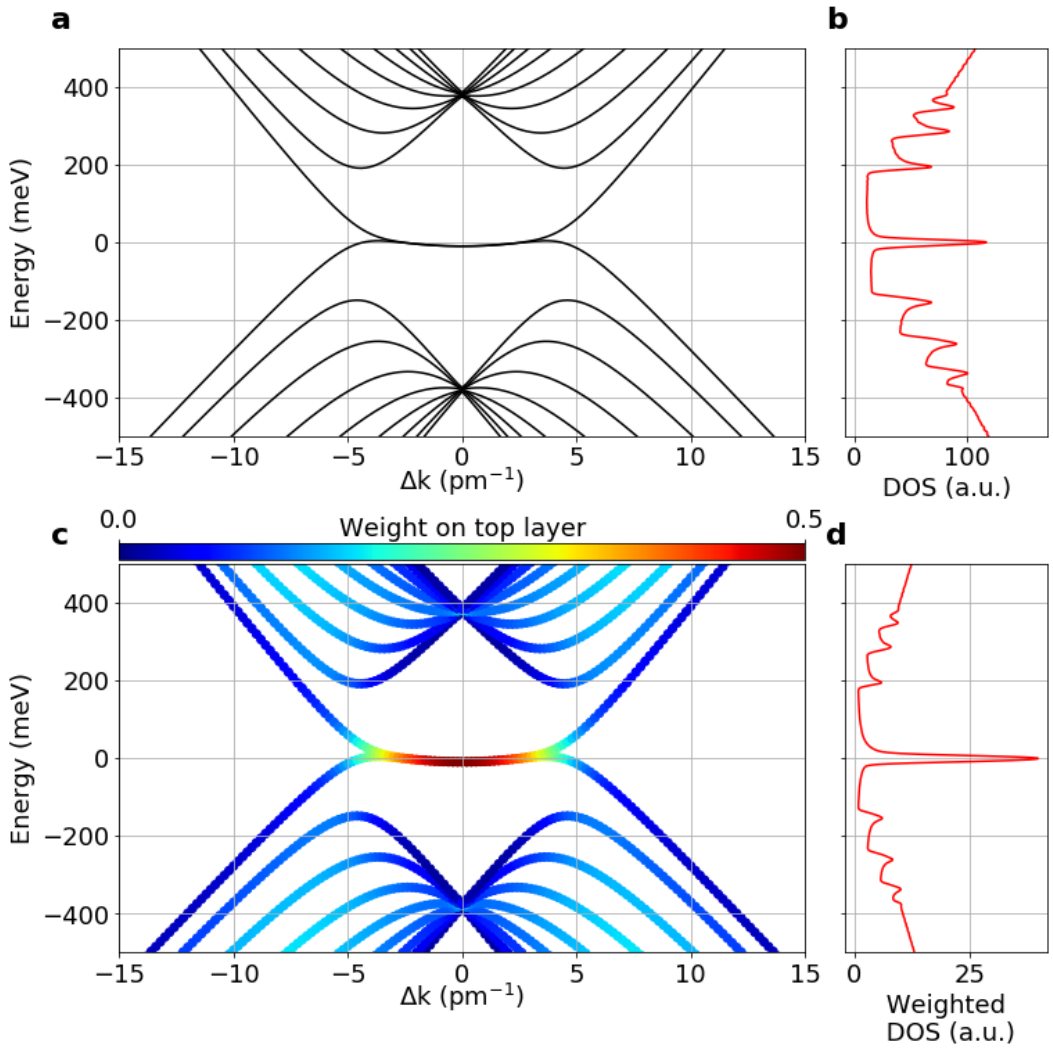

Figure 5.4: Band structure and density of states of N=9 RG. **a** Band structure calculated using model described above, with equal weight on all layers. **b** Density of states of (a) **c** Band structure in (a) weighted to the top layer, $|\psi_{A1}|^2 + |\psi_{B1}|^2$. **d** Density of states of (c).

states calculation agrees well with dI/dV measurements.

5.1.4 Thickness Comparison of Spectroscopic Data

We now turn our attention to a comparison of these spectroscopic features as a function of graphite thickness. Flakes of three different thicknesses (N

= 5, 9 and 14 layers) were measured, and the resulting spectra are shown in figure 5.5a. The sharp dI/dV peak is observed in every spectrum, highlighted in green, and grows in height as sample thickness is increased. The density of states calculated from a dI/dV measurement depends on both the tip density of states and the true tip-sample separation distance, both of which are unknown. This makes quantitative comparison of heights between dI/dV measurements difficult. However, comparing the height of the central peak relative to the height of the first valence band onset is an accurate method of comparing the sharpness of dI/dV features between measurements. A plot of the central peak height relative to the first valence band onset is shown in figure 5.5b, averaged for multiple different tips and sample areas. The relative height grows as sample thickness increases, indicating the van Hove singularity is growing sharper as sample thickness increases. The decrease in the peak width as thickness increases, shown in figure 5.5c, further corroborates this. This is in good agreement with the tight-binding model for the system, which predicts a surface flat band that grows flatter with thickness.

In addition to the growth of the central peak, the lower energy valence band onsets, highlighted in purple in figure 5.5a, become more numerous and more tightly spaced as thickness increases. This result is also seen in tight-binding models for the system, where each additional layer adds one valence band and one conduction band. The peak energy vs. peak position relative to the van Hove singularity (called "peak index" here) is shown in figure 5.5d, where dashed lines indicate experimental data and solid lines indicate calculations from tight binding. The energies of these peaks have been adjusted to account for the presence of the phonon gap, where peaks below E = 0 have been shifted up by 65 meV and peaks above E = 0 have been shifted down by 65 meV. These peaks have also been adjusted to account for doping of the system by surface contaminants, and all peak energies have been given a constant shift so that the peak corresponding to the surface flat band aligns with the expected position from the tight-binding model. We see good agreement between the experiment and tight-binding model, and dI/dV peaks at negative bias align well with valence band peaks in the density of states calculated using the tight-binding model. These valence band onsets serve as another confirmation of the increasing thickness of the samples, and additionally confirm the absence of stacking faults that would alter the number and spacing of these peaks.

As an aside, we have also (inadvertently) observed the influence of surface cleanliness and what we believe to be H contamination of the surface. As I mentioned previously, all samples were annealed at 350°C under a flow of 5 % H_2 / 95 % Ar forming gas for several hours before measurement. A small kink was found in the forming gas line that supplies the anneal after

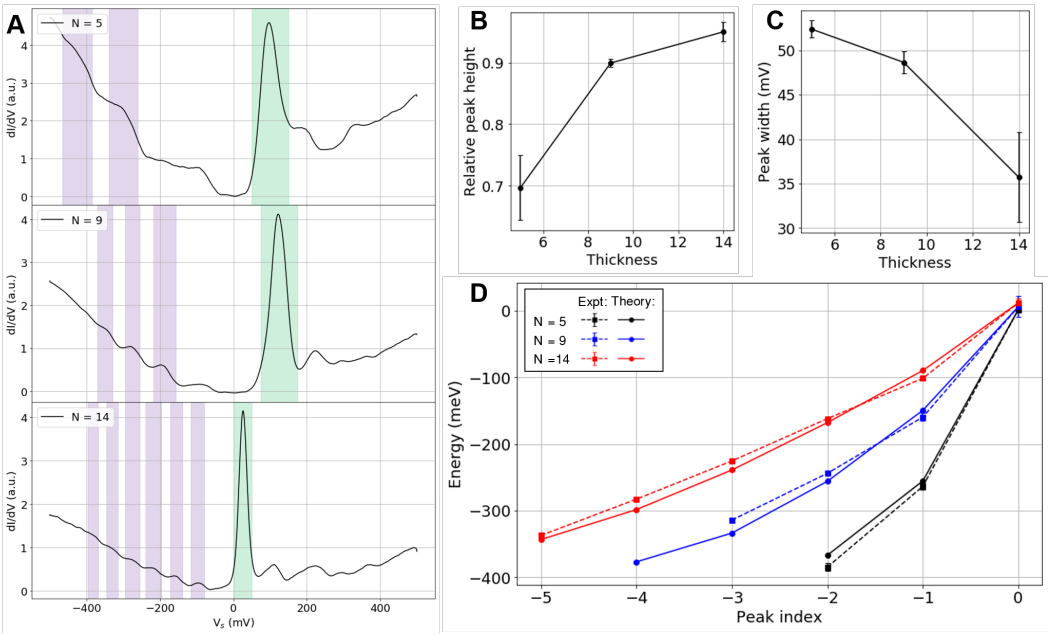

Figure 5.5: **a)** Comparison of N=5, 9, and 14 layer graphite samples. The sharp flat band is highlighted in green, while the higher energy band onsets are highlighted in purple. Peak **b)** height and **c)** width of the van Hove singularity vs sample thickness. "Relative height" compares the height of the central peak to that of the first valence band peak. **d)** Positions of higher energy peaks vs. peak index (relative to the van Hove singularity) for each device thickness. Dashed lines with square symbols indicate experimental data, while solid lines with circular symbols are calculated using the tight binding model. Error ranges are visible for peaks with index 0, but are too small to see for other peaks.

both anneal and measurement of the N = 5 and N = 9 samples that was not present when annealing the N = 14 sample, meaning the N = 5 and N = 9 samples did not receive as strong of a cleaning process and had more surface contaminants. This is seen in experiment as a large p-doping of these samples, causing a shift of all features towards positive sample bias. This has been accounted for in analysis of peak positions presented above. This type of doping was also seen in previous transport devices of graphene on bare SiO_2, which were reported earlier in this thesis in section 4. In addition, the phonon gap was observed in the N = 5 and N = 9 samples, but is absent in the N = 14 sample. We believe this to be the result of H contamination of the surface due to the significantly stronger forming gas anneal this sample

received. Scanning across the sample causes the tip to pick up H atoms, and vibrational states from these clusters of atoms cause a tunneling enhancement in a similar manner as the phonon-mediated process mentioned above, through a mechanism described in detail in reference [110]. This is corroborated by the observation of a sharp negative differential conductivity (figure 5.6) after continued scanning in this sample, the lineshape of which matches almost exactly with that seen in the last figure of reference [110] and is associated with a strong excess of adsorbed hydrogen at the apex of the tip. All measurements reported above are performed quickly after tip-forming, meaning there was too little scanning to cause an excess of hydrogen to accumulate on the tip, and the sharp negative differential conductivity was not observed.

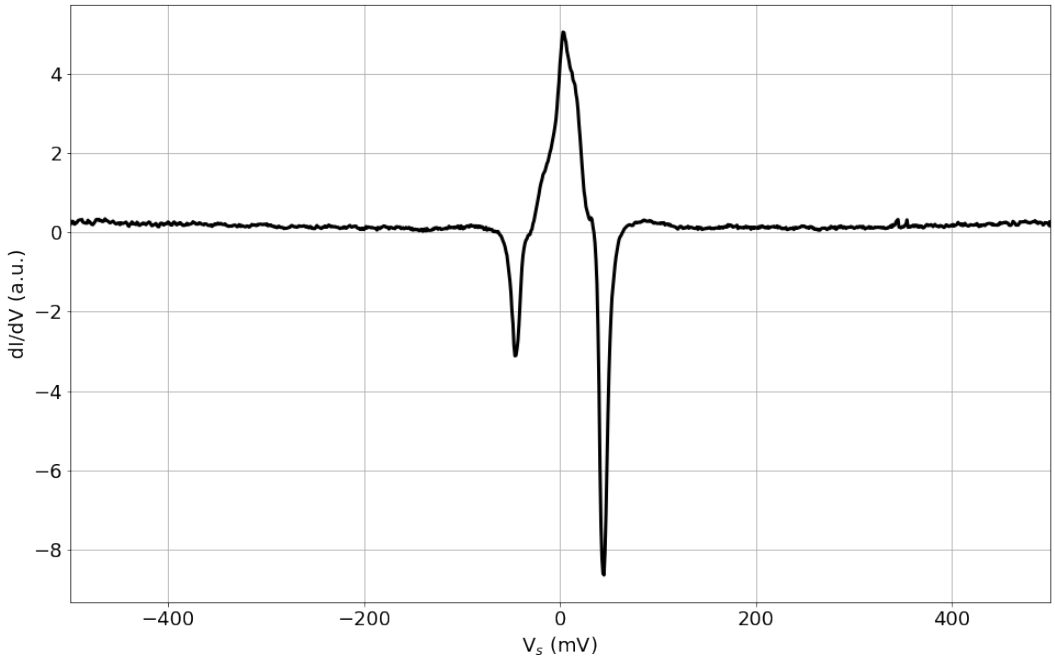

Figure 5.6: Negative differential conductivity observed in the N=14 sample, which exhibited strong H-contamination of the surface. This effect is seen in controlled experiments of H-contamination as well [110].

The above represents the first thickness-dependent measurement of the density of states of rhombohedral graphite. In the next sections, I'll discuss measurements performed on the thickest sample, 14-layer rhombohedral graphite. This sample has the flattest surface bands of any sample we fabricated, and thus the highest chance of exhibiting correlated electron physics at the temperatures achievable in our STM. I'll discuss the recent measurement

of the boundary between the rhombohedral and hexagonal phases where differences in stacking order result in various features of the dI/dV signal, as well as a splitting observed in the van Hove singularity that may point toward a correlated gap in the system.

5.2 Rhombohedral-Hexagonal Phase Boundary

The boundary of a material holds significance when studying materials of a topological nature due to the bulk-boundary correspondence principle. Briefly, this states that the boundary separating two topologically distinct insulators should host an edge state, where the band gap closes as the topological phase

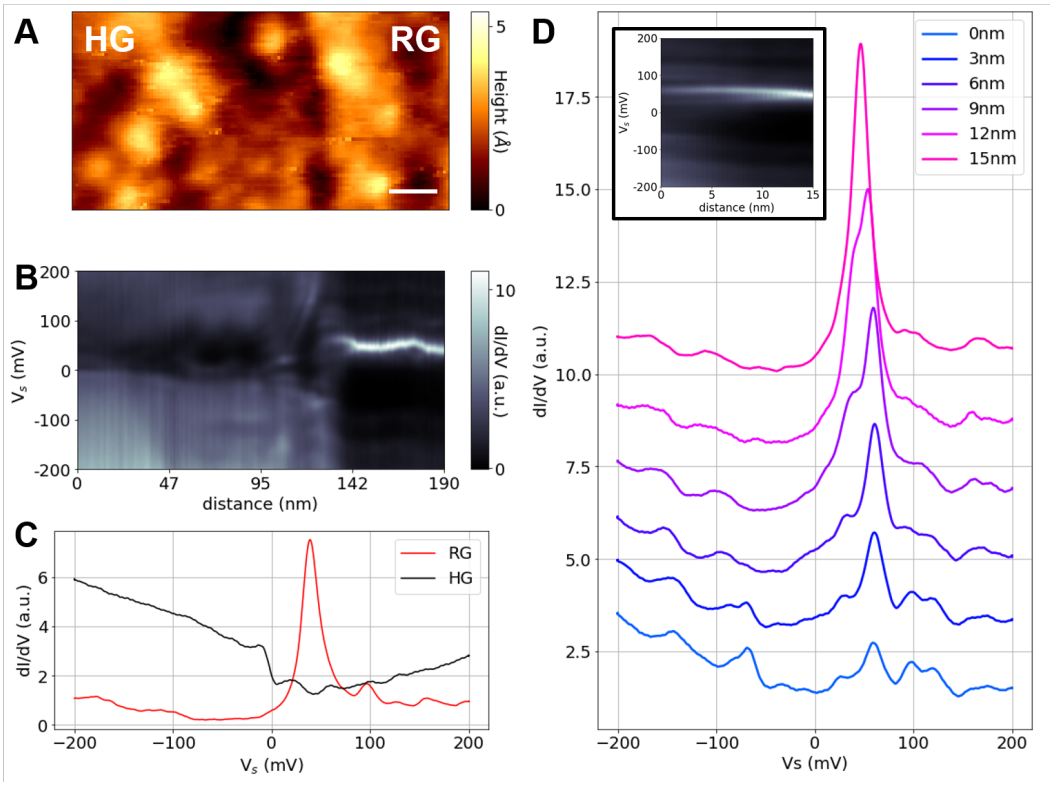

Figure 5.7: **a)** Topography of the boundary shows a small line separating the two phases. Scale bar is 25 nm. **b)** Line scan showing evolution of the density of states across the boundary. **c)** Comparison of individual spectra for RG and HG regions on either end of the line scan in b). **d)** Waterfall plot showing the evolution of the central peak as the hexagonal phase is approached from the right.

changes. Since the bulk of RG is a topological insulator due to its similarities with the famous Su-Schrieffer-Heger model, it is thus of interest to study the topological nature of these surface states. Previous studies of four-layer RG showed a gap in the surface spectrum that itself was topologically nontrivial, indicated by the presence of an edge state at the boundary between rhombohedral and hexagonal stacking [101].

Conveniently, the 14-layer sample had an easily accessible boundary between rhombohedral and hexagonal phases. Figure 5.7a shows the topography of the phase boundary, and a weak ridge is visible separating the two phases. The left portion of the image is hexagonal, while the right portion of the sample is rhombohedral. The sample itself has some inherent roughness due to the underlying SiO_2 substrate, however the RMS roughness of 80 pm is well within a single atomic layer of graphene.

Figure 5.7b shows several spectra taken along a line perpendicular to this edge, aligned to the topographic image above. The right most spectrum in each line scan shows clear rhombohedral behavior while the left-most spectrum shows hexagonal behavior, highlighted in figure 5.7c. As the hexagonal region is approached from the right, the central rhombohedral peak splits into two peaks that decay in height, and the first two valence band onsets shift inward. Beyond this, a series of peaks is observed that do not exactly match with features in rhombohedral or hexagonal graphite, until expected hexagonal behavior is recovered approximately 50 nm after the start of phase change.

A close-up of the rhombohedral-hexagonal boundary is shown in the inset of figure 5.7c, and several linecuts from this region are shown in the plot in 5.7c. The splitting of the central rhombohedral peak occurs over a length of approximately 15 nm. The shape of this peak is qualitatively similar to DFT calculations of an edge state in four-layer graphite from [101], although it is shifted to positive sample bias. It should be noted that neither RG or HG have a gap in their electronic spectrum, so it is unreasonable to call this a topological edge state in this case.

Instead, it is more likely that this is the result of small changes in stacking order as the flake transitions from rhombohedral to hexagonal. A stacking fault in RG occurs when the uniform shift of several layers of graphite causes a local ABA-type stacking within the bulk of the RG flake. This splits the full rhombohedral stack of thickness N into two rhombohedral stacks of thickness N_1 and $N_2 < N$, which is detailed in figure 5.8a. The behavior of surface states closely resembles that of the stack on top (N_1), with the energy structure of the surface flat band changing adiabatically from that of an N-layer stack to that of an N_1-layer stack. Introduction of many of this type of fault in succession would cause a shift of the overall stacking from ABC to ABA.

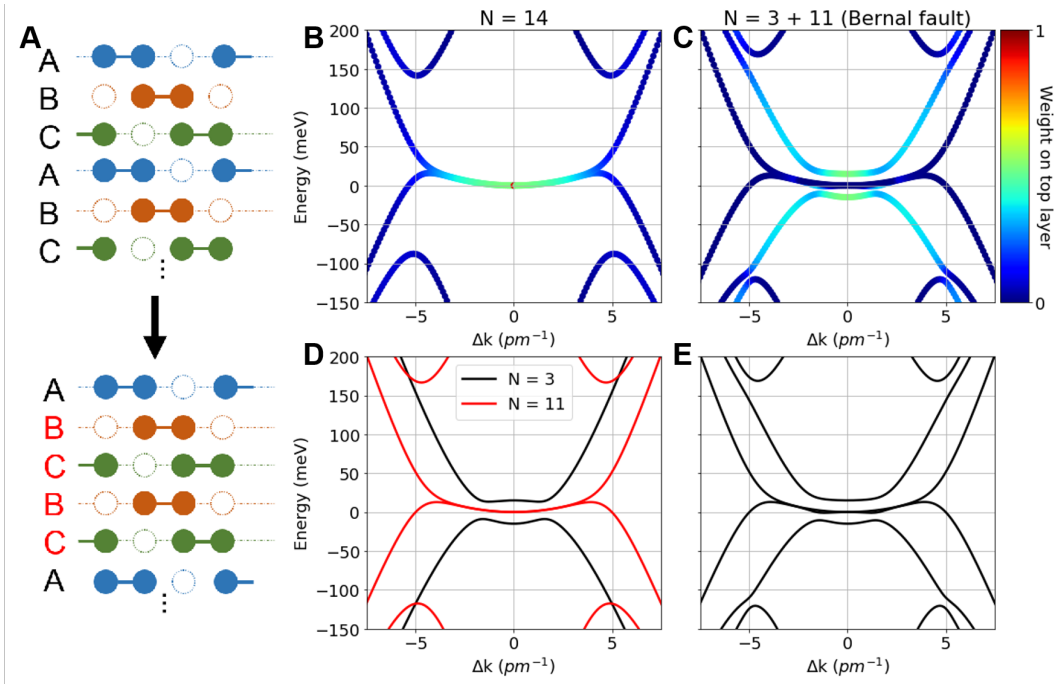

Figure 5.8: **a)** Schematic for a possible stacking fault in ABC graphite. **b)** Band structure for an N = 14 RG stack with no stacking faults, weighted to the top layer **c)** Weighted band structure for an RG stack with a Bernal fault between the 3rd and 4th layer, resulting in a N = 3 + 11 stack. **d)** Band structures of an N = 3 and N = 11 RG stack plotted together, for comparison to **e)** the unweighted band structure of the N = 3 + 11 stack.

Looking at the specific phase boundary in the inset of figure 5.7c, we observe a splitting of the central peak into two smaller peaks that decay in height, as well as an inward shift of the first valence band onset. Both of these features can be explained by the introduction of a ABA stacking fault between the 3rd and 4th layers. This splits the fully-rhombohedral stack into two rhombohedral stacks of thickness $N_1 = 3L$ and $N_2 = 11L$. The low-energy band structure for this structure is shown in figure 5.8c, where line color represents the weight of each state on the top-most layer. Comparing this with the low-energy band structure from a N=14 stack in 5.8b, one can see the surface state splits apart into to two flat bands located above and below the Fermi level, while the first valence band moves inwards toward the Fermi level. In fact, the low-energy band structure closely resembles that of two independent RG stacks of N=3 and N=11, which are depicted together in figure 5.8d (which can be compared to the unweighted N = 3 + 11 band structure in figure 5.8e). This calcula-

tion qualitatively matches observations, and explains the features close to the start of the phase transition on the rhombohedral side. Although this model doesn't capture the full phase change, it serves to highlight that the features observed most likely originate from local changes in stacking order during the phase change.

5.3 Search for Correlated States in N=14 Sample

The most compelling reason to study materials with flat bands is the possibility of observing correlated electron states. States arising from interacting electrons can show up as a gap in the electronic spectrum separating the different states. For example, a superconducting state is often characterized by a superconducting gap, the size of which is determined by the binding energy of cooper pairs. Additionally, a correlated ferromagnet may exhibit a spin-gap, where the gap size indicates an energetic favorability of one spin over another, as in quantum Hall ferromagnetism. In the N = 5 and N = 9 samples, strong p-doping caused by poor surface cleanliness moved the Fermi level outside of the surface flat band. Due to our inability to gate, it was impossible to move the Fermi level into the flat band, which means it is impossible to measure any correlated electrons states in these samples. However, in the N=14 sample, p-doping is minimal and the flat band is located relatively close to the Fermi level. Because of this, an investigation into possible correlated states was performed in the thickest sample.

Figure 5.9a shows a double-peak feature in the dI/dV spectrum of RG that was observed in some regions of the rhombohedral graphite sample. The N = 14 sample has a relatively low p-doping, and the level of this doping varied across the sample. It is possible that some regions are doped strongly enough to entirely move the Fermi level out of the flat band, while other portions were not doped nearly as strongly, resulting in a Fermi level within the flat band and the possibility of correlated states. The gap between these peaks is approximately 25 meV, which is similar to gap sizes calculated by Kerelesky *et. al* [101] describing charge transfer insulator and spontaneous ferrimagnetic states. In order to investigate the nature of this gap, we measured its behavior in magnetic field, which is shown in figure 5.9b. As seen, the gap displays no change in magnetic field, meaning it is either not magnetic in origin, or is unaffected by the magnetic field accessible in this STM (which is limited to +1T).

However, there are many reasons why a double peak feature like this may be observed in STM that are unrelated to any correlated state. First, a peak in the density of states of the tip may cause a double peak similar to that

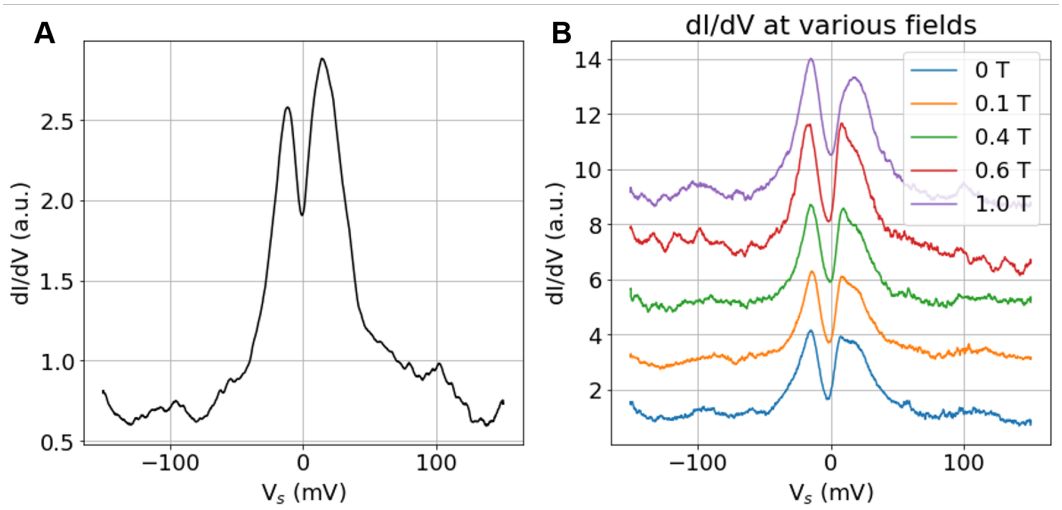

Figure 5.9: **a)** Double peak feature in the van Hove singularity measured for the N=14 sample. **b)** Evolution of the double peak in magnetic field.

observed here. As I mentioned in section 3.4, the tip DOS is usually assumed to be constant, so peaks in the tip DOS are undesirable during measurement. The presence of a tip peak at the same location as the flat band in RG would appear as a double peak symmetric about E=0, which is similar to what is observed. Second, as mentioned in the previous section, a change in the local stacking order by introduction of a Bernal fault between the 3rd and 4th layers would cause the appearance of a double peak feature similar to this. Historically, STM measurement of graphite has been plagued by motion of the top few layers of graphite, where the STM tip causes permanent sample deformation [113]. While some researchers have used this to their advantage in recent years [114], this permanent sample deformation is usually undesirable. It is possible that a local deformation of the top three layers occurred, causing this style of splitting of the central peak.

Ultimately, we decided not to explore this feature any further. The inability to gate the sample due to strong interlayer screening in RG [104] means we can only study the feature by varying magnetic field, and cannot finely tune the Fermi level within the gap. Additionally, the appearance of the feature at some regions of the sample and not in others meant it was nearly impossible to locate and study, as no topographical features indicated its presence or absence. Lastly, the feature appeared to disappear and reappear with different tips, strongly suggesting that it is in fact a tip-related feature arising from a non-constant tip density of states rather than an effect of a correlated gap

caused by the Fermi level entering the flat band.

5.4 Conclusions

This work represents the first measurement of the density of states of rhombohedral graphite as a function of thickness. Samples of N = 5, 9 and 14 layers with rhombohedral portions were measured using scanning tunneling microscopy, and a large peak in the density of states that grows with sample thickness was measured. This peak arises from the flat, conducting surface bands, which grow flatter as thickness increases. This represents the first such measurement of this phenomenon. A tight binding model was employed that explains the features observed in the spectra, illustrating the growing height of the central peak as well as the presence of valence band edges at negative bias voltages. The model is in good agreement with experimental results. The rhombohedral/hexagonal phase boundary displays features that align with the introduction of stacking faults across the boundary. P-doping of the N=5 and N=9 samples prevented investigation of correlated gaps in these systems. A possible double-peak feature within the flat band was measured in the N=14 sample that was unaffected by magnetic field, however the inability to gate the device as well as the elusive nature of the peak prompted the decision to not study this feature further.

There still remains plenty of work studying possible correlated states in this system. While RG thicknesses used in this study display a strong interlayer screening that prevents gating of the thickest samples [104], it is possible that thinner RG flakes such as N = 3-4 do not experience a full screening of the electric field induced by a bottom gate, allowing tuning of the Fermi level into the flat band. This in turn could lead to the observation of correlated gaps that only appear at certain gate voltages, and the nature of these gaps in magnetic field could be explored. Even further, study of these systems in dual-gated transport or capacitance measurements may lead to interesting correlated physics that cannot be measured in an STM due to the necessity of an open face device geometry for scanning-probe access. All in all, the demonstration of the increasing flat band with sample thickness shown here serves to highlight that even a relatively simple material like graphite may still possibly host exotic states of matter that have yet to be fully explored.

6 Conclusions and Future Directions

The revolution of 2D materials has created a new paradigm for designing both topological effects and correlated effects in 2D heterostructures. Using creative ways of combining materials' different properties, many proposals utilize proximity effects to design unique topological properties, or use moiré engineering to create flat dispersions in the band structure that encourage many-body effects. This work has focused on two such experiments: the observation of a magnetic proximity effect in an all-2D device structure and the measurement of intrinsic flat bands in multilayer rhombohedral graphite that do not require moiré engineering. I'll briefly summarize my results and discuss a possible route toward future research that could be pursued.

In chapter 4, I discussed experiments towards realizing a designed topological effect in 2D materials. I talked about my experiments in heterostructures of graphene with various 2D magnetic materials, in search of a magnetic proximity effect between these materials. While high device quality was observed in bare graphene devices, the ferromagnets used universally degraded before measurement, highlighting the highly sensitive nature of these materials. Even using some of the best protective measures available, I was unable to stop degradation of these materials from reducing the graphene transport quality, which ultimately made measurement of any fine magnetic gaps impossible. In heterostructures of graphene and anti-ferromagnetic α-$RuCl_3$, I demonstrated that a proposed ferromagnetic transition was absent in our devices, and that instead we observed an elevated anti-ferromagnetic transition that itself was tunable in gate voltage. This transition may or may not be occurring in the graphene layer itself, but it is impossible to conclude this in transport measurements as a conduction channel opens in the α-$RuCl_3$ surface layers, and transport in this channel is measured in parallel with graphene.

In chapter 5, I discussed measurement of intrinsic flat bands in rhombohedral graphite, which could potentially host correlated physics at low temperatures. I demonstrated that the density of states of the surface band increases with increasing rhombohedral thickness, the first such measurement of this phenomenon. Peaks in dI/dV corresponding to valence band onsets are observed that agree nicely with tight-binding calculations, which demonstrates the lack of stacking faults in these rhombohedral graphite flakes. I performed an investigation of the rhombohedral/hexagonal phase boundary, and while I did not observe any topological effects, I measured features corresponding to specific stacking faults that can be compared to tight-binding models of these faults. I searched for correlated states within the surface flat band, but the position of the Fermi level outside of the flat band and the inability to gate the

samples due to their thickness halted further investigation of any many-body effects.

There remains plenty of work to be done in the rhombohedral graphite system. It could be possible to use the STM tip itself as a second gate, allowing adjustment of the Fermi level in the top surface state. More rigorous cleaning techniques can be performed that removes the doping caused by surface contamination, which would move the Fermi level into the flat band and potentially allow observation of correlated effects without the need of a top gate. Even further, the thinnest sample (N = 5) could be thin enough to allow a single-sided gate to move the Fermi level into the flat band and allow observation of these correlated states without the need for any complicated gating geometries or extremely rigorous cleaning. Altogether, the promise of correlated physics in a moiré-less geometry is an exciting idea that may still have many intricacies to unravel.

In total, this work represents a strong effort toward designing topological and correlated effects in 2D heterostructures and a contribution to the field as a whole.

7 Appendices

7.1 Appendix A: Repairs to the Scanning Tunneling Microscope and Attached Liquid Helium Recovery System

Majority of my latter years as a graduate student have been spent performing measurements with a low-temperature scanning tunneling microscope. This microscope is a sophisticated piece of equipment that requires regular maintenance and repairs, and much of my time has been spent resolving issues with the microscope itself. The microscope uses liquid helium to cool samples to 4K, and has an attached liquid helium recovery and liquefication system. Additionally, samples are measured in ultra-high vacuum to preserve surface quality, since STM is a surface techniques and relies on clean, high-quality surfaces for the best possible measurements. In this appendix, I'll describe some of the biggest repairs I did in order to keep this system operational. For each repair, I'll first describe how the problem was discovered, then I'll describe how we diagnosed the issue. Then I'll describe how we fixed it.

7.1.1 Steel Bellows Leak

In August of 2020, I came to refill the STM's liquid helium cryostats, which is done every two days with this system. I arrived and discovered the temperature of both the cryostat and the STM head were elevated, well above either liquid helium or liquid nitrogen temperatures. My initial assumption was that I had arrived too late to fill, and that the liquid helium had completely boiled off, however after cooling the system back down to liquid nitrogen temperature I was unable to cool down the system any further with liquid helium at an appreciable rate.

Typically when operating the STM, we leave the ion pressure gauge off, as the light produced by this causes the sample to heat slightly above base temperature and the gauge itself acts as a potential noise source during measurement. Because of this, it was not obvious that the pressure was elevated in the STM chamber. It was discovered the next day, when we opened the gate valve connecting the STM chamber and sample preparation chamber (called 'prep chamber'), and a loud hissing was heard, followed by the immediate shut down of the prep chamber ion pump (which shuts off above 1e-5 torr).

In order to prevent foreign contaminants from entering the system, I attached a roughing pump to the turbo on the prep chamber and started pumping through this large inlet. With the gate valve closed, I was able to achieve

a pressure around 1e-8 Torr, which is the minimum expected for this style of pump. However, even slightly peaking the gate valve open caused a sharp increase in pressure that was difficult for the turbo pump to pump out. This was a consistent behavior, and no amount of peaking the gate valve open allowed us to pump out the full volume in the STM chamber. We found that slightly quickly peaking open and shutting the gate valve allowed us to slowly pump out the volume within the STM chamber, but this gas was quickly replaced through the leak.

When troubleshooting gas leaks in UHV systems, the first step is to figure out what kind of leak is present. There are two types: real leaks, which are leaks caused by a break in the vacuum walls or joints that cause outside air to leak into the chamber, and virtual leaks, which are leaks caused by a gas source from within the vacuum chamber (such as air trapped in the windings of a screw) that doesn't involve a break in the chamber walls or joints. Because the leak was a sustained source of high pressure air, and because the issue occurred overnight with no discernable changes to the STM chamber in the meantime, we assumed the leak is a real leak and not a virtual leak. In order to locate the leak, we utilized a residual gas analysis (RGA) system attached to the prep chamber. This technique can analyze the gas composition in a vacuum system by ionizing nearby gas species, accelerating them through a large electric field and deflecting them with a magnetic field. The radius of the arc of this deflection is proportional to the mass of the gas species, and a mass spectrum of the gas within the chamber can be determined. It should be noted that this process only works at pressures $<$ 1e-4 torr, so pumping via our turbo pumps is required when running the RGA. When leak checking a high-vacuum system, helium is typically used because it is an inert gas that won't interact with any part of the system, and because its small atomic size means it can easily enter any real leaks. Helium can be introduced outside of the chamber, and if it is introduced near a leak then it will be detected internally by the RGA.

This problem is a bit complicated in our system by our inability to hold open the gate valve, due to the excessive pressure within the STM chamber that would cause damage to our turbo pumps. This means we do not have an instantaneous reading of the helium level in the system, because we have to first flood with helium and then peak open the gate valve to allow the STM chamber air into the prep chamber. Because of this, our leak-checking procedure went as follows: first we introduce helium around an external portion of the STM chamber by creating a "balloon" around the area of interest. This balloon is sealed at the edges, so helium is only present around one external part of the STM and is absent at all others. Then after letting the gas diffuse into the

leak, we peak open the gate valve and see if helium is detected by the RGA. If it is, then the leak is located within the helium balloon we created, and if not, then it must be located outside the helium balloon. This can be repeated with subsequently smaller balloons until the leak is located with precision.

We started by flooding helium around the entire system, without using any balloon. We then peaked open the gate valve and recorded a mass spectrum with the RGA. There was a large peak around Mass = 4 amu, indicating the presence of helium in the chamber, and that we were correct to assume this was a real leak and not a virtual leak. At this point, the STM chamber is now flooded with Helium gas, so before continuing to isolate the leak it must be removed. To achieve this, we alternate peaking open the gate valve and shutting it in order to safely pump out the full volume of gas within STM chamber and remove any excess helium remaining. Once no more helium gas was detected by the RGA, we created our first helium balloon around the upper portion of the cryostat, shown in figure 7.1. This was constructed using a trash bag and masking tape, the most sophisticated leak-testing tools available to graduate students. We then flooded this balloon with helium, waited for the helium to diffuse through the leak, then peaked open the gate valve to test for the presence of helium. With the balloon shown in 7.1a, helium was detected, indicating the leak is within the confines of the balloon. This was repeated for subsequently smaller bags, until we reached the one shown in 7.1b, indicating

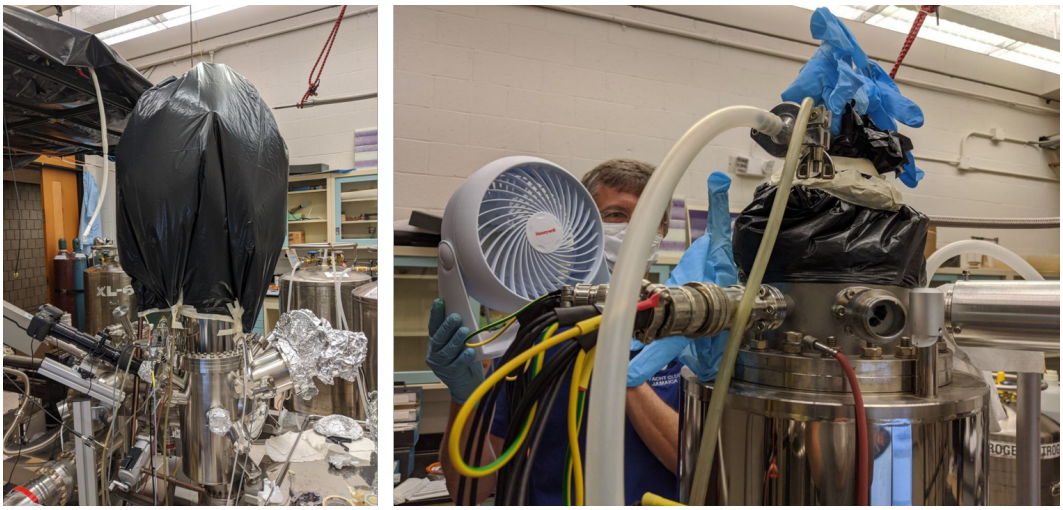

Figure 7.1: **a)** Large bag placed over the cryostat, which was filled with helium to identify the leak. **b)** smaller bag placed over a different region to further locate the actual location of the leak.

the real leak was located on the steel bellows at the top of the cryostat.

With the location of the real leak detected, we are left with two questions: how did the leak form, and how do we fix it? I'll start by answering the first question. The location of the leak was more precisely located by measuring a mass spectrum while the gate valve is barely peaked open, to give the closest thing to an instantaneous gas reading we could achieve. This was performed while directing the flow of helium gas perpendicular to the walls of the steel bellows, and the largest spike in helium gas was detected when the gas was directed just behind the inlet of the outer LN2 cryostat, on the side wall of the steel bellows themselves (specifically, between the 2nd and 3rd fold of the bellows). This location is shown in figure 7.2a, with a close-up in 7.2b showing a slight rust-colored degradation. These bellows are steel, and the

Figure 7.2: **a)** The steel bellows where the leak occurred. This picture was taken recently after filling the inner cryostat, so a layer of frost is visible over most of the upper portion of the cryostat. A close-up of the bellows is shown in **b)**, where some rust-colored degradation is visible. Notice the inlet to the LN2 cryostat is just in front of the location of the degradation. **c)** UHV sealant that was used to close up the leak.

bellows are welded to the steel side walls above and below them, meaning there is no joint in the system through which this leak is occurring. The leak is a result of corrosion through the steel bellows themselves, corroborated by the rusty discoloration of the steel here. How this corrosion occurred is only speculation, but its location behind the LN2 cryostat inlet is likely not a coincidence. When refilling the inner and outer cryostats with liquid helium and liquid nitrogen respectively, the entire top portion of the cryostat frosts over, including the steel bellows. A picture of this frost is shown in figure 7.2, which was coincidentally taken about 30 minutes after filling the cryostat (meaning it had actually thawed slightly). When filling the LN2 cryostat, the line connecting the dewar to the inlet completely freezes over, so a heat gun is used to thaw the inlet to allow removal of the line faster than letting it thaw naturally. This heat gun, when handled by someone of average height pointing at the LN2 inlet, would coincidentally heat the steel bellows directly behind it. Thus the steel bellows experience rapid thermal stress in the form of cryogenic temperatures immediately followed by temperatures significantly higher than room temperature. This regular temperature cycling likely caused an accelerated degradation of the steel here, and opened up a leak through the steel.

The solution to prevent further corrosion of the steel is simple: **we no longer use the heat gun to thaw the liquid nitrogen line after filling the outer cryostat**. While the decrease in temperature due to adding cryogens to the system is unavoidable, the rapid heating caused by the heat gun is definitely avoidable. Instead, we now wait for the LN2 line to thaw naturally, which occurs over the course of about 10 minutes. This does not add significant time to the filling procedure, as the lenghthiest portion of the filling procedure is adding liquid helium to the inner cryostat.

The next question is how do we fix it? Ideally, a fix would involve taking apart the top portion of the STM, removing the corroded bellows, then replacing them by welding new bellows in place. The STM has complicated wiring surrounding these bellows (which is partially visible in figure 7.2a), and all wiring is taut inside the UHV chamber, so that it does not contact the interior walls and provide a pathway for both thermalization and vibrational noise to reach the STM head. Thus a technician from CreaTec, the company who designed and constructed this STM, would need to be present for this procedure. Additionally after talking with CreaTec, they recommended shipping the entire cryostat to their office in Berlin, Germany, which is a lengthy procedure. All of this took place during the COVID-19 pandemic, so any travel that would be required by a technician to help package the cryostat would require a two-week quarantine both on arrival in the US and on arrival in German

on both shipping the cryostat to Berlin and on receiving in back in the US, meaning two months of waiting just for the technician to quarantine before helping. This does not factor in the time needed to ship the cryostat, or the time needed for repair. Likely, this entire procedure would take at minimum four months (likely longer), and would carry expensive shipping and repair costs as well. As a graduate student looking to finish his PhD in less than a year, this was not an appealing situation.

Instead, I looked for quicker solutions. If the steel bellows were going to be replaced anyways, I was free to do whatever I wanted to them to try and fix the leak. To this end, I found a can of CELVASEAL High Vacuum Leak Sealant (figure 7.2c), which is used to seal leaks of exactly our nature. Using this sealant involves spraying it on the location of the UHV leak and annealing at 260°C for 5 minutes. After a few iterations of this procedure, the leak should be sealed. With our leak, a couple obstacles are posed. First, the leak is in the folds of the steel bellows, which makes it difficult to reach with the spray. To solve this, sprayed the sealant into the fold with a low angle of incidence, then slipped a razor blade between the folds and gently rocked it along the location of the leak to ensure the sealant filled the leak. The second obstacle is annealing. Since the leak is located in a tight location of the STM, it is difficult to get any heating equipment to the bellows to anneal the sealant. Additionally, many parts of the STM cannot survive temperatures above 150°C, meaning annealing at the 260°C needed would destroy them. This was solved by using a heating tape with approximately 1" width, and wrapping it around the bellows themselves. This locally heats the bellows to the correct temperature without heating the temperature-sensitive portions of the STM. At the end of this section, I will include a procedure for sealing this leak, as it may need to be repeated in the future.

After repeating this process 5-6 times, and checking the helium leak level between each use of the sealant, I found that the leak fully sealed beyond the detection limit of the RGA. I was able to pump out both the STM and Prep chambers using the turbo pump to a pressure 1e-8 torr, and after a subsequent bakeout of the STM, I achieved a base pressure of 7.3e-11 torr in the STM chamber. Thus the sealing procedure worked well!

It should be noted that baking the STM (which is a common procedure in UHV systems used to achieve a low base pressure after exposure to ambient conditions) can open the leak again. **It is important to re-test the leak using the RGA every time a bakeout is performed.**

Procedure for using CELVASEAL UHV Sealant

1. Set up the RGA. This is detailed in the RGA manual. Ensure the prep

chamber pressure is below 1e-4 torr before running a mass spectrum.

2. Perform a leak check of the bellows. Using a helium cylinder, flood the exterior of the bellows with helium and measure a mass spectrum to see if a leak has opened. If helium is not detected, you can stop now. Otherwise, continue.

3. The leak is located between the 2nd and 3rd folds of the bellows. There is a possibility of residual UHV sealant left behind from a previous seal. Use a razor blade cleaned with isopropyl alcohol and remove any external residue by scraping it off. The goal is to create an open pathway for the sealant to reach the deepest portion of the fold in the bellows.

4. Shake the sealant can, then direct the nozzle between the 2nd and 3rd fold. Spray until it foams out of the crease. It should be a white color.

5. Using a razor blade cleaned with IPA, gently slip it between the folds of the bellows and rock it back and forth. This pushes the sealant into the leak. The pressure of the STM chamber may become heavily unstable during this procedure due to mechanical adjustment of the leak with the razor blade; this is expected behavior.

6. Repeat step 5 two to three times, until you are sure the sealant has reached the leak.

7. The heating tape is a white braided strip with half of a male wall outlet plug on either side, located in a drawer labeled heating tape. Wrap the heating tape around the bellows, making sure it goes inside of the screws so that it wraps tightly around the bellows themselves. Wrap it 2-3 times so that the entirety of the bellows is covered by the tape.

8. Drape the tape so that the braided portion touches nothing but the bellows themselves. The braided portion heats to 260°C, so it will be hot when you are done. The bakeout frame is very convenient for this.

9. Use a thermocouple to monitor the temperature. Slip the thermocouple between two of the folds of the heating tape, as close to the leak as possible.

10. Connect both ends of the heating tape together so they form a complete male wall plug, and plug in the heating tape.

11. Wait five minutes.

12. Unplug the heating tape and let it cool. Keep monitoring the temperature and only touch it when it is at a safe temperature.

13. Remove the tape from the bellows and repeat the leak-checking procedure in step 2. If a leak remains, repeat steps 3-13 until a leak no longer remains.

Note that a bakeout does not need to be repeated if a leak is detected.

7.1.2 Annealing Wire Break

When loading a sample for measurement, the final step before loading it into the STM itself is a 250°C anneal in the prep chamber, to remove surface contaminants and ensure the cleanest possible surface for measurement. To achieve this, a filament is located underneath the sample slot on the manipulator, which can be used to heat the sample plate and thus the surface of the sample by passing a small current through the filament. A picture of the end of the manipulator and a close up of the heating filament is shown in figure 7.3.

At the end of 2020, I was loading a sample into the STM and noticed that attempting to pass a current through the filament, the power supply immediately supplied its maximum possible voltage, indicating it could not pass any current through the filament. Using a multimeter, I found no electrical continuity through either external pin connecting to the sample heater. This

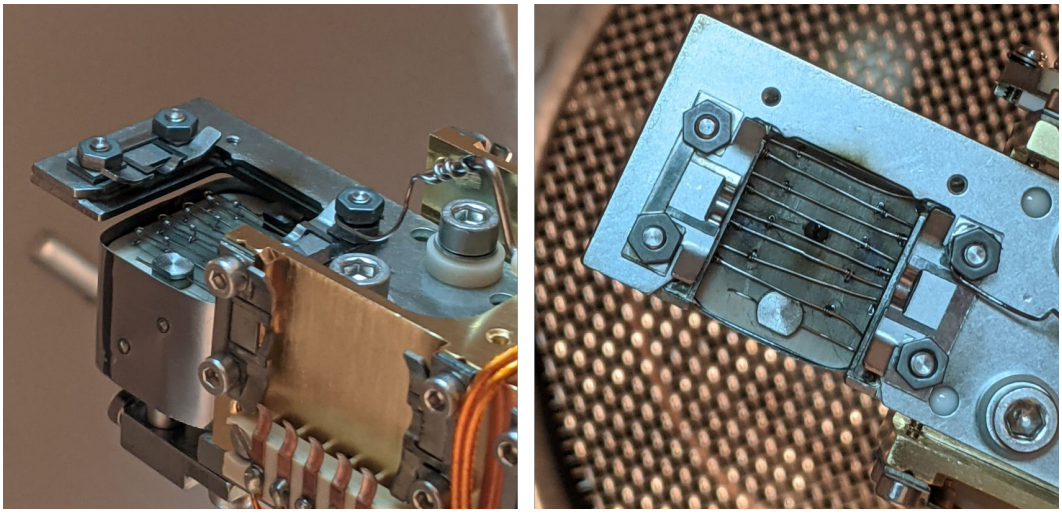

Figure 7.3: **a)** The manipulator itself. **b)** a close-up of the sample heater

indicates that either a break in the filament or a break in the wires leading up to the filament had occurred, both of which are located in the UHV chamber

Diagnosing the issue is easy in ambient conditions with a multimeter, however it is complicated by the fact that this is entirely located in a UHV chamber. I discovered that by wrapping a piece of aluminum foil around the arm of the load lock chamber, I could electrically contact the end of the rod used to transfer samples in and out of the prep chamber (henceforth "transfer rod"), and could use the transfer rod itself as an multimeter lead that can extend into the UHV chamber. A diagram of my setup is shown in figure 7.4a, where one lead of the multimeter is attached to the foil on the load lock while the other end is connected to the sample heater leads.

In order to test the continuity, I touched the transfer rod to multiple different portions of the electrical lines connecting to the filament. Some of these were difficult to reach using just the transfer rod, so I attached a stainless steel sample plate to the end of the transfer rod and used it as a fine extension of the UHV multimeter lead, with images of it touching specific portions of the electrical lines shown in figure 7.4b and c. I found that there was electrical

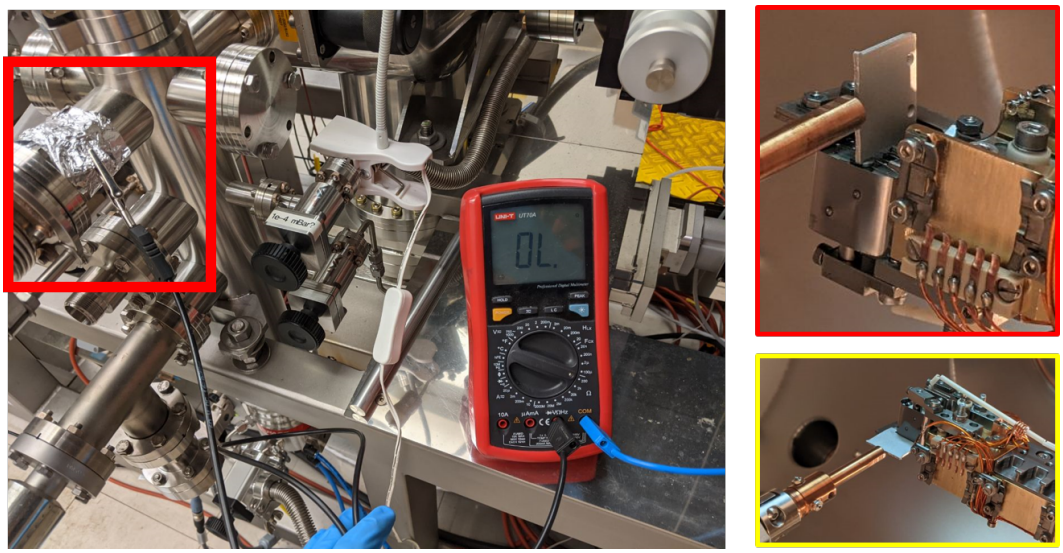

Figure 7.4: **a)** The multimeter set-up used to test electrical continuity within the UHV chamber. In the red square is a piece of tin foil wrapped around the outside of the load-lock chamber. I found this set-up was electrically continuous with whatever was attached to the transfer rod. **b-c)** Two images of using a sample plate attached to the end of the transfer rod to probe electrical continuity at places on the manipulator that are difficult to reach.

continuity through all lines leading up to the filament, indicating the break was in the filament itself.

In order to further locate the position of the break in the filament, I used an even finer probe constructed using an STM tip holder. A lengthy piece of tungsten wire (the predecessor to STM tips used in all measurements) was inserted into a tip holder, and the tip holder was placed in the tip caddy, shown in figure 7.5a. This tungsten wire can be used as a gently fine probe to locate the exact location of the break in the tungsten wire, as shown in figure 7.5b. Using this probe, I discovered the exact location of the break, shown in

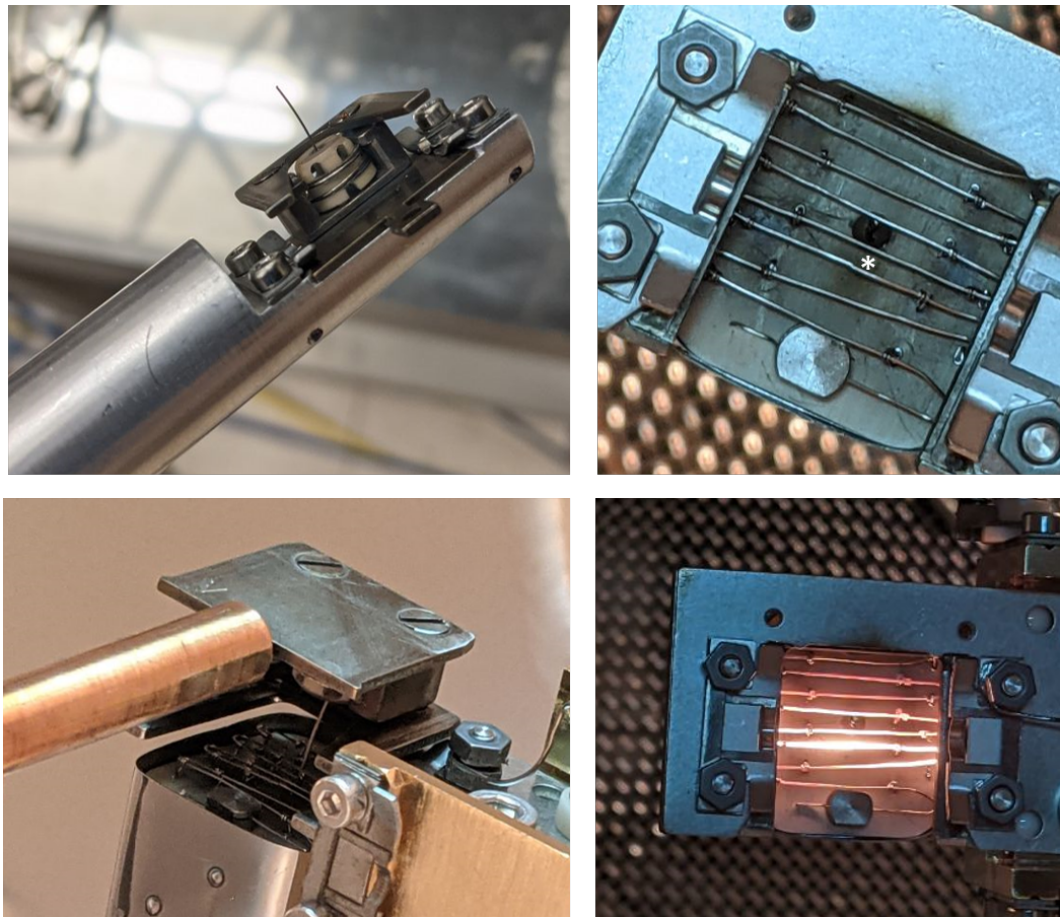

Figure 7.5: **a)** An extra-long piece of tungsten wire was placed inside a tip holder, and this could be used to move around the filament of the sample heater. **b)** Example image of using the long tungsten wire. **c)** The sample heater with the location of the break marked with a white asterisk. **d)** The sample heater while flowing a current, showing the break has been fixed.

figure 7.5c with a white asterisk. The slightest discontinuity is visible with the naked eye.

To fix the issue, I used the tungsten wire to gently push the two pieces of the filament together, so that they electrically contacted one another. Then I passed a large current through the wire using the heater leads at the end of the manipulator, effectively welding the filament back together inside the UHV chamber. A picture of this process is shown in figure 7.5d. A current of 4A was maintained for 10 minutes. The tungsten wire was not touching the filament while this current was applied. After this, the filament has worked properly for nine months. It is possible that a break may occur again in the future, and this procedure will need to be repeated.

The reason for the break is currently unknown. I see two possible causes. First is that when inserting or removing a sample, a slight accidental rotation occurred and the sample plate contacted the filament, causing the break. This can be avoided by carefully inserting the sample plate into the slot on the manipulator to ensure it does not contact the filament. The second possible cause is that an STM tip that was too long was inserted into the manipulator. When inserting STM tips, they are initially inserted upside down, so that they can be rapidly heated with an electron beam that removes any oxide layer that formed from them being created in ambient conditions. If an STM tip is too long, it will necessarily drag across the filament and potentially cause a break. To avoid this, follow the tip making procedure exactly, and be very careful to ensure the tip does not exceed the length requirements. The tip making procedure requires the precursor tungsten wire does not exceed 1.9/10 inches in length, and subsequent etching steps remove portions of the wire relative to the end of the wire. Following these instructions will ensure a tip is not too long and will not cause this issue in the future.

7.1.3 STM Clamp Repair

In December of 2020, we intentionally let the STM warm up to room temperature. The combination of winter holidays and the COVID-19 pandemic meant nobody could come in to fill the inner cryostat. Upon returning to the lab in January, we attempted to cool down the STM to liquid helium temperatures, but found the process took much longer than usual: the process usually takes less than a day but after two days of cooling, it was not nearly at base temperature.

The STM head is suspended from springs during measurement in order to better dampen mechanical vibrations and improve measurement. When not measuring, the STM can be clamped to the base plate below it, which

allows the user to change samples and tips without causing massive oscillations in the STM head. Additionally, it gives the STM head better thermal contact to the cryostat and increases the speed of cool down. When investigating the clamping mechanism, it was discovered that when moving between the clamped and unclamped positions, no motion of the STM head occurred, indicating the STM was stuck in the floating position. This poses a major problem for measurement, as samples and tips could no longer be changed.

I'll quickly described the clamping mechanism itself before discussing how it was fixed. At the base of the STM there is a T-shaped hook that is used to control motion of the STM head. This hook fits into a T-shaped slot positioned just below it, rotated 90° after insertion to prevent it from slipping out. When the T-slot is pulled downwards, it pulls the STM head with it and clamps it to the base plate. When released, the STM floats and the T-piece does not contact the T-slot, so no vibrational noise is introduced. The T-slot moves via a wire/pulley system connected to a lever on the outside of the STM. All of this is shown in figure 7.6.

We hypothesized that the issue was either that the T-piece had slipped

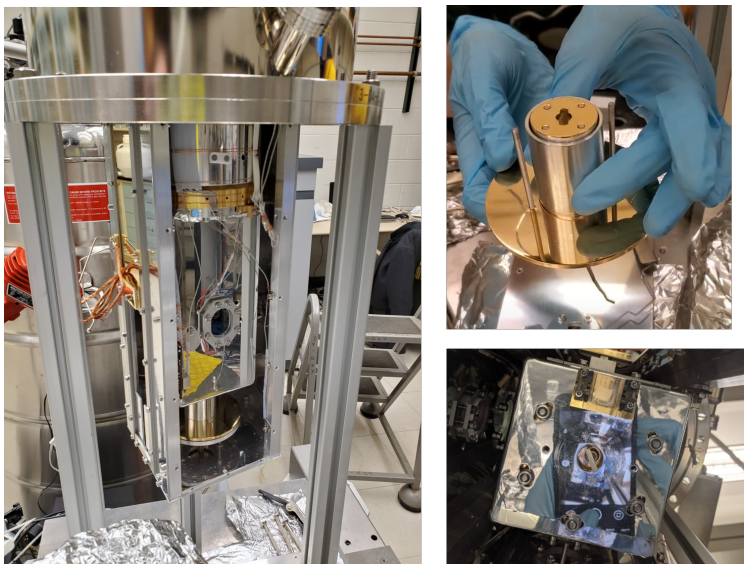

Figure 7.6: **a)** The STM head with the side-plate of the LN2 shield removed. The T-slot is located at the bottom of this.**b)** The "T-slot", which, when floating, encases the T-piece without touching it and thus increasing vibrational noise. When clamped, the central golden plate pulls downwards, pulling the T-piece and the STM head with it. **c)** The T-piece on the base of the STM head, which is used to pull the STM head to the base plate and clamp it.

out of the T-slot, or that there was a break in the wire connecting to the T-slot. Investigating either of these requires venting the UHV system and taking apart the STM itself. We vented the STM to ambient pressure using nitrogen through the load lock chamber inlet. Using a crane that was provided by CreaTec when the STM was installed, we lifted the cryostat and STM head out of the STM chamber, and set it on a tripod to diagnose the issue. Images of this process are shown in figure 7.7

After taking apart the LN2 shield surround the STM head, we discovered that the T-piece had slipped out of the T-slot. Additionally, it was improperly installed: the 90° rotation had never been performed, and only a slight mis-rotation of the T-slot by ∼10° was all that was holding the STM in the clamped position. Before reinserting the T-piece, we correctly rotated the T-slot by 90°, then reinserted the T-piece and thoroughly tested the STM clamping mechanism. We then put the STM back together, and performed a bakeout. It should be noted that the steel bellows leak previously mentioned re-opened after the bakeout, and had to be resealed using the procedure described above.

Subsequent attempts to cool down occurred in a timely manner, meaning the fix had worked.

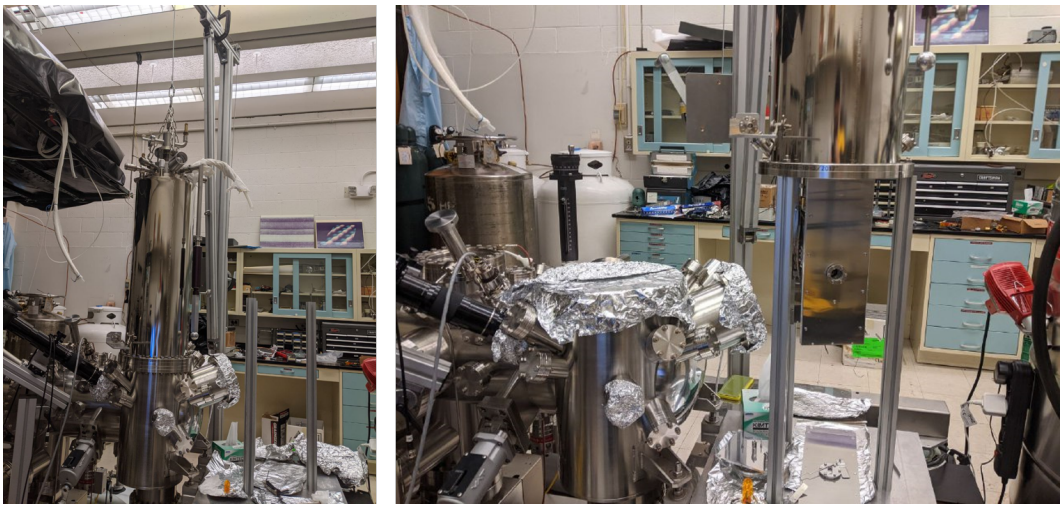

Figure 7.7: **a)** The cryostat and STM head with the crane attached, ready to lift. **b)** The cryostat and STM head removed from the STM chamber, and place on a tripod.

7.1.4 Water Chiller Clog

The helium liquefier requires a flow of chilled water to operate. To achieve this, a water chiller exists in the chase behind the STM lab. This chiller takes output water from the liquefier, cools it down like a refrigerator, and resupplies it to the liquefier inlet. To achieve this, it needs a steady flow of water itself, which is supplied by the building water lines. These building water lines are very dirty. While we have filtration systems in place to clean the building water, often they are not enough to completely clean these lines. The water chiller occasionally clogs itself, and can no longer cool down water for the liquefier.

This issue presents as an error in the liquefier, reading "HIGH OIL TEMP". If this occurs, first swap the filter located in the chase with a fresh clean one, as described in the manual written by Dacen Waters. However if this does not resolve the issue, follow the following procedure (best with two people):

1. Turn off the incoming and outgoing building water supplies in the chase simultaneously. Do this slowly.

2. Vent the pressure in the lines using the red button at the top of the filter casing.

3. The hose connecting the incoming building water to the inlet of the water chiller is the "incoming hose", and the same for the outgoing water is the "outgoing hose". Remove these hoses from the incoming and outgoing building water supplies, located just below the valves that shut them off. Remember which is which. For the incoming water hose, it is best to keep the filter attached and remove the hose after the filtration system.

4. Attach the outgoing hose to the incoming building water outlet, at the end of the filtration system.

5. Put the incoming water hose end in the sink located just inside the lab.

6. There is a large tub on the shelf above the sink. It is advised to place this over the sink to avoid splashing.

7. Slowly turn on the incoming building water line. This should flow water backwards through the water chiller.

8. Brown water should come out of the hose in the sink. If it does not, further open the incoming water line.

9. It is likely the sink will fill up a few times during this procedure. If this occurs, turn off the incoming building water, let the sink drain, then resume.

10. When the water coming out of the hose runs clear, turn off the incoming building water supply.

11. Return the outgoing hose to the outgoing building water inlet. Return the incoming hose to the incoming water outlet.

12. Slowly turn on the incoming and outgoing water supplies simultaneously.

13. Flush the water chiller by pressing the black button at the base of the chiller.

7.2 Appendix B: Gating in a Scanning Tunneling Microscope

Many devices in this thesis were constructed with the intent to use the p-doped silicon substrate as a gate, by creating a capacitive effect across the 300nm SiO_2 layer and inducing a change in charge density in a 2D heterostructure. In rhombohedral graphite stacks of N = 9 and N = 14 this was the case, and several experiments were performed by tuning the gate voltage applied to the silicon chip and measuring tunneling spectra at different gates. In these samples, the doped silicon chip was attached to a tantalum STM sample plate with a conducting epoxy, and the back gate bias was applied to the entire tantalum plate.

It became apparent that the gate voltage applied did not affect tunneling spectra in any appreciable way. Tunneling spectra from a wide range of gate voltages did not have any appreciable differences. While this could be the result of strong interlayer screening in RG [104], this caused us to question whether the gate voltage was being properly applied at all.

In order to test this, I created a transport device that could be measured both in ambient conditions outside of the STM and inside the STM. The device consisted of a piece of graphite approximately three layers thick that I transferred onto pre-patterned gold leads in a Hall bar geometry. I used PPC as the transfer polymer, and included a piece of hBN to pick up the graphite using their van der Waals interaction. PPC does not bind to graphite, so the hBN layer is crucial for transfer success. A schematic of the device structure is shown in figure 7.8a, and an optical image of the device is shown in figure 7.8b. The device was then mounted onto an STM sample plate using the

same conducting epoxy, and subsequently wire-bonded. The STM only has four pins, so only four of the six Hall bar leads were used. In figure 7.8b, the un-bonded pins are labeled "NB" in red.

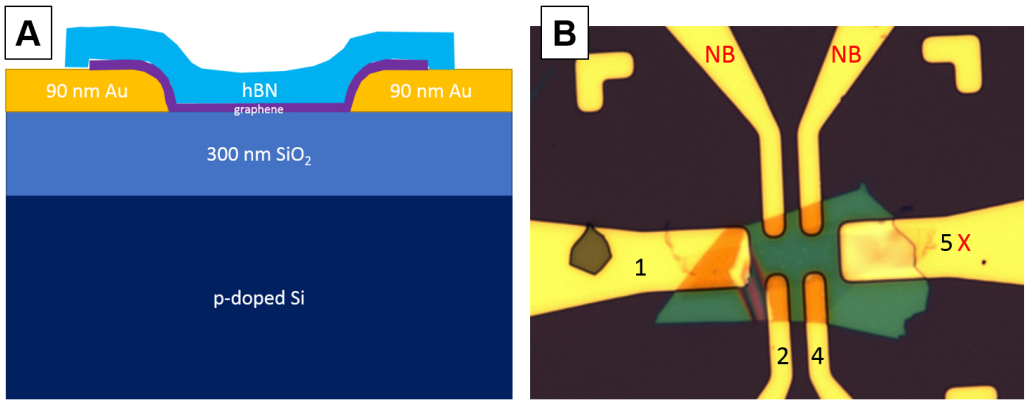

Figure 7.8: **a)** A schematic of the device geometry used to test gating in the STM. **b)** A 100x image of the finished device. Pins labeled with numbers were used in the measurement, pins labeled "NB" were not bonded. Pin 5 did not work at low temperatures.

The device was then tested in room temperature. We do not have an STM-style sample holder outside of the STM that would easily allow us to supply bias voltages necessary for transport measurements, so a probe station was used instead. In order to test our ability to gate, a two-terminal voltage-biased measurement scheme was used. A 5 mV DC bias voltage was supplied through an 11.8 kΩ line resistance to one probe while the other was grounded. The probes were then moved onto the sample pins, and the current through the graphite device was recorded for several gate voltages. A plot of the two-terminal resistance is shown in figure 7.9a. The device displays a resistance peak centered around $V_g = 18$ V. All resistance values exceed 12.8 kΩ. This is expected due to our two-terminal geometry. This device geometry measures all contact resistances and line resistances in series with the device resistance. Both contact resistances are on the order of 500 Ω, and together with the 11.8 kΩ line resistance, a total extraneous resistance of 12.8 kΩ exists on top of all measurements. Thus the true value of the resistance peak, which is found by subtracting this extraneous resistance from the total resistance, is approximately 950 Ω, which is similar to what one would expect for room temperature graphite transport [13]. The leakage current, defined as the current supplied by the gate voltage power supply, is shown in figure 7.9b. This should be

zero when the gate dielectric is an ideal insulator, however in practice, it is a small non-zero value that increases with gate voltage, and should be larger at higher temperatures due to the broadening of the Fermi-Dirac distribution. In an abundance of caution, measurement was halted when the leakage current exceed $1/1000^{th}$ of the device current.

The sample was then loaded into the STM, where the pins that are usually used to make contact to the tunnel drain were instead used for transport. We measured low temperature transport in this device in an identical gating geometry as exists in STM measurements, where the sample bias is added on top of the gate voltage to ensure ΔV across the capacitor is constant. The resulting device resistance, measured with identical bias voltage and line resistance as in the ambient conditions, is shown in figure 7.9c. We see a

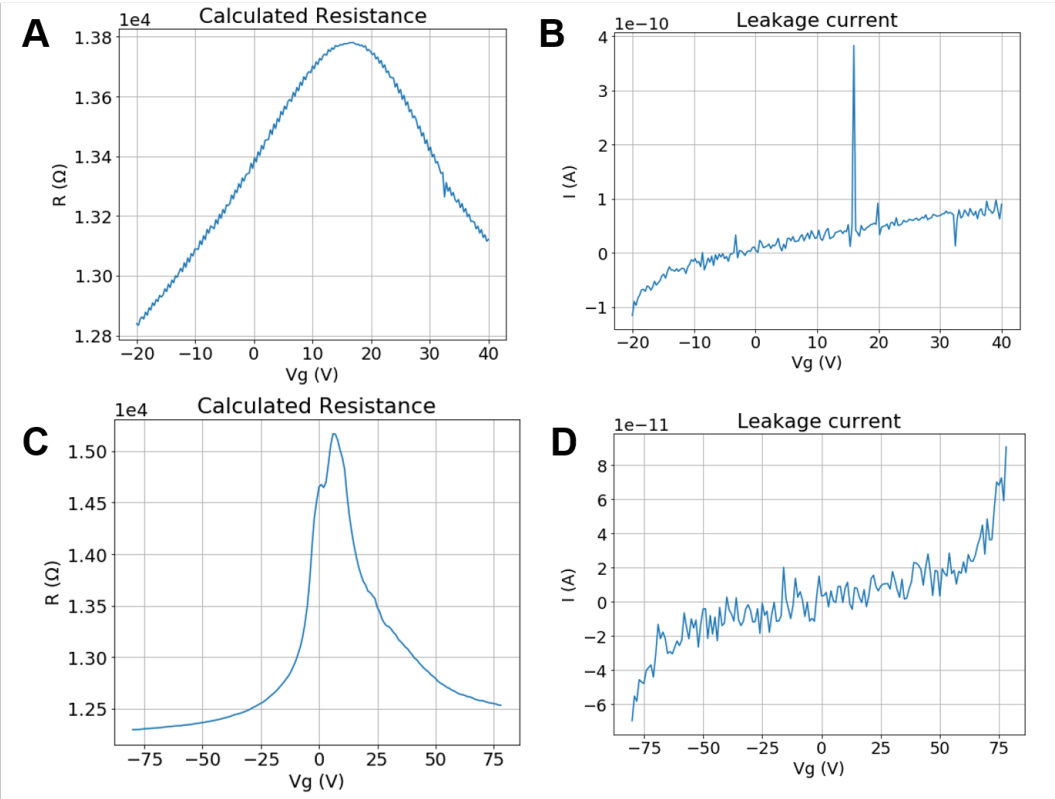

Figure 7.9: **a)** Room-temperature two-terminal resistance vs. gate voltage. **b)** Room-temperature leakage current through the SiO_2 vs. gate voltage. **c)** Low-temperature two-terminal resistance vs. gate voltage. **d)** Low-temperature leakage current through the SiO_2.

modulation of the device resistance from 12.5 kΩ to over 15 kΩ through the gate range tested. The contact resistances, which are generally not the same at room temperature and low temperature, were approximately 200 Ω at T = 4K in the STM. Thus the total extraneous resistance was 12.2 kΩ, resulting in a device resistance modulation from 100 Ω to 3 kΩ. The resistance peak occurs at an identical location as in the room temperature case, but the line shape displays a sharper profile with a taller peak (note the change in gate voltage axis). This is comparable to that seen in graphite transport in literature [13]. The leakage current is plotted in figure 7.9d, and is approximately an order of magnitude less than that seen in the room temperature case. This is expected due to the reduced broadening of the Fermi-Dirac distribution at T = 4K. At the minimum/maximum gate voltages tested, the beginning of an exponential increase is observed. In fact, gate voltages beyond this caused a large increase in leakage current, exceeding 1 nA leakage at V_g = + 78 V. Afterwards, the device displayed no change in resistance as gate voltage was varied, indicating dielectric breakdown of the SiO_2 had occurred and caused irreversible device damage.

The above confirms that the gating geometry in the STM was working as intended. The applied gate voltage to the entire tantalum plate altered graphite resistance in a predictable manner that was consistent with both previously reported literature on transport in few-layer graphite and room temperature measurements of the same device. This indicates that the lack of observable changes in RG tunneling spectra as gate voltage is varied is due to the strong interlayer screening effect.

References

[1] Jan H de Boer and Evert JW Verwey. Semi-conductors with partially and with completely filled 3d-lattice bands. *Proceedings of the Physical Society (1926-1948)*, 49(4S):59, 1937.

[2] Stephen John Blundell. *Magnetism in condensed matter*. Oxford University Press, 2014.

[3] K v Klitzing, Gerhard Dorda, and Michael Pepper. New method for high-accuracy determination of the fine-structure constant based on quantized hall resistance. *Physical Review Letters*, 45(6):494, 1980.

[4] Richard E Prange and Steven M Girvin. The quantum hall effect, graduate texts in contemporary physics, 1987.

[5] Matthew Yankowitz, Shaowen Chen, Hryhoriy Polshyn, Yuxuan Zhang, K Watanabe, T Taniguchi, David Graf, Andrea F Young, and Cory R Dean. Tuning superconductivity in twisted bilayer graphene. *Science*, 363(6431):1059–1064, 2019.

[6] Yuan Cao, Valla Fatemi, Shiang Fang, Kenji Watanabe, Takashi Taniguchi, Efthimios Kaxiras, and Pablo Jarillo-Herrero. Unconventional superconductivity in magic-angle graphene superlattices. *Nature*, 556(7699):43–50, 2018.

[7] M Serlin, CL Tschirhart, H Polshyn, Y Zhang, J Zhu, K Watanabe, T Taniguchi, L Balents, and AF Young. Intrinsic quantized anomalous hall effect in a moiré heterostructure. *Science*, 367(6480):900–903, 2020.

[8] Aaron L Sharpe, Eli J Fox, Arthur W Barnard, Joe Finney, Kenji Watanabe, Takashi Taniguchi, MA Kastner, and David Goldhaber-Gordon. Emergent ferromagnetism near three-quarters filling in twisted bilayer graphene. *Science*, 365(6453):605–608, 2019.

[9] Lei Wang, En-Min Shih, Augusto Ghiotto, Lede Xian, Daniel A Rhodes, Cheng Tan, Martin Claassen, Dante M Kennes, Yusong Bai, Bumho Kim, et al. Correlated electronic phases in twisted bilayer transition metal dichalcogenides. *Nature materials*, 19(8):861–866, 2020.

[10] Guorui Chen, Lili Jiang, Shuang Wu, Bosai Lyu, Hongyuan Li, Bheema Lingam Chittari, Kenji Watanabe, Takashi Taniguchi, Zhiwen Shi, Jeil Jung, et al. Evidence of a gate-tunable mott insulator in a trilayer graphene moiré superlattice. *Nature Physics*, 15(3):237–241, 2019.

[11] Guorui Chen, Aaron L Sharpe, Eli J Fox, Ya-Hui Zhang, Shaoxin Wang, Lili Jiang, Bosai Lyu, Hongyuan Li, Kenji Watanabe, Takashi Taniguchi, et al. Tunable correlated chern insulator and ferromagnetism in a moiré superlattice. *Nature*, 579(7797):56–61, 2020.

[12] Emma C Regan, Danqing Wang, Chenhao Jin, M Iqbal Bakti Utama, Beini Gao, Xin Wei, Sihan Zhao, Wenyu Zhao, Zuocheng Zhang, Kentaro Yumigeta, et al. Mott and generalized wigner crystal states in wse 2/ws 2 moiré superlattices. *Nature*, 579(7799):359–363, 2020.

[13] K. S. Novoselov, A. K. Geim, S. V. Morozov, D. Jiang, Y. Zhang, S. V. Dubonos, I. V. Grigorieva, and A. A. Firsov. Electric field effect in atomically thin carbon films. *Science*, 306(5696):666–669, 2004.

[14] Xiaoxiang Xi, Zefang Wang, Weiwei Zhao, Ju-Hyun Park, Kam Tuen Law, Helmuth Berger, László Forró, Jie Shan, and Kin Fai Mak. Ising pairing in superconducting nbse2 atomic layers. *Nature Physics*, 12(2):139–143, Nov 2015.

[15] Efrén Navarro-Moratalla, Joshua O. Island, Samuel Mañas-Valero, Elena Pinilla-Cienfuegos, Andres Castellanos-Gomez, Jorge Quereda, Gabino Rubio-Bollinger, Luca Chirolli, Jose Angel Silva-Guillén, Nicolás Agraït, Gary A. Steele, Francisco Guinea, Herre S. J. van der Zant, and Eugenio Coronado. Enhanced superconductivity in atomically thin tas2. *Nature Communications*, 7:11043–, Mar 2016.

[16] Bevin Huang, Genevieve Clark, Efren Navarro-Moratalla, Dahlia R Klein, Ran Cheng, Kyle L Seyler, Ding Zhong, Emma Schmidgall, Michael A McGuire, David H Cobden, et al. Layer-dependent ferromagnetism in a van der waals crystal down to the monolayer limit. *Nature*, 546(7657):270–273, 2017.

[17] Ming-Wei Lin, Houlong L Zhuang, Jiaqiang Yan, Thomas Zac Ward, Alexander A Puretzky, Christopher M Rouleau, Zheng Gai, Liangbo Liang, Vincent Meunier, Bobby G Sumpter, et al. Ultrathin nanosheets of crsite 3: a semiconducting two-dimensional ferromagnetic material. *Journal of Materials Chemistry C*, 4(2):315–322, 2016.

[18] Yuanbo Zhang, Yan-Wen Tan, Horst L. Stormer, and Philip Kim. Experimental observation of the quantum hall effect and berry's phase in graphene. *Nature*, 438(7065):201–204, 2005.

[19] K. S. Novoselov, A. K. Geim, S. V. Morozov, D. Jiang, M. I. Katsnelson, I. V. Grigorieva, S. V. Dubonos, and A. A. Firsov. Two-dimensional gas of massless dirac fermions in graphene. *Nature*, 438(7065):197–200, 2005.

[20] C. R. Dean, A. F. Young, P. Cadden-Zimansky, L. Wang, H. Ren, K. Watanabe, T. Taniguchi, P. Kim, J. Hone, and K. L. Shepard. Multicomponent fractional quantum hall effect in graphene. *Nature Physics*, 7(9):693–696, 2011.

[21] Andrea F Young, Cory R Dean, Lei Wang, Hechen Ren, Paul Cadden-Zimansky, Kenji Watanabe, Takashi Taniguchi, James Hone, Kenneth L Shepard, and Philip Kim. Spin and valley quantum hall ferromagnetism in graphene. *Nature Physics*, 8(7):550–556, 2012.

[22] K. S. Novoselov, D. Jiang, F. Schedin, T. J. Booth, V. V. Khotkevich, S. V. Morozov, and A. K. Geim. Two-dimensional atomic crystals. *Proceedings of the National Academy of Sciences*, 102(30):10451–10453, 2005.

[23] Cory R Dean, Andrea F Young, Inanc Meric, Chris Lee, Lei Wang, Sebastian Sorgenfrei, Kenji Watanabe, Takashi Taniguchi, Phillip Kim, Kenneth L Shepard, et al. Boron nitride substrates for high-quality graphene electronics. *Nature nanotechnology*, 5(10):722–726, 2010.

[24] Kin Fai Mak, Changgu Lee, James Hone, Jie Shan, and Tony F Heinz. Atomically thin mos2: a new direct-gap semiconductor. *Physical review letters*, 105(13):136805, 2010.

[25] Zhaowei Zhang, Jingzhi Shang, Chongyun Jiang, Abdullah Rasmita, Weibo Gao, and Ting Yu. Direct photoluminescence probing of ferromagnetism in monolayer two-dimensional crbr3. *Nano letters*, 19(5):3138–3142, 2019.

[26] Cheng Gong, Lin Li, Zhenglu Li, Huiwen Ji, Alex Stern, Yang Xia, Ting Cao, Wei Bao, Chenzhe Wang, Yuan Wang, et al. Discovery of intrinsic ferromagnetism in two-dimensional van der waals crystals. *Nature*, 2017.

[27] Arnab Banerjee, Jiaqiang Yan, Johannes Knolle, Craig A. Bridges, Matthew B. Stone, Mark D. Lumsden, David G. Mandrus, David A. Tennant, Roderich Moessner, and Stephen E. Nagler. Neutron scattering in the proximate quantum spin liquid α-rucl3. *Science*, 356(6342):1055–1059, 2017.

[28] A. Banerjee, C. A. Bridges, J.-Q. Yan, A. A. Aczel, L. Li, M. B. Stone, G. E. Granroth, M. D. Lumsden, Y. Yiu, J. Knolle, S. Bhattacharjee, D. L. Kovrizhin, R. Moessner, D. A. Tennant, D. G. Mandrus, and S. E. Nagler. Proximate kitaev quantum spin liquid behaviour in a honeycomb magnet. *Nature Materials*, 15:733 EP –, Apr 2016. Article.

[29] Shujie Tang, Chaofan Zhang, Dillon Wong, Zahra Pedramrazi, Hsin-Zon Tsai, Chunjing Jia, Brian Moritz, Martin Claassen, Hyejin Ryu, Salman Kahn, Juan Jiang, Hao Yan, Makoto Hashimoto, Donghui Lu, Robert G. Moore, Chan-Cuk Hwang, Choongyu Hwang, Zahid Hussain, Yulin Chen, Miguel M. Ugeda, Zhi Liu, Xiaoming Xie, Thomas P. Devereaux, Michael F. Crommie, Sung-Kwan Mo, and Zhi-Xun Shen. Quantum spin hall state in monolayer 1t'-wte2. *Nature Physics*, 13:683–, Jun 2017.

[30] Andrea Young. *Quantum Transport in Graphene Heterostructures*. PhD thesis, Columbia University, 2012.

[31] S. V. Morozov, K. S. Novoselov, M. I. Katsnelson, F. Schedin, D. C. Elias, J. A. Jaszczak, and A. K. Geim. Giant intrinsic carrier mobilities in graphene and its bilayer. *Phys. Rev. Lett.*, 100:016602, Jan 2008.

[32] Xu Du, Ivan Skachko, Anthony Barker, and Eva Y. Andrei. Approaching ballistic transport in suspended graphene. *Nature Nanotechnology*, 3(8):491–495, 2008.

[33] Edward McCann and Mikito Koshino. The electronic properties of bilayer graphene. *Reports on Progress in physics*, 76(5):056503, 2013.

[34] JO Island, X Cui, C Lewandowski, JY Khoo, EM Spanton, H Zhou, D Rhodes, JC Hone, T Taniguchi, K Watanabe, et al. Spin–orbit-driven band inversion in bilayer graphene by the van der waals proximity effect. *Nature*, 571(7763):85–89, 2019.

[35] Navketan Batra and Goutam Sheet. Physics with coffee and doughnuts. *Resonance*, 25(6):765–786, 2020.

[36] Ruijuan Xiao, Ferenc Tasnadi, K Koepernik, JWF Venderbos, M Richter, and M Taut. Density functional investigation of rhombohedral stacks of graphene: Topological surface states, nonlinear dielectric response, and bulk limit. *Physical Review B*, 84(16):165404, 2011.

[37] Kenji Watanabe, Takashi Taniguchi, and Hisao Kanda. Direct-bandgap properties and evidence for ultraviolet lasing of hexagonal boron nitride single crystal. *Nature materials*, 3(6):404–409, 2004.

[38] Sajedeh Manzeli, Dmitry Ovchinnikov, Diego Pasquier, Oleg V. Yazyev, and Andras Kis. 2d transition metal dichalcogenides. *Nature Reviews Materials*, 2:17033 EP –, Jun 2017. Review Article.

[39] N. D. Mermin and H. Wagner. Absence of ferromagnetism or antiferromagnetism in one- or two-dimensional isotropic heisenberg models. *Phys. Rev. Lett.*, 17:1133–1136, Nov 1966.

[40] Wei-Bing Zhang, Qian Qu, Peng Zhu, and Chi-Hang Lam. Robust intrinsic ferromagnetism and half semiconductivity in stable two-dimensional single-layer chromium trihalides. *Journal of Materials Chemistry C*, 3(48):12457–12468, 2015.

[41] Hao Wang, Volker Eyert, and Udo Schwingenschlögl. Electronic structure and magnetic ordering of the semiconducting chromium trihalides crcl3, crbr3, and cri3. *Journal of Physics: Condensed Matter*, 23(11):116003, 2011.

[42] LD Casto, AJ Clune, MO Yokosuk, JL Musfeldt, TJ Williams, HL Zhuang, M-W Lin, K Xiao, RG Hennig, BC Sales, et al. Strong spin-lattice coupling in crsite3. *APL materials*, 3(4):041515, 2015.

[43] K. W. Plumb, J. P. Clancy, L. J. Sandilands, V. Vijay Shankar, Y. F. Hu, K. S. Burch, Hae-Young Kee, and Young-June Kim. $\alpha - \mathrm{rucl}_3$: A spin-orbit assisted mott insulator on a honeycomb lattice. *Phys. Rev. B*, 90:041112, Jul 2014.

[44] R. T. Scaletter. An introduction to the hubbard hamiltonian, 2016.

[45] Leon Balents. Spin liquids in frustrated magnets. *Nature*, 464(7286):199–208, 2010.

[46] Alexei Kitaev. Anyons in an exactly solved model and beyond. *Annals of Physics*, 321(1):2–111, 2006.

[47] Benjamin Hunt, Javier D Sanchez-Yamagishi, Andrea F Young, Matthew Yankowitz, Brian J LeRoy, Kenji Watanabe, Takashi Taniguchi, Pilkyung Moon, Mikito Koshino, Pablo Jarillo-Herrero, et al. Massive dirac fermions and hofstadter butterfly in a van der waals heterostructure. *Science*, 340(6139):1427–1430, 2013.

[48] Cory R Dean, L Wang, P Maher, C Forsythe, Fereshte Ghahari, Y Gao, Jyoti Katoch, M Ishigami, P Moon, M Koshino, et al. Hofstadter's butterfly and the fractal quantum hall effect in moiré superlattices. *Nature*, 497(7451):598–602, 2013.

[49] Felix Lüpke, Dacen Waters, C Sergio, Michael Widom, David G Mandrus, Jiaqiang Yan, Randall M Feenstra, and Benjamin M Hunt. Proximity-induced superconducting gap in the quantum spin hall edge state of monolayer wte 2. *Nature Physics*, 16(5):526–530, 2020.

[50] Lars Onsager. Crystal statistics. i. a two-dimensional model with an order-disorder transition. *Phys. Rev.*, 65:117–149, Feb 1944.

[51] Hai Li, Jumiati Wu, Xiao Huang, Gang Lu, Jian Yang, Xin Lu, Qihua Xiong, and Hua Zhang. Rapid and reliable thickness identification of two-dimensional nanosheets using optical microscopy. *ACS nano*, 7(11):10344–10353, 2013.

[52] Alper Gurarslan, Yifei Yu, Liqin Su, Yiling Yu, Francisco Suarez, Shanshan Yao, Yong Zhu, Mehmet Ozturk, Yong Zhang, and Linyou Cao. Surface-energy-assisted perfect transfer of centimeter-scale monolayer and few-layer mos2 films onto arbitrary substrates. *ACS nano*, 8(11):11522–11528, 2014.

[53] Andres Castellanos-Gomez, Michele Buscema, Rianda Molenaar, Vibhor Singh, Laurens Janssen, Herre SJ van der Zant, and Gary A Steele. Deterministic transfer of two-dimensional materials by all-dry viscoelastic stamping. *2D Materials*, 1(1):011002, 2014.

[54] Dmitry Shcherbakov, Petr Stepanov, Daniel Weber, Yaxian Wang, Jin Hu, Yanglin Zhu, Kenji Watanabe, Takashi Taniguchi, Zhiqiang Mao, Wolfgang Windl, Joshua Goldberger, Marc Bockrath, and Chun Ning Lau. Raman spectroscopy, photocatalytic degradation, and stabilization of atomically thin chromium tri-iodide. *Nano Letters*, 18(7):4214–4219, Jul 2018.

[55] AM Goossens, VE Calado, A Barreiro, K Watanabe, T Taniguchi, and LMK Vandersypen. Mechanical cleaning of graphene. *Applied Physics Letters*, 100(7):073110, 2012.

[56] L Wang, I Meric, PY Huang, Q Gao, Y Gao, H Tran, T Taniguchi, K Watanabe, LM Campos, DA Muller, et al. One-dimensional electrical contact to a two-dimensional material. *Science*, 342(6158):614–617, 2013.

[57] David J Griffiths and Darrell F Schroeter. *Introduction to quantum mechanics*. Cambridge University Press, 2018.

[58] Bert Voigtländer. *Scanning Probe Microscopy*. Springer, 2015.

[59] M Zahid Hasan and Charles L Kane. Colloquium: topological insulators. *Reviews of modern physics*, 82(4):3045, 2010.

[60] F Duncan M Haldane. Model for a quantum hall effect without landau levels: Condensed-matter realization of the" parity anomaly". *Physical review letters*, 61(18):2015, 1988.

[61] Jay D Sau, Roman M Lutchyn, Sumanta Tewari, and S Das Sarma. Generic new platform for topological quantum computation using semiconductor heterostructures. *Physical review letters*, 104(4):040502, 2010.

[62] Zhenhua Qiao, Shengyuan A Yang, Wanxiang Feng, Wang-Kong Tse, Jun Ding, Yugui Yao, Jian Wang, and Qian Niu. Quantum anomalous hall effect in graphene from rashba and exchange effects. *Physical Review B*, 82(16):161414, 2010.

[63] Wang-Kong Tse, Zhenhua Qiao, Yugui Yao, AH MacDonald, and Qian Niu. Quantum anomalous hall effect in single-layer and bilayer graphene. *Physical Review B*, 83(15):155447, 2011.

[64] Peng Wei, Sunwoo Lee, Florian Lemaitre, Lucas Pinel, Davide Cutaia, Wujoon Cha, Ferhat Katmis, Yu Zhu, Donald Heiman, James Hone, et al. Strong interfacial exchange field in the graphene/eus heterostructure. *Nature materials*, 15(7):711–716, 2016.

[65] Zhiyong Wang, Chi Tang, Raymond Sachs, Yafis Barlas, and Jing Shi. Proximity-induced ferromagnetism in graphene revealed by the anomalous hall effect. *Phys. Rev. Lett.*, 114:016603, Jan 2015.

[66] DA Abanin, SV Morozov, LA Ponomarenko, RV Gorbachev, AS Mayorov, MI Katsnelson, Kenji Watanabe, Takashi Taniguchi, KS Novoselov, LS Levitov, et al. Giant nonlocality near the dirac point in graphene. *Science*, 332(6027):328–330, 2011.

[67] Yiping Wang, Jesse Balgley, Eli Gerber, Mason Gray, Narendra Kumar, Xiaobo Lu, Jia-Qiang Yan, Arash Fereidouni, Rabindra Basnet, Seok Joon Yun, et al. Modulation doping via a two-dimensional atomic crystalline acceptor. *Nano Letters*, 20(12):8446–8452, 2020.

[68] Jiayong Zhang, Bao Zhao, Tong Zhou, Yang Xue, Chunlan Ma, and Zhongqin Yang. Strong magnetization and chern insulators in compressed graphene/cri 3 van der waals heterostructures. *Physical Review B*, 97(8):085401, 2018.

[69] Boyi Zhou, J. Balgley, P. Lampen-Kelley, J.-Q. Yan, D. G. Mandrus, and E. A. Henriksen. Evidence for charge transfer and proximate magnetism in graphene–$\alpha-rucl_3$ heterostructures. *Phys. Rev. B*, 100:165426, Oct 2019.

[70] Ö. Rapp, G. Benediktsson, H. U. Åström, S. Arajs, and K. V. Rao. Electrical resistivity of antiferromagnetic chromium near the néel temperature. *Phys. Rev. B*, 18:3665–3673, Oct 1978.

[71] Yukio Suezaki and Hazime Mori. Dynamic critical phenomena in magnetic systems. ii electrical resistivity near the néel point. *Progress of Theoretical Physics*, 41:1177–1189, May 1969.

[72] S. Alexander, J. S. Helman, and I. Balberg. Critical behavior of the electrical resistivity in magnetic systems. *Phys. Rev. B*, 13:304–315, Jan 1976.

[73] Masatoshi Imada, Atsushi Fujimori, and Yoshinori Tokura. Metal-insulator transitions. *Reviews of modern physics*, 70(4):1039, 1998.

[74] Soudabeh Mashhadi, Youngwook Kim, Jeongwoo Kim, Daniel Weber, Takashi Taniguchi, Kenji Watanabe, Noejung Park, Bettina Lotsch, Jurgen H. Smet, Marko Burghard, and Klaus Kern. Spin-split band hybridization in graphene proximitized with a-rucl3 nanosheets. *Nano Letters*, 19(7):4659–4665, Jul 2019.

[75] Young-Jun Yu, Yue Zhao, Sunmin Ryu, Louis E Brus, Kwang S Kim, and Philip Kim. Tuning the graphene work function by electric field effect. *Nano letters*, 9(10):3430–3434, 2009.

[76] I Pollini. Electronic properties of the narrow-band material α-rucl 3. *Physical Review B*, 53(19):12769, 1996.

[77] S.-H. Baek, S.-H. Do, K.-Y. Choi, Y. S. Kwon, A. U. B. Wolter, S. Nishimoto, Jeroen van den Brink, and B. Büchner. Evidence for a field-induced quantum spin liquid in α-rucl$_3$. *Phys. Rev. Lett.*, 119:037201, Jul 2017.

[78] Julien Renard, Matthias Studer, and Joshua A Folk. Origins of nonlocality near the neutrality point in graphene. *Physical review letters*, 112(11):116601, 2014.

[79] Mengqiao Sui, Guorui Chen, Liguo Ma, Wen-Yu Shan, Dai Tian, Kenji Watanabe, Takashi Taniguchi, Xiaofeng Jin, Wang Yao, Di Xiao, and Yuanbo Zhang. Gate-tunable topological valley transport in bilayer graphene. *Nature Physics*, 11:1027 EP –, Sep 2015.

[80] Xiaoxue Liu, Zhi Wang, Kenji Watanabe, Takashi Taniguchi, Oskar Vafek, and JIA Li. Tuning electron correlation in magic-angle twisted bilayer graphene using coulomb screening. *Science*, 371(6535):1261–1265, 2021.

[81] Fengcheng Wu, AH MacDonald, and Ivar Martin. Theory of phonon-mediated superconductivity in twisted bilayer graphene. *Physical review letters*, 121(25):257001, 2018.

[82] Biao Lian, Zhijun Wang, and B Andrei Bernevig. Twisted bilayer graphene: a phonon-driven superconductor. *Physical review letters*, 122(25):257002, 2019.

[83] Cenke Xu and Leon Balents. Topological superconductivity in twisted multilayer graphene. *Physical review letters*, 121(8):087001, 2018.

[84] Hiroki Isobe, Noah FQ Yuan, and Liang Fu. Unconventional superconductivity and density waves in twisted bilayer graphene. *Physical Review X*, 8(4):041041, 2018.

[85] Guorui Chen, Aaron L Sharpe, Patrick Gallagher, Ilan T Rosen, Eli J Fox, Lili Jiang, Bosai Lyu, Hongyuan Li, Kenji Watanabe, Takashi Taniguchi, et al. Signatures of tunable superconductivity in a trilayer graphene moiré superlattice. *Nature*, 572(7768):215–219, 2019.

[86] NB Kopnin, TT Heikkilä, and GE Volovik. High-temperature surface superconductivity in topological flat-band systems. *Physical Review B*, 83(22):220503, 2011.

[87] NB Kopnin, Mari Ijäs, A Harju, and TT Heikkilä. High-temperature surface superconductivity in rhombohedral graphite. *Physical Review B*, 87(14):140503, 2013.

[88] WA Muñoz, Lucian Covaci, and FM Peeters. Tight-binding description of intrinsic superconducting correlations in multilayer graphene. *Physical Review B*, 87(13):134509, 2013.

[89] Minoru Otani, Mikito Koshino, Yoshiteru Takagi, and Susumu Okada. Intrinsic magnetic moment on (0001) surfaces of rhombohedral graphite. *Physical Review B*, 81(16):161403, 2010.

[90] Betül Pamuk, Jacopo Baima, Francesco Mauri, and Matteo Calandra. Magnetic gap opening in rhombohedral-stacked multilayer graphene from first principles. *Physical Review B*, 95(7):075422, 2017.

[91] Matthew Yankowitz, Fenglin Wang, Chun Ning Lau, and Brian J LeRoy. Local spectroscopy of the electrically tunable band gap in trilayer graphene. *Physical Review B*, 87(16):165102, 2013.

[92] Wenzhong Bao, Lei Jing, Jr Velasco, Y Lee, Gang Liu, D Tran, B Standley, M Aykol, SB Cronin, D Smirnov, et al. Stacking-dependent band gap and quantum transport in trilayer graphene. *Nature Physics*, 7(12):948–952, 2011.

[93] Haoxin Zhou, Tian Xie, Takashi Taniguchi, Kenji Watanabe, and Andrea F Young. Superconductivity in rhombohedral trilayer graphene. *arXiv preprint arXiv:2106.07640*, 2021.

[94] Haoxin Zhou, Tian Xie, Areg Ghazaryan, Tobias Holder, James R Ehrets, Eric M Spanton, Takashi Taniguchi, Kenji Watanabe, Erez Berg, Maksym Serbyn, et al. Half and quarter metals in rhombohedral trilayer graphene. *arXiv preprint arXiv:2104.00653*, 2021.

[95] Fan Zhang, Bhagawan Sahu, Hongki Min, and Allan H MacDonald. Band structure of a b c-stacked graphene trilayers. *Physical Review B*, 82(3):035409, 2010.

[96] Rui Xu, Long-Jing Yin, Jia-Bin Qiao, Ke-Ke Bai, Jia-Cai Nie, and Lin He. Direct probing of the stacking order and electronic spectrum of rhombohedral trilayer graphene with scanning tunneling microscopy. *Physical Review B*, 91(3):035410, 2015.

[97] Debora Pierucci, Thomas Brumme, Jean-Christophe Girard, Matteo Calandra, Mathieu G Silly, Fausto Sirotti, Antoine Barbier, Francesco Mauri, and Abdelkarim Ouerghi. Atomic and electronic structure of trilayer graphene/sic (0001): Evidence of strong dependence on stacking sequence and charge transfer. *Scientific reports*, 6(1):1–9, 2016.

[98] Long-Jing Yin, Li-Juan Shi, Si-Yu Li, Yu Zhang, Zi-Han Guo, and Lin He. High-magnetic-field tunneling spectra of a b c-stacked trilayer graphene on graphite. *Physical review letters*, 122(14):146802, 2019.

[99] Long-Jing Yin, Li-Zhen Yang, Li Zhang, Qilong Wu, Xiaoshuai Fu, Ling-Hui Tong, Guang Yang, Yuan Tian, Lijie Zhang, and Zhihui Qin. Imaging of nearly flat band induced atomic-scale negative differential conductivity in abc-stacked trilayer graphene. *Physical Review B*, 102(24):241403, 2020.

[100] Yanmeng Shi, Shuigang Xu, Yaping Yang, Sergey Slizovskiy, Sergey V Morozov, Seok-Kyun Son, Servet Ozdemir, Ciaran Mullan, Julien Barrier, Jun Yin, et al. Electronic phase separation in multilayer rhombohedral graphite. *Nature*, 584(7820):210–214, 2020.

[101] Alexander Kerelsky, Carmen Rubio-Verdú, Lede Xian, Dante M. Kennes, Dorri Halbertal, Nathan Finney, Larry Song, Simon Turkel, Lei Wang, Kenji Watanabe, Takashi Taniguchi, James Hone, Cory Dean, Dmitri N. Basov, Angel Rubio, and Abhay N. Pasupathy. Moiréless correlations in abca graphene. *Proceedings of the National Academy of Sciences*, 118(4), 2021.

[102] Debora Pierucci, Haikel Sediri, Mahdi Hajlaoui, Jean-Christophe Girard, Thomas Brumme, Matteo Calandra, Emilio Velez-Fort, Gilles Patriarche, Mathieu G Silly, Gabriel Ferro, et al. Evidence for flat bands near the fermi level in epitaxial rhombohedral multilayer graphene. *ACS nano*, 9(5):5432–5439, 2015.

[103] Hugo Henck, Jose Avila, Zeineb Ben Aziza, Debora Pierucci, Jacopo Baima, Betül Pamuk, Julien Chaste, Daniel Utt, Miroslav Bartos, Karol Nogajewski, et al. Flat electronic bands in long sequences of rhombohedral-stacked graphene. *Physical Review B*, 97(24):245421, 2018.

[104] Mikito Koshino. Interlayer screening effect in graphene multilayers with a b a and a b c stacking. *Physical Review B*, 81(12):125304, 2010.

[105] Yaping Yang, Yi-Chao Zou, Colin R Woods, Yanmeng Shi, Jun Yin, Shuigang Xu, Servet Ozdemir, Takashi Taniguchi, Kenji Watanabe, Andre K Geim, et al. Stacking order in graphite films controlled by van der waals technology. *Nano letters*, 19(12):8526–8532, 2019.

[106] Yuanbo Zhang, Victor W Brar, Feng Wang, Caglar Girit, Yossi Yayon, Melissa Panlasigui, Alex Zettl, and Michael F Crommie. Giant phonon-induced conductance in scanning tunnelling spectroscopy of gate-tunable graphene. *Nature Physics*, 4(8):627–630, 2008.

[107] TO Wehling, Ilya Grigorenko, AI Lichtenstein, and AV Balatsky. Phonon-mediated tunneling into graphene. *Physical review letters*, 101(21):216803, 2008.

[108] Christopher Gutiérrez, Lola Brown, Cheol-Joo Kim, Jiwoong Park, and Abhay N Pasupathy. Klein tunnelling and electron trapping in

nanometre-scale graphene quantum dots. *Nature Physics*, 12(11):1069–1075, 2016.

[109] Wonhee Ko, Saban M Hus, Xufan Li, Tom Berlijn, Giang D Nguyen, Kai Xiao, and An-Ping Li. Tip-induced local strain on mo s 2/graphite detected by inelastic electron tunneling spectroscopy. *Physical Review B*, 97(12):125401, 2018.

[110] Ruoting Yin, Yi Zheng, Xiaochuan Ma, Qing Liao, Chuanxu Ma, and Bing Wang. Clarifying the intrinsic nature of the phonon-induced gaps of graphite in the spectra of scanning tunneling microscopy/spectroscopy. *Physical Review B*, 102(11):115410, 2020.

[111] Canxun Zhang, Tiancong Zhu, Salman Kahn, Shaowei Li, Birui Yang, Charlotte Herbig, Xuehao Wu, Hongyuan Li, Kenji Watanabe, Takashi Taniguchi, et al. Visualizing delocalized correlated electronic states in twisted double bilayer graphene. *Nature communications*, 12(1):1–8, 2021.

[112] Edward McCann and Vladimir I Falko. Landau-level degeneracy and quantum hall effect in a graphite bilayer. *Physical review letters*, 96(8):086805, 2006.

[113] SJ Altenburg and R Berndt. Local work function and stm tip-induced distortion of graphene on ir (111). *New Journal of Physics*, 16(5):053036, 2014.

[114] P Xu, Yurong Yang, D Qi, SD Barber, JK Schoelz, ML Ackerman, L Bellaiche, and PM Thibado. Electronic transition from graphite to graphene via controlled movement of the top layer with scanning tunneling microscopy. *Physical Review B*, 86(8):085428, 2012.